NASA CR-134680

(NASA-CR-134680) ON THE INVESTIGATION OF CASCADE AND TURBOMACHINERY ROTOR WAKE CHARACTERISTICS Contractor Report, 1 Jul. 1973 - 30 Jun. 1974 (Pennsylvania State Univ.) 242 p HC $7.50 CSCL 21E G3/07
N75-16555
Unclas
09662

ON THE INVESTIGATION OF CASCADE AND TURBOMACHINERY ROTOR WAKE CHARACTERISTICS

By

R. RAJ AND B. LAKSHMINARAYANA

Prepared for

NATIONAL AERONAUTICS AND SPACE ADMINISTRATION

Contract NAS 3-17855

Department of Aerospace Engineering
The Pennsylvania State University
University Park, Pennsylvania 16802

1. Report No. NASA CR - 134680	2. Government Accession No.	3. Recipient's Catalog No.

4. Title and Subtitle On the Investigation of Cascade and Turbomachinery Rotor Wake Characteristics	5. Report Date February 1975
	6. Performing Organization Code
7. Author(s) R. Raj and B. Lakshminarayana	8. Performing Organization Report No.
	10. Work Unit No. YOF 6402
9. Performing Organization Name and Address The Pennsylvania State University 233 Hammond Building University Park, PA 16802	11. Contract or Grant No. NAS 3-17855
	13. Type of Report and Period Covered Contractor Report; July 1, 1973 to June 30, 1974
12. Sponsoring Agency Name and Address National Aeronautics and Space Administration Washington, D.C. 20546	14. Sponsoring Agency Code

15. Supplementary Notes

16. Abstract

The objective of the investigation reported in this thesis is to study the characteristics of a turbomachinery rotor wake, both analytically and experimentally. The constitutive equations for the rotor wake are developed using generalized tensors and a non-inertial frame of reference. Analytical and experimental investigation is carried out in two phases; the first phase involved the study of a cascade wake in the absence of rotation and three dimensionality. In the second phase the wake of a rotor is studied. Simplified two- and three-dimensional models are developed for the prediction of the mean velocity profile of the cascade and the rotor wake, respectively, using the principle of self-similarity. The effect of various major parameters of the rotor and the flow geometry is studied on the development of a rotor wake. Laws governing the decay of the wake velocity defect in a cascade and rotor wake as a function of downstream distance from the trailing edge, pressure gradient and other parameters are derived. Experimental investigations on the study of cascade and rotor wake were carried out in a cascade tunnel and axial flow fan facilities. Two and three sensor hot wire probes were used to measure the mean velocity and turbulence quantities of a cascade and a rotor wake, respectively. Static pressure measurements were carried out using a three-dimensional spherical probe. All the measurements were carried out in a stationary frame of reference. The experimental data was used to determine the unknown constants in the decay laws for the mean velocity defect and in specifying the decay laws for the maximum value of turbulence intensity and Reynolds stresses. From the overall investigation, it is concluded that wakes of cascade and rotor differ widely from the wakes of simple bodies, such as a cylinder or a flat plate or airfoil. Though the cascade and rotor wake are nearly self-similar in mean velocity profile close to the trailing edge of the blade, they are not self-preserving. The region of self-preservation is observed farther away from the trailing edge. The level of anisotropy and total turbulence level is found to be highest in the case of a rotor wake. The decay rate of mean and turbulence quantities in the rotor wake is much larger compared to a cascade, an isolated airfoil, a flat plate or a cylinder wake. The ratio of total stress to that of turbulence energy is found to vary considerably across the wake.

17. Key Words (Suggested by Author(s)) Three Dimensional Wake Turbomachinery Cascade	18. Distribution Statement Unlimited

19. Security Classif. (of this report) Unclassified	20. Security Classif. (of this page)	21. No. of Pages 188	22. Price*

* For sale by the National Technical Information Service, Springfield, Virginia 22151

NASA CR 134680

FINAL REPORT

ON THE INVESTIGATION OF CASCADE AND TURBOMACHINERY ROTOR WAKE CHARACTERISTICS

By

R. RAJ and B. LAKSHMINARAYANA

Prepared for
NATIONAL AERONAUTICS AND SPACE ADMINISTRATION
Contract NAS 3-17855

Technical Management By
NASA Lewis Research Center
Cleveland, Ohio
M. F. Heidmann

February 1975

Department of Aerospace Engineering
The Pennsylvania State University
University Park, PA 16802

ERRATA SHEET

Page	Line or Equation	Remarks
36	Line 3 from bottom	Read 3×10^2 as 6×10^2 (Sec^{-1})
71	Equation 5.24	Should read as $\frac{\bar{U}_r}{\bar{U}_{so}} = \frac{\bar{U}_d}{\bar{U}_{so}} \cdot \frac{-8(A+\phi')\nu_T^2 + (\bar{U}_{so} B S \cos\lambda)^2}{4B_1 \Omega \sin\lambda (S\cos\lambda)^2 \nu_T} \cdot A_6 \cos\{[\frac{A+\phi'}{B_1}]^{1/2} \eta_3\}$
71	Equation 5.27	Should read as $B_1^2 (\frac{\bar{U}_{so} S'}{4\nu_T})^2 + \phi' = \frac{\pi^2}{4} B_1$
112	Figure 7.5	The decimal points are not correct on the ordinate axis and need to be divided by a factor of 10.
121	Figure 7.9	The scale on the left-hand ordinate axis need to be reduced by a factor of 2.76 except the number 0.23
135	Line 8 from bottom	Read $T_D = \sqrt{\overline{V^2}}/\bar{V}$
138	Equation 8.1	Read $2\Omega\bar{U}_{so}\sin\lambda$ with minus sign
147	Equation 8.3	Read π^2/R_s with minus sign
156	Equation 8.5	The value of constant A is 0.0109, 0.017 and 0.025

ACKNOWLEDGMENTS

The authors wish to express their thanks to Dr. J. L. Lumley for his help on the theoretical developments of the problem; J. Ross, B. Nuss and J. Rishel for experimental set-up, Mark Hurvitz for indispensable help in data processing and computer programming, Mrs. S. Raj for drafting various figures.

The research reported here was supported by National Aeronautics and Space Administration through the contract NAS 3-17855 (with technical management by M. F. Heidmann) and by the Applied Research Laboratory of The Pennsylvania State University.

TABLE OF CONTENTS

TABLE OF CONTENTS (continued)

LIST OF FIGURES

LIST OF FIGURES (continued)

LIST OF FIGURES (continued)

LIST OF FIGURES (continued)

NOMENCLATURE

b	wake width
bo	initial wake width
c	chord length
c_d, c_L	coefficient of drag and lift respectively
D'	turbulence dissipation
E	instantaneous output voltage from hot wire anemometer
E_o	voltage at zero velocity
f	sampling frequency of ADC unit
G	$\lvert\tau_o\rvert/\rho\overline{q^2}$
$g^{\ell j}$	metric tensor
H	shape factor
H_t	value of shape factor at the blade trailing edge
L	mixing length
ℓ	half the wake width
ℓ_{os}, ℓ_{op}	characteristic length scales of the wake on the suction and pressure sides respectively
M	$2\pi f/\Omega n$
N_1	number of wakes processed
n	number of rotor blades
P	$\left[-\overline{U'_z U'_y}\,\frac{\partial \bar{U}_z}{\partial y} / (\overline{U'^2_z} - \overline{U'^2_y})\,\frac{\partial \bar{U}_z}{\partial z}\right]_{y=\ell}$
P_a	ambient static pressure
P_s	static pressure
P_T	total pressure
P^*	reduced pressure $(P_s - \Omega^2 r^2/2)$
$\overline{q^2}$	turbulence energy

NOMENCLATURE (continued)

r	radius of the rotor
r, θ, z	radial, tangential, and axial directions respectively (Figure 5.1)
r_h, r_m, r_t	hub, mean, and tip radius of the rotor
R_L	qL/ν
R_d	$\bar{U}_d \ell/\nu_T$
R_s	$\bar{U}_d S'/\nu_T$
$S'_{ik}, \bar{S}_{ik}$	instantaneous and mean strain rate tensors respectively
S	spacing of the blades
S'	$S \cos \lambda$
s, n, r	s is the streamwise direction along the wake centerline, n is normal to s and r (radial direction). (Figure 3.1)
T	time scale for return to isotropy
T_D	$V^2/\bar{V}$, $\bar{V}$ = circumferential average
T_s, T_n, T_r	normalized components of turbulence intensities in s, n, and r directions respectively $\left(\sqrt{\overline{U'^2_s}}/\bar{U}_{somax}, \sqrt{\overline{U'^2_n}}/\bar{U}_{somax}, \sqrt{\overline{U'^2_r}}/\bar{U}_{somax}\right)$
T_{uz}, T_{uy}, T_{ux}	components of turbulence intensities normalized with respect to local mean velocity in z, y, and x directions respectively $\left(\sqrt{\overline{U'^2_z}}/\bar{U}_z, \sqrt{\overline{U'^2_y}}/\bar{U}_z, \sqrt{\overline{U'^2_x}}/\bar{U}_z\right)$
U'	component of fluctuating velocity
$\bar{U}$	component of mean velocity
$\bar{U}_c$	wake centerline velocity
$\bar{U}_d$	wake velocity defect
$\bar{U}_{so}$	mean velocity component in s direction outside the wake (Figure 3.1)

$\bar{U}_{zo}$	mean velocity component in z direction outside the wake (Figures 4.1 and 5.1)
V	instantaneous absolute velocity
$V_{cm\ell}$	cooling velocity sensed by ℓth wire at the mth data point. (Figure 6.12)
$\underline{V}_{om}$	instantaneous velocity vector at the mth data point (Figure 6.12)
$V_{m\ell}$	component of instantaneous velocity vector along the ℓth sensor (Figure 6.12)
W	instantaneous relative velocity
W'	turbulent fluctuation in relative velocity
x, y, z	direction of x, y, z axes (Figure 4.1)
$\alpha_{m\ell}$	defined in Figure 6.12
β_c	defined in Figure 6.12
Γ_{ij}^{ℓ}	Christoffel symbol
δ_{ij}	Kroneckers delta
ε_{ipq}	alternating tensor
ζ	pressure loss coefficient
η	y/ℓ
η_1	$(r\theta/z^{1/2})(\bar{U}_{zo}/2\nu_T)^{1/2}$
η_2	$2r\theta/S$
η_3	$2n/S' \cos \lambda$
θ^*	momentum thickness
θ_1, θ_2	probe angles (Figure 6.12)
θ_4	turning angle
λ	inviscid outlet air angle
ν	kinematic viscosity
ν_T	turbulent exchange coefficient for momentum
ρ	density

NOMENCLATURE (continued)

τ_o	total Reynolds stress
τ_{sn}, τ_{rn}, τ_{sr}	shear stresses $[\overline{U'_s U'_n}/\bar{U}^2_{somax}, \overline{U'_r U'_n}/\bar{U}^2_{somax}, \overline{U'_s U'_r}/\bar{U}^2_{somax}]$
ϕ_1	$4\Omega K_8 (2\nu_T/\bar{U}_{zo})^{1/2}$
ϕ'	$(\Omega^2 S^2/\bar{U}^2_{so}) \sin^2\lambda \ \cos^2\lambda$
ψ	static pressure coefficient $[(P_s - P_a)/\rho\bar{U}^2_{somax}]$
Ω	angular velocity of the rotor
Ω_d	angular velocity of the rotor at design point.

Subscripts

s, n, r	values in s, n, and r directions respectively
r, θ, z	values in r, θ, and z directions respectively
x, y, z	values in x, y, and z directions respectively
m	values at the mth data point
ℓ	sensor of the probe
1, 2, 3	see Figure 6.12
$1'$, $2'$, $3'$	see Figure 6.12
i, j, k, etc.	tensor indices

Superscript

$\dot{}$	time derivative
$\overline{\quad}$	time averaged values
$\widetilde{\quad}$	ensemble averaged values

CHAPTER I

INTRODUCTION

1.1 General Statement of the Problem

A turbomachinery rotor, henceforth referred to as a rotor, forms an essential and integral part of the turbo-power and propulsion plants for underwater, air, land, and space applications. Rotor performance depends upon the effectiveness of its aerodynamic and mechanical design. There are a large number of problems related to the efficient design of a rotor. A few of these problems have been resolved using theoretical and experimental information on a cascade of airfoils and using empirical data on actual rotors. There are still many problems which remained unresolved until recently. One such problem is the viscous region behind a cascade of airfoils and rotors. The viscous region downstream of cascade of airfoils and the rotor in an otherwise uniform stream of fluid is known as the cascade and rotor wake, respectively. This wake region excludes tip vortices, boundary layers on the annulus and hub walls. Lack of information on the characteristics of cascade and rotor wakes has hindered the development of adequate theories for the prediction of noise, unsteady aerodynamic loading, bending, and torsional vibrations of the blades in a multi-stage turbomachine.

The investigation of the total wake problem is very complex. Due to the complicated nature of the problem, it still continues to be one of the least understood phenomena in turbomachines. The complications involved in the analytical and experimental investigations are many. The flow field behind a rotor is highly three-dimensional. There is periodic variation, as well as random fluctuation in velocity. Moreover, the flow field behind the rotor is a function of a number of parameters such as radial and axial pressure gradients, speed of rotation, incidence, solidity, hub/tip ratio, blade geometry, blade outlet angle, free stream turbulence, and the distance downstream of the trailing edge.

Due to complexity, economics, and time limitations, it is not feasible to study the effect of all parameters on which the rotor wake depends in a rotating facility. However, some of the parameters on which the rotor wake depends can be easily simulated, theoretically and experimentally, in a cascade of airfoils. Unfortunately, the literature survey on two- and three-dimensional wakes (Chapter II) indicates that even a two-dimensional cascade wake model is not yet available and most aerodynamists and acousticians still use the isolated airfoil wake model developed by Silverstein et al. (57). The use of this model for the prediction of mixing losses and noise from rotors is seriously doubted.

Although it is convenient and economical to study the turbomachinery flow field in a cascade setup, the presence of coriolis and centrifugal forces, swirl, and pressure gradients which cannot be simulated in a cascade, would make the rotor wake characteristics different from those of a cascade or isolated airfoil. The variation of the blade element circulation along the blade span gives rise to shed vortices. This effect, in addition to radial variation of blade boundary layer growth and spanwise flow, causes considerable variation in the properties of the wake along the span. Hence, there is a great need for an experimental and analytical study of the rotor wake in an actual environment with a view to obtain more accurate wake models for turbomachinery rotors.

1.2 Objectives of the Present Investigation

The present program on the investigation of turbulent wakes of a rotor and a cascade of airfoils was undertaken with the following objectives:

(a) To understand the rotor wake properties, especially to discern how the centrifugal and the coriolis forces, pressure gradient, and rotor cascade geometry affect the wake development, experimentally, in a cascade of airfoils and a rotor.

(b) To study the cascade wakes and how they differ from an isolated airfoil.

(c) To develop an appropriate model, based on theory and experiment, for the prediction of rotor wake properties. It is intended to include as many variables as possible.

1.3 Method and Means of Investigation

Realizing the difficulties stated in the previous sections, the present investigation is carried out in two phases. Phase one includes extensive theoretical and experimental study of the characteristics of a cascade wake, while phase two covers a detailed study of the rotor wake.

The general problem for the prediction of the mean and turbulence quantities for both the rotor and the cascade wake is first formulated (Chapter III) by considering the equations of continuity, mean motion, Reynolds stress, and turbulence dissipation. These equations are obtained in a generalized tensor form and expressed in a relative rotating coordinate system. The technique used for modeling the various terms in the absence of rotation and curvature is adopted from Lumley

(40) and Lumley and Khajeh-Nouri (41). The complete set of equations governing the wake flow form a closure problem with eleven unknowns and few undetermined constants.

After the formulation of the general problem a simplified cascade wake model is developed (Chapter IV). Boundary layer approximations and an order of magnitude analysis are used to simplify the equations of mean motion. Characteristics of mean velocity at the wake centerline and the wake width are predicted by applying the principle of self-similarity to the simplified equations of mean motion and correlating the Reynolds stress to mean velocity gradient through eddy viscosity. The principle of self-similarity in this analysis on the basis of strong experimental evidence is used even close to the trailing edge of the blade. The cascade wake model so developed is capable of predicting mean flow characteristics of the near and far wake characteristics of turbulent quantities. Some relative estimates of turbulence quantities are made.

The experimental investigations are carried out in a cascade of airfoils (Chapter VI). The measurements of the mean and turbulence quantities are carried out with a five-hole pressure probe and a two sensor hot-wire probe at various axial and transverse locations downstream of the wake. Using the analytical model and the experimental data, the concept of self-preservation, the effect of incidence, solidity, variation of eddy viscosity, and decay rate of mean and turbulence quantities are examined. A thorough investigation of a cascade wake is helpful in the understanding and the development of simplified rotor wake models.

The effect of some of the parameters which cannot be investigated in a cascade (e.g., rotation, pressure gradient in spanwise direction, etc.) are included in the second phase of the investigation. Simplified rotor wake models are developed (Chapter V) for two types of rotors-staggered and unstaggered blades. Equations of mean motion are simplified by an order of magnitude analysis. Solutions for the mean radial and streamwise profiles are predicted by using the principle of self-similarity. Equations of Reynolds shear stress are examined for the near and far wake characteristics of turbulence quantities. Some relative estimates of turbulence quantities and the effect of rotation on them are determined.

The experimental investigation on the rotor wake is carried out using a pre-calibrated static pressure probe, single sensor, and a triple sensor hot-wire probes (Chapter VI). The measurements are taken in a stationary coordinate system at various axial and radial locations downstream of the rotor. The measurement of the overall disturbance level and its decay with distance downstream of the trailing edge of the rotor blade is carried out with a single sensor hot-wire probe. The mean velocity profiles and distribution of turbulence intensities and shear stresses across the rotor wake are obtained from the triple sensor hot-wire probe data. The data from the triple sensor hot-wire probe is memorized in a tape recorder. Details on processing the data from the triple sensor probe are described in Chapter VI.

CHAPTER II

LITERATURE SURVEY ON WAKES AND TURBULENCE MODELING

Interest in the study of flow fields past bodies originated around 1920. The non-zero vorticity region downstream of a body in an otherwise uniform stream of fluid is commonly referred to as "wake". The investigations started with the study of wakes of simple bodies (cylinder, sphere, flat-plate, and airfoil) at low Reynolds numbers. Excellent reviews (3, 21, 27) are available in early work on wakes of simple bodies at low Reynolds numbers. Later on, it was realized that many of the flows in engineering applications are at comparatively high Reynolds numbers and are usually turbulent. Therefore, the study of laminar (low Reynolds number) wakes remained more or less of academic interest.

In the following sections, a comprehensive review of the theoretical and experimental work on the two- and three-dimensional turbulent wakes is presented. Most of the available literature on two- and three-dimensional turbulent wakes is on the prediction of mean properties of the wake. However, for the accurate prediction of the wake properties, turbulence modeling is important. Hence, a qualitative review of turbulence modeling is also presented and the various problems encountered in turbulence modeling of turbomachinery flows are also outlined.

2.1 Turbulent Wakes

2.1.1 Two-Dimensional Wake

2.1.1.1 Bluff Bodies. The turbulent wakes behind two-dimensional bluff bodies were first investigated by Schlichting (56). His theory was based on Prandtl's mixing length theory. According to Prandtl's theory,

$$\tau = \rho L^2 \left|\frac{\partial \bar{U}_z}{\partial y}\right| \frac{\partial \bar{U}_z}{\partial y} \tag{2.1}$$

where

τ = Reynolds stress,
y = transverse coordinate,
L = mixing length, and
$\bar{U}_z$ = mean velocity in the wake.

A similar solution based on Prandtl's new theory was later obtained by Reichardt (51). According to Prandtl's new theory,

$$\tau = \rho\ \nu_T \frac{\partial \bar{U}_z}{\partial y} \text{ and } \nu_T = \chi \ell (\bar{U}_{zo} - \bar{U}_c), \tag{2.2}$$

where

ν_T = eddy viscosity or turbulent exchange coefficient for momentum,
ℓ = half the wake width,
χ = empirical constant,
$\bar{U}_{zo}$ = wake edge velocity, and
$\bar{U}_c$ = wake center line velocity.

The above mentioned solutions are valid only at a distance far downstream of the body (50 diameters in the case of a cylindrical body).

The main reason for this is that in the case of bluff bodies, the analytical description of the flow field close to the body is difficult due to the existence of large scale unsteadiness in this region. Moreover, the above solutions were obtained by applying boundary layer approximations and the precise location beyond which the theory is valid has not been established.

Olsson (44) studied turbulent wakes of equally spaced, identical cylinders. This case was investigated both theoretically and experimentally and the theoretical results were found to be in fairly good agreement with the experimental results. This solution takes into account the effect of spacing and showed that the wake centerline velocity recovers at a slower rate with an increase in spacing. The solution is not valid for near wake prediction. Palmer and Keffer (45) also investigated the similar case but with unequally spaced cylinders of unequal diameters. In this investigation, it was established that the energy reversal region exists in the wake of these cylinders. Cordes (17) studied the near wake characteristics of equally spaced cylinders and estimated the second order effects on the characteristics of the wake as the body is approached.

All of the above cases were investigated for constant pressure along the streamwise direction. Hill et al. (29) studied the wake of a rectangular body with a pressure gradient in the streamwise direction and derived the criteria for the growth and decay of a wake. The criteria were based on the family of wake profiles represented by

$$\frac{\bar{U}_c}{\bar{U}_{zo}} = 1 + a_1 \left(\frac{B^2 z}{\theta_t^*}\right) , \tag{2.3}$$

where

B = fraction of $\bar{U}_c$ at the centerline of the wake,

θ_t^* = momentum thickness at the trailing edge, and

a_1 = parameter representative of pressure gradient.

If $a_1 > 0.10$, the wake would decay an order of magnitude faster than the constant pressure wake. On the other hand, for $a_1 < -0.01$, the wake would tend to grow rather than decay.

2.1.1.2 Streamlined Bodies. The laminar wake solution provided a good starting point for the development of an empirical turbulent wake model. As discussed in Reference (26), the wake centerline velocity in the case of a flat plate laminar wake could be estimated from the following relation:

$$\frac{\bar{U}_c}{\bar{U}_{zo}} = 1 - a_2 \left(\frac{z}{c} + \frac{z_o}{c}\right)^{-1/2} + d_2 \left(\frac{z}{c} + \frac{z_o}{c}\right)^{-1} \qquad (2.4)$$

where c is the length of the plate and a_2, z_o, and d are constants for a particular flow and geometry of the flat plate. Near the trailing edge, i.e., for $z < c$, both of the terms in Equation (2.4) would dominate the solution, while far downstream of the trailing edge, i.e., for $z > c$, the first term in Equation (2.4) would dominate the solution. This explains why the centerline velocity recovery would be faster near the trailing edge. However, due to intense turbulent mixing, the recovery in the centerline velocity of a turbulent wake would be much faster than in the case of a laminar wake. In general, the velocity recovery characteristics of the turbulent wake could be described by the relation

$$\frac{\bar{U}_c}{\bar{U}_{zo}} = 1 - a_3 \left(\frac{z}{c} + \frac{z_o}{c}\right)^{-1/2} , \qquad (2.5)$$

where constants a_3 and z_o would be different from a_2 and z_o, used in relation (2.4) of a laminar wake.

The measurement of mean velocity profile in the wake of a flat plate was carried out by Eagleson et al. (21) in water and by Chevray and Kovasznay (14) in air. In both of these investigations, the measurement of turbulence intensities and Reynolds stresses were also carried out. It could be inferred from both of these investigations that the wake flow near the trailing edge would not be completely self-preserved, however, the mean velocity profiles would be self-similar. It should be stressed that Equation (2.5) would be valid when the turbulence level in the free stream would be low. If the turbulence level in the free stream is high (7 to 8 percent), then the recovery rate would vary, probably as $(z/c + z_o/c)^{-1}$ (Ref. 21). However, detailed experimental data is needed to explicitly express the effect of free stream turbulence on wake centerline velocity recovery rate. No data is available on the study of the near wake of a flat plate under pressure gradient.

Near and far wakes of a symmetrical airfoil were first investigated experimentally by Silverstein et al. (57), who provided empirical relationships for the wake decay. Preston and Sweeting (47) and Preston et al. (48) carried out a systematic investigation of the characteristics of the wake behind an isolated airfoil and observed that a similarity in mean velocity profile exists close behind the airfoil and that the wake centerline velocity recovered to about 80 percent of the free-stream velocity in a quarter chord length from the trailing edge. These observations led Spence (58) to give a general expression of the form

$$1-\frac{\bar{U}_c}{\bar{U}_{zo}} = 0.1265\ \left(\frac{z}{c} + 0.025\right)^{-1/2} . \qquad (2.6)$$

According to Spence, this expression would hold irrespective of the geometry of the airfoil, which is in doubt.

There is at present no general theoretical formulation of wake structure as a function of physical characteristics of an airfoil or its loading. Based on the model equations of Bradshaw et al. (6), Bradshaw (4) suggested a different type of approach to predict the mean velocity characteristics of the near wake of a symmetrical airfoil using a "mixing length" fit to data of Chevray and Kovasznay (14). Bradshaw concluded that the mixing length fit used in the analysis is not valid once the inner wake has spread outside the inner layer of the boundary layer. This type of analysis may not be carried out for the case of an axisymmetric wake since mixing length may be imaginary in part of the flow. In the case of a cascade of cambered airfoils, no analytical treatment is available which predicts the wake centerline velocity, wake width, or the turbulence characteristics. Even experimental data is scarce. The only experimental data on mean velocity profiles in a cascade is due to Lieblein and Roudebush (37) and no conclusion could be drawn from these experiments since the measurements reported by Lieblein and Roudebush are for a very limited range of cascade flow parameters.

Detailed investigations on cascade wakes were reported by Raj and Lakshminarayana (49). Both mean and turbulence characteristics of a cascade wake were considered.

2.1.2 Three-Dimensional Wake

The literature available on three-dimensional wakes has no direct relevance to the rotor wake, but some basic information which can be used in the development of a rotor wake model can be inferred from the following review on three-dimensional wakes.

2.1.2.1 Stationary Bodies.

The study of three-dimensional wakes at low Reynolds number started as early as 1930. A short review of the early experimental and theoretical work was reported by Goldstein (27). It could be shown by using Oseen's approximation that even at low Reynolds number and at a large distance away from the body, the wake centerline velocity, in the case of a three-dimensional symmetrical body, would decay faster than in the case of a two-dimensional symmetrical body. However, at large Reynolds number, the wake would be turbulent and the situation would be different than the laminar wake. Swan, (60), using the mixing length hypothesis, showed that the wake centerline velocity at far downstream of the body of revolution varies as $\sim (1 - z^{-2/3})$. Detailed experimental and theoretical investigations on the turbulent wake of a body of revolution were carried out by Chevray (13). Analytical expressions were derived to express the manner in which the mean characteristics of the wake develop in the established flow region. The measurement of turbulent quantities was also carried out. The results were claimed to be in good agreement with the theory.

Explanatory investigations of the turbulent wakes behind bluff bodies (flat plate, a circular disc) were carried out by Cooper and Lutzky (16). The theoretical analysis of Cooper and Lutzky was no different from those of Goldstein (27) or Swan (60). However, plenty of experimental data was given on turbulence measurements. The work of Cooper and Lutzky appears to have been repeated by Hwang and Baldwin (31) and Carmody (8) after a lapse of about nine years. Hwang and Baldwin distinguished three regions:

(a) Region of high anisotropy extending from the body to about fifty diameters away from it.

(b) Region of near isotropy extending from about one hundred diameters to about four hundred diameters. This is the region of approximate similarity and isotropic relations are adequate for estimating the decay.

(c) Region of high intermittancy extending beyond four hundred diameters and decay rate slows down in the final period.

Stieger and Bloom (59) examined the three-dimensional wakes with initial eccentricity. They reported the following theoretical conclusions:

(a) The wake with any degree of initial eccentricity degenerates to an axisymmetric configuration and the mode of decay.

(b) If two wakes have identical flight conditions, identical initial velocity at the axis and identical drag, the wake with the largest initial eccentricity will decay most rapidly.

An interesting approach to the solution of the problem of swirling wakes and jets was given by Reynolds (52) by considering the conservation of both the angular and the axial momentum. Two different cases were considered: (a) flows dominated by axial momentum and (b) flows dominated by angular momentum. Case (a) corresponds to the well known axisymmetric turbulent wake and the Case (b) to the wake of a selfpropelled body. However, no specific conclusions were drawn when both the axial momentum and the angular momentum were of the same order of magnitude.

A recent study on the typical features of turbulent plane and axisymmetric wake flows was carried out by Ermshaus (22). The results showed that each kind of wake has its own distinct characteristics.

2.1.2.2 Rotating Bodies. Chervinsky and Lorenz (12) discussed the case of a free wake behind a rotating body. They showed, analytically, that the maximum swirl component of velocity decays faster in a free jet than in a wake. However, no experimental data is available on the wake of a rotating body. The measurement of mean velocity profile beyond a rotating disc was carried out by Chanaud (10). The momentum integral analysis reported by him did not lead to accurate predictions of the mean flow close to the disc.

The qualitative correlation between the wakes in axial flow compressors and the blade vibrations was first given by Pearson and McKenzie (46). However, no experimental data or theoretical formulation of the compressor wake problem was provided or proposed. An analytical method for predicting the distorted wake geometry behind a helicopter rotor was described by Landgrebe (35). His analysis was developed by the use of Biot-Savart law and numerical integration. However, it was assumed that the wake of a rotor is in the form of a thin vortex sheet. This assumption is of doubtful validity since, due to turbulence and mixing with free stream, the sheet of vortices would develop into a crude wedge. The initial application of Landgrebe's work indicated that significant distortions of the wake geometry occur.

An experimental technique for surveying wake characteristics (mean velocity) of a rotor wake using a single hot-wire was given by Whitfield et al. (63). The hot-wire was used in a stationary system. Lakshminarayana and Poncet (33) developed a method of measuring the mean as well as turbulence properties of the wake using three sensors located in the three coordinate directions at the exit of a rotor blade. They measured the wakes of a three-bladed Rocket Pump Inducer. Kiock (32) and Evans (23) also carried out measurements of rotor wakes with single and cross-wires, respectively. Kiock (32) investigated, experimentally, the overall disturbance and turbulence level in cascade, fan, and compressor rotor wake. The effect of Reynolds number on the turbulence level was also investigated. However, the theoretical representation of the decay of turbulence level is not appropriate since the decay law is derived from the principle of self-preservation, and the principle of self-preservation is not applicable close to the trailing edge of the blade. The hot-wire analysis and measurement carried out by Evans (23) were based on the assumption that radial velocity was zero. Even though this might be true outside the wake, the imbalance between centrifugal and pressure forces inside the wake would give rise to radial velocity. This radial velocity is proportional to wake defect.

2.2 Turbulence Modeling

Most of the models developed for the prediction of mean velocity profile in two-dimensional wakes, jets, and turbulent boundary layers employ the concept of eddy viscosity or mixing length. Such models are quite successful from the point of view of predicting the gross behavior.

There are some major drawbacks of these models. First, these models are based on gross physical reasoning and hence, are unlikely to provide the prediction of local properties accurately. Second, the models fail in several situations (e.g. recirculating flows, energy reversal regions in wakes, etc.). In the region of energy reversal, the mean velocity gradient vanishes and the shear stress is not zero. The existence of such regions in wakes of a cascade of cylinders of unequal diameters and a cascade of cambered airfoils has been established (45, 49). Moreover, the mixing length hypothesis does not take into account the past history of the flow field.

Few of the shortcomings of the mixing length hypothesis can be overcome by representation of eddy viscosity (ν_T) in a modified form (due to Prandtl and Kolmogorov)

$$\nu_T = \overline{U_y'^2} \quad T$$

and

$$\nu_T = \sqrt{\overline{q^2}}\, L \quad , \tag{2.7}$$

where

$\overline{U_y'^2}$ = turbulence intensity in the transverse direction,

T = time scale for return to isotropy,

$\overline{q^2}$ = turbulence energy, and

L = mixing length.

Knowing the eddy viscosity and the mean velocity profiles, it is possible to estimate the shear stress but not the turbulence intensities. In some flow fields, shear stresses may be of the same order as that of turbulence intensity. Excellent critical reviews of the eddy viscosity and mixing length models are provided by Batchelor (1) and Launder and Spalding (36).

Although it is possible to predict approximately the mean velocity profile by the use of eddy viscosity or mixing length models, it is impossible to obtain a description of the turbulent motion. With regard to the prediction of turbulence quantities, Hu (30) and Chou (15) proposed some theoretical models. Due to the lack of advanced calculating machines, no numerical calculations were performed. Batchelor and Townsend (2) obtained quantitative estimates of turbulence quantities using a principle of self-preservation. The principle of self-preservation in wakes is applicable only far downstream of the body where the turbulence reaches an equilibrium structure. However, in the wakes of streamlined bodies, the equilibrium structure of turbulence is reached much earlier compared to bluff bodies. In any case, even closer to a body, there is always a small region at each cross-section in boundary layers and wakes where the turbulence structure is in equilibrium, i.e., production of turbulence equals dissipation of turbulence. These regions are usually away from the region of maximum shear and occur closer to the outer edge, i.e., about 0.5 to 0.30 times the thickness of the viscous region. The axisymmetric flows are also self-similar and can be handled by similar techniques. The turbulence quantities in plane two-dimensional flows obtained by the use of the principle of self-preservation obey the following relationship (Ref. 2, 62):

$$\overline{U_z'^2} \propto (z - z_o)^{-n_1} \tag{2.8}$$

where n_1 is a function of anisotropy and the type of flow field. z_o is the virtual origin. For isotropic turbulence and two-dimensional plane wakes, $n_1 = 1$. In the case of a plane jet, $n_1 = 2$. In the case of a wake of an axisymmetric body, $n_1 = 4/3$.

The experimental data on turbulence properties of flat plate (14) and cascade (49) wakes is inconsistent with the values of the power mentioned earlier. This indicates that the predictions based on the principle of self-preservation are no longer correct very close to a body. There are many other factors which affect the self-preservation principle in actual flow fields (e.g. streamline curvature, rotation, etc.). The detailed effect of streamline curvature on turbulent flow was described in detail by Bradshaw (5) and that of rotation by Raj and Lumley (50).

Higher order closure schemes, which were proposed as early as 1944 (Ref. 15, 30), could provide detailed structure of turbulence in the wake and other types of turbulent flows. Subsequently, several simplified closure techniques were developed. Details on some of the closure techniques were described by Launder and Spalding (36). A detailed quantitative discussion of merits and shortcomings of multi-equation models of turbulence is considered in Chapter III of the thesis. At this point, however, a passing reference is needed to introduce one equation model of Bradshaw et al. (6) which is characteristic of its class. Bradshaw et al.'s closure technique can predict five quantities, three mean components of velocity, and two components of shear stress. One of the major drawbacks of the model is the assumption that shear stress is proportional to turbulent energy and the ratio of two quantities is constant throughout the flow field.

This assumption cannot be justified on the basis of the available information except in some simple flows. Moreover, the model does not account for transport of length scale. Most of the literature on closure problems is referred to in References (5) and (36). More recent closure techniques are due to Lumley and Khajeh-Nouri (41, 42).

Most of the models referred to above have been developed for a stationary, rectangular coordinate system while, at present, most of the boundary layer and wake problems in turbomachinery rotors employ a relative rotating frame of reference which includes both the curvature and rotation terms. Resolving the problems in a rotating frame of reference eliminates the effect of periodic unsteadiness. The transformation of the whole set of turbulence model equations from a stationary coordinate system to a rotating coordinate system appears simple at first glance, but the actual procedure is complicated. Lumley (38) has indicated a method of carrying out such a transformation. The modeling procedure should properly account for the effect of curvature and rotation on the turbulence structure. This is a difficult task and has not yet been accomplished.

The effect of rotation can be large, moderate, or small depending upon the speed of rotation of the machine and blade geometry. If the strain rate (S_{ij}) and the speed of rotation ($\varepsilon_{ijk}\Omega_k$) of the machine are of the same order of magnitude, it is not difficult to implement the necessary changes in the modeling. However, if $\varepsilon_{ijk}\Omega_k > S_{ij}$, there is no available technique by which the effect of rotation can be taken into account in the modeling. In such a situation, it appears that the dominant length and time scale of the turbulence motion are controlled by rotation only, and strain rates have a secondary effect on these scales.

CHAPTER III

THEORETICAL FORMULATION OF THE TURBOMACHINERY WAKE PROBLEM

A critical review of turbulent boundary layers and wakes presented in the second chapter indicates that most of the existing closure techniques on turbulence modeling are not applicable to turbomachine rotors. There is also no technique which can accommodate a situation when angular speed of rotation (Ω) is higher than the mean strain rate of the flow.

The main objective of this chapter is to describe the formulation of a rotor wake closure problem in a generalized coordinate system. The generalized coordinate system will include all curvature and rotation terms. This problem will then be simplified by retaining only the highest order terms as applicable to turbomachinery rotor wakes. The problem formulated in a generalized coordinate system could easily be reduced to a non-inertial frame of reference for stators and cascade wakes. A description of the rotor wake problem, the physical nature and classification of the cascade and rotor wake will be discussed.

3.1 Physical Nature of Cascade and Rotor Wakes

3.1.1 Cascade Wake

The mean velocity in a cascade wake is two-dimensional and is asymmetric. The asymmetry in the wake is due to the past history of the flow. Far downstream, the wake of adjacent airfoils in a cascade interact and the resultant mean velocity profile becomes a periodic function with a period equal to spacing of the blades. The cascade wake, unlike the wake of an isolated airfoil, encounters an adverse pressure gradient because the edge velocity in a cascade wake decreases continuously downstream. A cascade wake differs from the wake of a cylinder, flat plate, and an isolated airfoil (symmetrical and cambered) not only in its mean properties but also in turbulence properties.

3.1.2 Rotor Wake

Wakes of rotor blades, unlike a cascade or an isolated airfoil wake, is three-dimensional in nature (see Figure 3.1). The three-dimensionality of the rotor wake is due to the imbalance in the pressure gradient and the centrifugal forces inside the wake. While the pressure gradient is nearly the same across the wake, there is a variation in the centrifugal forces inside the wake due to velocity defect and this results in radial flows. Depending upon the distribution of absolute tangential velocity, the radial flows can be large or small inward or outward. It should be noted that distribution of absolute tangential velocity acorss the wake can be of wake-type or jet-type, when viewed from a stationary system. This trend is reversed when viewed from a relative system. However, the distribution of axial and radial components of velocity remain the same in the absolute and the relative frame of reference.

Referred to a stationary coordinate system, a cascade or an isolated airfoil wake is continuously moving away from the airfoils. Whereas, a rotor wake remains in close proximity to the rotor blade for a longer period of time due to the rotation of the blade and the resulting swirl. Hence, it might be expected that the wake distortions which are neglected for a cascade or an isolated airfoil assume greater importance for a rotor. Unlike a cascade or an isolated airfoil wake,

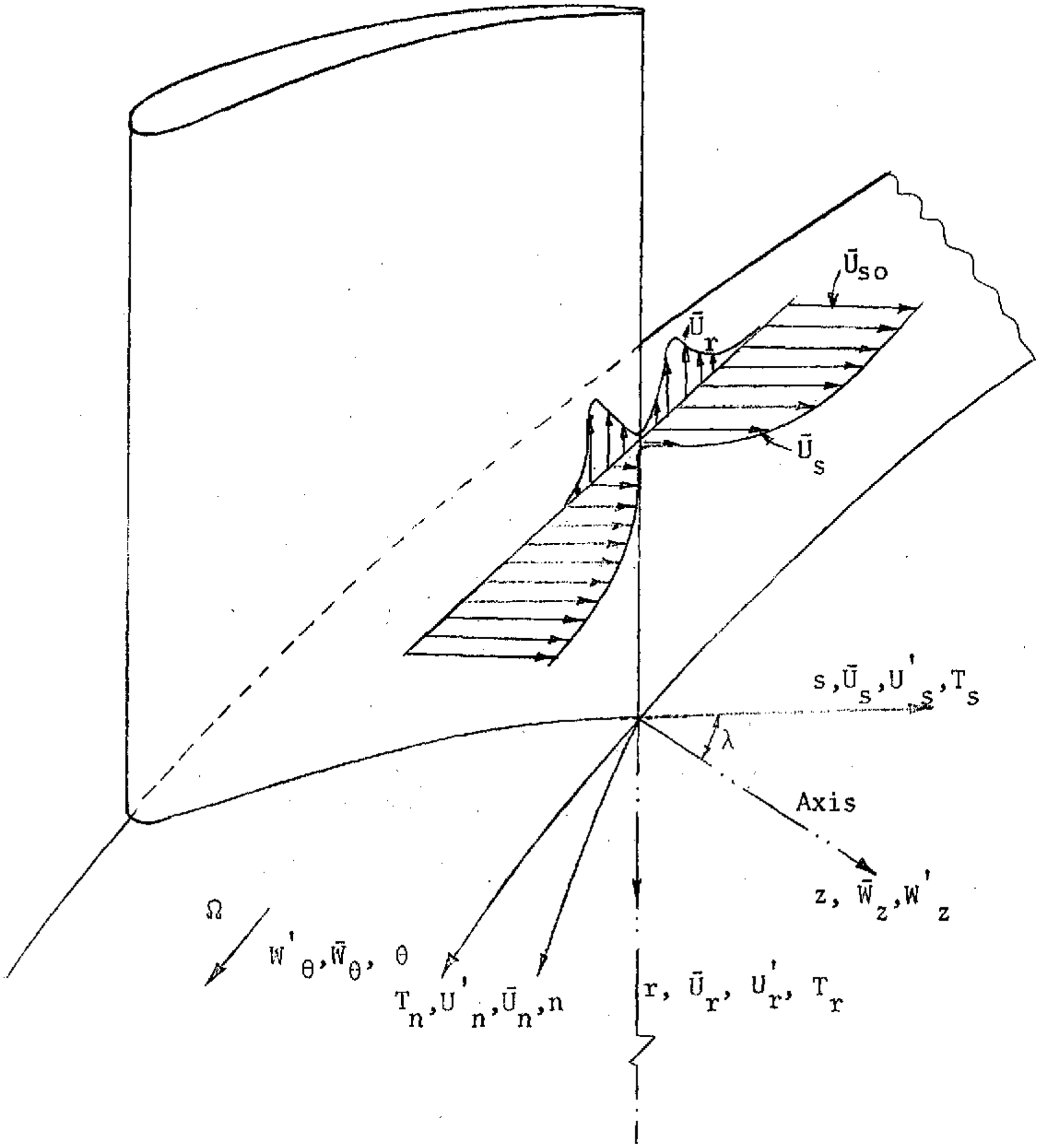

Figure 3.1 Nature of Turbomachinery Rotor Wake and Notations Used.

a rotor wake is periodically unsteady viewed from a stationary frame of reference. However, if referred to a rotating coordinate system, the rotor wake is steady. Furthermore, there is interference in the development of rotor wake from the downstream blade row. Wakes of rotors in the last stages of a turbomachine develop under the influence of pressure gradients and high free stream turbulence. All these effects make the rotor wake extremely complicated in nature.

A rotor wake, like cascade and isolated airfoil wake, is also asymmetric. The asymmetry is due to the loading on the blades. Far downstream, the wake of one rotating blade may interact with the wake of an adjacent blade in high solidity rotors. In addition to this, the flow separation at the trailing edge can also cause changes in the decay rate.

The variation of blade element circulation along the blade span causes the generation of shed vortices which can cause intense mixing of the wake region with the free stream. This may accelerate the decay of wake defect and is also a source of generation of additional turbulence in the flow. The presence of hub and tip boundary layers, secondary flows, etc., are additional sources affecting the decay rate.

3.2 Generalized Form of Governing Equations

In the formulation of the generalized rotor wake problem, the continuity, Navier-Stokes (mean momentum), Reynolds stress and turbulence dissipation equations are used. All the abovementioned equations are presented below in a generalized tensor form for an incompressible fluid. The equations include the curvature terms implicitly and the rotation term explicitly.

Continuity

$$\bar{U}_i{}^{,i} = 0, \; U_i'{}^{,i} = 0, \tag{3.1}$$

where

$\bar{U}_i$ = time averaged component of velocity, and

U_i' = fluctuating component of velocity.

Navier-Stokes (mean momentum)

$$\dot{\bar{U}}_i + \bar{U}_{i,j}\,\bar{U}^j + \left(\overline{U_i'\,U'^j}\right)_{,j} + 2\,\varepsilon_{ipq}\Omega^p\,\bar{U}^q$$

$$= -\bar{P}_{,i}/\rho + \nu\, g^{\ell j}\,\bar{U}_{i,\,\ell j}, \tag{3.2}$$

where

$\varepsilon_{i\rho q}$ = an alternating tensor,

$g^{\ell j}$ = a metric tensor,

$\bar{P}_{,i}$ = time averaged pressure gradient, and

Ω^p = angular velocity.

Reynolds Stress

The equation for Reynolds stress is obtained from the momentum equation for U_i' as follows: the momentum equation for U_i' is multiplied with U_k' and that of U_k' with U_i'. The resulting two equations are added and time averaged to obtain the equation for $\overline{U_i'U_k'}$:

$$\overline{U_i'U_K'} + (\overline{U_i'U_k'})_{,j}\ \bar{U}^j + (\overline{U_k'U'^j}\ \bar{U}_{i,j} + \overline{U_i'U'^j}\ \bar{U}_{k,j})$$

$$+ (\overline{U_i'U_k'\ U'^j})_{,j} + 2\ \Omega^p\ (\overline{U_k'\ U'^q}\ \varepsilon_{ipq} + \overline{U_i'U'^q}\ \varepsilon_{kpq})$$

$$= - (\overline{U_k'\ \ P'}_{,i} + \overline{U_i'\ P'}_{,k})/\rho + \nu g^{\ell j}(\overline{U_k'U'_{i,\ell j}} + \overline{U_i'U'_{k,\ell j}}) \tag{3.3}$$

where $P'_{,i}$ is the gradient of fluctuating pressure.

The significance of various terms in the equation may be summarized as follows: the first term represents a local variation of stress with time; the second term represents transport or convection of stress by the mean flow; the third and fourth terms represent generation or suppression of turbulence; the fifth and sixth terms represent redistribution due to rotation and pressure fluctuations; and the seventh term represents dissipation due to viscosity.

The differential form of Equation (3.3) for a generalized curvilinear coordinate system with $\Omega^P = 0$ is given in Nash and Patel (43).

Turbulence Energy

The equation of turbulence energy is obtained from the equation of Reynolds-stress (3.3) by contraction of indices, i.e.,

$$\overline{q^2} = g^{ik}\ \overline{U_i'U_k'}.$$

It is interesting to note that the rotation term vanishes identically in this equation because it does no work on the material element. The equation can be written as follows:

$$\overline{\dot{q}^2} + \overline{q^2}_{,j}\, \bar{U}^j + (\overline{U'^i U'^j}\; \bar{U}_{i,j} + \overline{U'^k U'^j}\; \bar{U}_{k,j}) +$$

$$(\overline{q^2 U'^j})_{,j} = -2\, (\overline{U'^i P'}_{,i})/\, \rho +$$

$$\nu\, g^{\ell j}\, g^{ik}\, (\overline{U'_k U'_{i,\ell j}} + \overline{U'_i U'_{k,\ell j}}) \; . \tag{3.4}$$

The significance of various terms in this equation are similar to the one as explained for Equation (3.3).

Turbulence Dissipation

The expression for the turbulence dissipation is written as follows:

$$D = 2\,\nu\, S'_{ik}\, S'^{ik} = 2\,\nu\, g^{i\ell} g^{km}\, S'_{ik}\, S'_{\ell m},$$

where $$S'_{ik} = \frac{1}{2}\, (U'_{i,k} + U'_{k,i}).$$

The time averaged value of D is written as $\bar{D}$. The equation for $\bar{D}$ is obtained from the momentum equation for U'_i as follows: from the momentum equation for U'_i and equation for $U'_{i,k}$ is obtained by differentiating the equation for U'_i with respect to subscript k. Interchanging the indices, an equation for $U'_{k,i}$ is obtained. The equation for $U'_{i,k}$ and $U'_{k,i}$ are added and divided by 2. The resulting equation is the equation for S'_{ik}. Similarly, an equation for $S'_{\ell m}$ is obtained. Now, the equation for S'_{ik} is multiplied with $S'_{\ell m}$ and the equation for $S'_{\ell m}$ is multiplied with S'_{ik}. The resulting equations are added which results in an equation for $S'_{ik}S'_{\ell m}$. The equation for $S'_{ik}S'_{\ell m}$ is multiplied by a factor 2 $g^{i\ell}g^{km}$ and time averaged to obtain the equation for $\bar{D}/\nu$. The equation for $\bar{D}/\nu$ is written as follows:

$$\frac{\dot{\bar{D}}}{\nu} + \frac{\bar{D}_{,j}}{\nu}\,\bar{U}^{j} + g^{\ell i}g^{mk}\,[\bar{U}^{j}_{,k}\overline{(S'_{\ell m}U'_{i,j})} + \bar{U}^{j}_{,i}\overline{(S'_{\ell m}U'_{k,j})}]$$

$$+ g^{\ell i}g^{mk}\,[\bar{U}^{j}_{,m}\overline{(S'_{ik}U'_{\ell,j})} + \bar{U}^{j}_{,\ell}\overline{(S'_{ik}U'_{m,j})}] +$$

$$+ [2\,\overline{S'^{ik}U'^{j}}\,(\bar{S}_{ik})_{,j} + 2\,\overline{S'_{ik}U'^{j}}\,(\bar{S}^{ik})_{,j}] +$$

$$+ [\overline{(S'^{ik}U'^{j}_{,k})}\,\bar{U}_{i,j} + \overline{(S'^{ik}U'^{j}_{,i})}\,\bar{U}_{k,j}] +$$

$$+ [\overline{(S'_{ik}U'^{j,k})}\,\bar{U}^{i}_{,j} + \overline{(S'_{ik}U'^{j,i})}\,\bar{U}^{k}_{,j}]$$

$$+ \left(\frac{\overline{DU'^{j}}}{\nu}\right)_{,j} + [\overline{S'^{ik}U'^{j}_{,k}U'_{i,j}} + \overline{S'^{ik}U'^{j}_{,i}U'_{k,j}} +$$

$$+ \overline{S'_{ik}U'^{j,k}U'^{i}_{,j}} + \overline{S'_{ik}U'^{j,i}U'^{k}_{,j}}] +$$

$$+ 2\,\Omega^{P}\,[\varepsilon_{\ell pq}\,\overline{(S'^{ik}U'^{q}_{,k})} + \varepsilon_{kpq}\,\overline{(S'^{ik}U'^{q}_{,i})}]$$

$$+ 2\,\Omega^{P}\,[\varepsilon_{\ell pq}\,\overline{(S'^{\ell m}U'^{q}_{,m})} + \varepsilon_{mpq}\,\overline{(S'^{\ell m}U'^{q}_{,\ell})}]$$

$$= -\frac{2}{\rho}\,g^{\ell i}g^{mk}\,[\overline{S'_{\ell m}P'_{,ik}} + \overline{S'_{ik}P'_{,\ell m}}]$$

$$+ \frac{1}{2}\,g^{nj}\,(\bar{D}_{,nj}) -$$

$$- 2\,\nu\,g^{nj}g^{\ell i}g^{mk}\,[\overline{(S'_{ik})_{,n}\,(S'_{\ell m})_{,j}} +$$

$$+ \overline{(S'_{\ell m})_{,n}\,(S'_{ik})_{,j}}]\,. \tag{3.5}$$

In the above equations, $\bar{S}_{ik} = \frac{1}{2}\,(\bar{U}_{i,k} + \bar{U}_{k,i})$.

The significance of various terms in this equation may be summarized as follows.

The first term represents the local variation of dissipation; the second and eighth terms represent the flux of dissipation due to mean and fluctuating velocity components, respectively, and are large. The third, fourth, sixth and seventh terms may be called the generation terms and are small. The fifth and twelvth terms are contributions to dissipation due to inhomogeneity in the flow and are small. The ninth term represents the production of velocity gradients which is due to the stretching of the fluctuating strain rates and is large. The tenth term represents the redistribution due to rotation and is not identically zero. The eleventh term represents a diffusion transport of dissipation by pressure fluctuation and is small. The thirteenth term represents destruction of gradients by viscosity and is large.

Equations (3.1) to (3.5) are presented in generalized tensors and do not explicitly show the curvature terms. It is necessary to point out that there are nine curvatures in a three-dimensional space. The curvature terms in these equations are associated with the Christoffel symbol ($\Gamma^{\ell}_{i\ell}$). Not all the curvatures are important for investigating the mean properties of the flow in the field of turbomachinery. However, for higher order approximations, all the curvature terms are equally important.

3.3 Turbulence Modeling

A set of equations can be chosen from Section (3.2), depending upon the information and accuracy desired for formulating the closure problem. Any set of equations chosen do not form a closure problem for the complete description of the rotor wake, since the number of unknowns is more than the number of chosen equations. Moreover, not all the equations given in Section (3.2) are needed for the formulation of the closure problem for a turbulent flow: For example, if the Reynolds stress equation is used as a first transport equation then the use of the turbulence energy equation as a second transport, equation does not reveal any additional information because the latter equation is obtained from the Reynolds stress equation by contraction of indices. However, one equation can be used to provide information for the second equation as was done by Bradshaw et al. (6), and Hanjalic and Launder (28).

3.3.1 Turbulence Modeling in Reynolds Stress Equation

Three terms need to be considered for modeling the Reynolds stress equation. They are (a) the pressure gradient velocity correlation, (b) triple velocity correlation, and (c) the viscous term.

(a) Pressure Gradient Velocity Correlation. Chou (15) was the first to propose that the pressure gradient velocity correlation consists of two parts; that is,

$$(\overline{P'_{,i}U'_{k}} + \overline{U'_{i}P'_{,k}}) \,/\, \rho = F^{s}_{rik}\,\bar{U}^{r}_{,s} + b_{ik}, \qquad (3.6)$$

where functions F^{s}_{rik} and b_{ik} can be uniquely determined from double and triple velocity correlation. The form of functions F^{s}_{rik} and b_{ik} given by Chou indicates that part one of the pressure gradient velocity correlation originates from the interaction of the mean strain rate with the turbulence, and the second part is due to the mutual interaction between the fluctuating components. The form of pressure gradient velocity correlation given above limits its use to regions away from the immediate vicinity of the solid boundary. Recently, Hanjalic and Launder (28) and Lumley and Khajeh-Nouri (42) have proposed different forms of the fourth order tensor. Lumley and Khajeh-Nouri gave a more general expression valid for higher order approximation while that of Hanjalic and Launder is only a first order approximation. Lumley and Khajeh-Nouri point out that the first part corresponds to rapid distortion theory, while the second corresponds to non-linear return to isotropy in the absence of shear.

Raj and Lumley (50) have added correction for the effect of rotation on the tendency to equipartition in the modeling of Lumley and Khajeh-Nouri (42). With this correction, the first part of pressure gradient velocity correlation was written as follows:

$$2\ (0.2\ \overline{q^2})\ F_{srik}(\bar{U}_{r,s} - \varepsilon_{rst}\Omega_t)\ , \qquad (3.7)$$

where $F_{srik} = (\delta_{ri}\delta_{sk} + \delta_{rk}\delta_{si})\ /\ 2 + \ldots\ldots$.

This modeling is valid for turbomachinery flow fields when the flow is analyzed in the relative rotating coordinate system.

The second part of the pressure gradient velocity correlation in Equation (3.6) for a nonisotropic homogeneous flow was first modeled by Rotta (54),

$$(\overline{P'_{,i}U'_k} + \overline{P'_{,k}U'_i})\ /\ \rho = A\,\frac{\sqrt{\overline{q^2}}}{L}\,(\overline{U'_iU'_k} - \delta_{ik}\ \overline{q^2}/3)\ , \qquad (3.8)$$

where A is a numerical constant of order unity and L is an integral scale of the turbulence. The effect of pressure gradient velocity correlation is to decrease the anisotropy and the Reynolds stress. Hanjalic and Launder (28), and Lumley (38) replaced the term A $\sqrt{\overline{q^2}}/L$

in Equation (3.8) with 1/T, where $T = k\,\overline{q^2}/\bar{D}$, k is a constant and T is known as relaxation time or time scale for return to isotropy. Daly and Harlow (19) recognized that any modeling technique should satisfy Galilean and tensor invariance. Lumley (38) applied the tensor invariance concept to simple turbulent flows. Donaldson (20) formulated a turbulence closure problem based on tensor invariance. His modeling technique included the dependency on rotation of the mean velocity field (vorticity vector) suggested by Lumley (38) earlier. In a recent work, Lumley and Khajeh-Nouri (42) noted that it is not the vorticity vector but the anti-symmetric rotation tensor (R_{pq}) which is to be included in the expansion scheme of a functional given below. According to the authors a second rank tensor could be written as follows:

$$A_{ij} = -\overline{q^2}/T \; . \quad f_{ij}\,(b_{pq},\, R_{pq}) \qquad (3.9)$$

where f_{ij} is a functional of b_{pq} and R_{pq} and

$$b_{ij} = (\overline{U'_i U'_j}/q^2 - \delta_{ij}/3)$$

The expansion of f_{ij} is given in Reference (42).

(b) <u>Triple Velocity Correlation</u>. Lumley (40) proposed that the trace of $(\overline{U'_k P'}_{,i} + \overline{U'_i P'}_{,k})/\rho$; i.e., $2\;\;\delta_{ik}(\overline{U'_j P'})_{,j}/3\rho$ due to inhomogeneity in the flow can be included with the triple velocity correlation.

In Chou's (15) closure technique, it was not necessary to model the triple velocity correlation because the second transport equation he employed is an equation for the triple velocity correlation. In other closure techniques (Ref. 19, 20, 28, 41), it was not considered appropriate to use the triple velocity correlation equation as a reasonable level of closure. Hanjalic and Launder (28) did not use the triple velocity correlation as a second transport equation but used it to simulate the triple velocity correlation by terms of lower order.

Using a tensor invariance technique, Lumley (40) modeled triple velocity correlation along with a trace of pressure gradient velocity correlation. In a generalized tensor system, this can be written as follows:

$$\overline{(U'_i U'_k + 2\,\delta_{ik}\,P'/3\rho)U'^j} = -A_{11}\,T(\overline{q^2}/3)\,[\delta_{ik}\delta^{j\ell} + a\,(\delta^j_i\,\delta^\ell_k + \delta^\ell_i\,\delta^j_k)\,]\,\overline{q^2}_{,\ell} - A_{12}\,T^2\,(\overline{q^2}/3)\,[\delta_{ik}\delta^{j\ell} + b\,(\delta^j_i\,\delta^\ell_k + \delta^\ell_i\,\delta^j_k)\,]\,\bar{D}_{,\ell} \tag{3.10}$$

where a, b, A_{11}, and A_{12} are undetermined coefficients. The above modeling can be easily reduced to the case of homogeneous flow for $i \neq k$.

There are many other forms of modeling techniques such as by Daly and Harlow (19) for triple velocity correlation, and by Donaldson (20) for trace of pressure gradient velocity correlation. The proposed models are a simple diffusion representation.

(c) Viscous Term. The viscous term in the Reynolds stress equation is $\nu\,g^{\ell j}\,(\overline{U'_k U'_{i,\ell j}} + \overline{U'_i U'_{k,\ell j}})$ and can be decomposed as follows:

$$\nu\,g^{\ell j}[(\overline{U'_i U'_k})_{,\ell j} - 2\,\overline{U'_{i,\ell} U'_{k,j}}]\ . \tag{3.11}$$

The first term is the viscous transport term while the second term is a viscous dissipation. Donaldson (20) modeled the second term assuming that it was proportional to the shear stress. He provided no supporting arguments for this assumption. In most cases (e.g. high Reynolds number approximation) the first term in Equation (3.11) is neglected.

3.3.2 Turbulence Modeling in Turbulence Energy Equation

The turbulence energy equation is independent of the coordinate transformation. The modeling techniques presented for the various terms in the Reynolds stress equation can also be used for modeling terms in the turbulence energy equation.

3.3.3 Simplification of the Turbulence Dissipation Equation and its Modeling

The turbulence dissipation equation presented in an exact form for a generalized coordinate system (Section (3.2)) is very difficult to solve. One of the most suitable methods of simplifying this equation is to use a high Reynolds number approximation. With such an assumption, many terms which are dominant at low Reynolds number (e.g. in the Viscous sublayer very close to the solid boundary) are eliminated. However, in the present investigation of the rotor wake characteristics, flows away from the boundary are of interest and the high Reynolds number approximation is valid. In this case, the expression for turbulence dissipation can be simplified as follows:

$$\bar{D} = 2\,\nu\,\overline{S'_{ik}S'^{ik}}$$

$$= \nu\, g^{i\ell} g^{km}\,[\overline{U'_{i,k}U'_{\ell,m}} + (\overline{U'_{i}U'_{k}})_{,m\ell}] \quad .$$

Now $[\overline{U'_{i,k}U'_{\ell,m}} \,/\, (\overline{U'_{i}U'_{k}})_{,m\ell}] \sim 0\,(R_L)$,

where $R_L = qL/\nu$.

If we ignore terms of order $1/R_L$, then:

$$\bar{D} = \nu\, g^{i\ell} g^{km} (\overline{U'_{i,k} U'_{\ell,m}})$$

$$= \nu\, \overline{U_{i,k} U^{i,k}} \quad . \tag{3.12}$$

Several authors [e.g., Daly and Harlow (19), Hanjalic and Launder (28), Lumley and Khajeh-Nouri (41), etc.] have contributed towards the development of suitable models for the turbulence dissipation equation in the cartesian tensor form. With the exception of Lumley and Khajeh-Nouri (41), most of the authors have retained terms not consistent with the order of other terms retained in the equation. Therefore, it appears appropriate at this time to extend Lumley and Khajeh-Nouri's technique to the generalized turbulence dissipation Equation (3.5). Following the arguments developed by Lumley and Khajeh-Nouri (41) and using an order of magnitude analysis similar to those of Tennekes and Lumley (61) for the vorticity equation, Equation (3.5) takes the following form:

$$\dot{\bar{D}} + \bar{D}_{,j}\bar{U}^{j} + (\overline{DU'^{j}})_{,j} =$$

$$- 2\,\nu\, \overline{U'^{i,k} U'_{i,j} U'^{j}_{,k}} - 2\,\nu^{2}\, \overline{U'_{i,kj} U'^{i,kj}} \quad . \tag{3.13}$$

A similar equation in cartesian tensors is given by Lumley (40). Both the terms on the right-hand side of Equation (3.13) are of order one (Ref. 41) but they differ by an order $R_L^{-1/2}$. Using Lumley and Khajeh-Nouri's (41) arguments, the right-hand side of Equation (3.13) can be represented by

$$- a_4\, \overline{D^2}/\overline{q^2} + a_5\, \bar{D}\, P/\overline{q^2} \;, \tag{3.14}$$

where constants a_4 and a_5 would be different from those given by Lumley and Khajeh-Nouri. The term $\overline{DU'^{j}}$ can be modeled as follows (40):

$$\overline{DU'^{j}} = - A_{21}\ (\overline{q^2}/3)(\overline{q^2}/2)^{,j} - A_{22}\ T\ (\overline{q^2}/3)\ \bar{D}^{,j} \quad ,$$

where A_{21} and A_{22} are undetermined constants. It should be remarked here that for the highest order approximation of one, Equation (3.14) takes the following form:

$$\overline{(U'^{i,k}U'_{i,j}U'^{j}_{,k})} = - \nu\ \overline{(U'_{i,kj}U'^{i,kj})}, \tag{3.15}$$

and is similar to the Taylor's vorticity budget.

3.3.4 Comments on Rotation and Curvature Terms in Turbulence Dissipation Equation

The turbulence dissipation is a scalar. But its equation is not independent of transformation from a non-inertial frame of reference to a rotating frame as is evident from Equation (3.5). This is a further confirmation of Lumley's statement (Ref. 38) that equations of motion for a turbulent flow field do not satisfy the principle of material indifference. Considering turbulence dissipation Equation (3.5) in cartesian tensors, it turns out that the rotation terms do not vanish. The terms are:

$$2\ \nu\ [\Omega_3(\overline{U'_{3,2}U'_{1,3}} - \overline{U'_{3,1}U'_{2,3}}) + 3\ \Omega_3\ (\overline{U'_{2,2}U'_{1,2}}) -$$

$$- 2\ \Omega_3\ (\overline{U'_{1,1}U'_{2,1}}) - \Omega_3\ (\overline{U'_{2,2}U'_{2,1}})] \quad . \tag{3.16}$$

In Equation (3.16), subscript 3 denotes the axis of the machine (z) about which the rotor is rotating, subscript 2 denotes the tangential direction (y) and subscript 1 denotes the radial direction (r). For isotropic turbulence, all the correlations mentioned in Equation (3.16) are identically zero.

For non-isotropic flows, as is usually the case, an order of magnitude analysis of the rotation term can be carried out in a similar way to those carried out by Tennekes and Lumley (61) in the vorticity equation. The rotation term (10) in the Equation (3.5) is of the order of:

$$\Omega^P D/R_L{}^{1/2} \quad . \tag{3.17}$$

If the abovementioned term is to contribute to the turbulent dissipation Equation (3.13), then it has to be of the order of terms retained in the Equation (3.13), i.e.,

$$D \cdot q/L \quad . \tag{3.18}$$

Equating (3.17) and (3.18), it is possible to estimate the order of the free parameter Ω^P (angular velocity of the machine) necessary to have a significant effect on the turbulence dissipation that is

$$\Omega^P \sim (q/L)\ R_L{}^{1/2} \quad . \tag{3.19}$$

Similarly, if (3.17) has to be of the order of terms retained in Equation (3.15) then

$$\Omega^P \sim (q/L)\ R_L \quad . \tag{3.20}$$

A simple calculation for a wake of width two inches and a turbulence intensity of fourteen percent with a wake edge velocity of about fifty feet per second indicates that the order of Ω^P in Equation (3.19) turns out to be 3×10^2. Such a level of angular velocity is most commonly encountered in the field of turbomachinery. The rotation term in the turbulence dissipation equation not only affects the dissipation rate directly, but also acts indirectly through changing the mean and fluctuating velocity gradients in the turbulent flowfield.

Kolmogolov hypothesis says that all small scale structure of turbulence is isotropic at infinite Reynolds number. But due to the finite value of Reynolds number in most of the flows, the small scale structure of turbulence is not absolutely isotropic. The terms given above may be considered as a measure of the anisotropy in the small scale structure of turbulence at finite Reynolds number. From the engineering point of view the term is significant and should not be neglected.

The modeling of the rotation terms in the turbulence dissipation equation is a very complex and is a risky proposal in the absence of any direct experimental verification. But the rotation term is proportional to the anisotropy in the flow. Therefore, it can be evaluated by the following relation (considering only the largest order term in the Equation (3.16))

$$A_{33} \frac{\Omega_3 \nu}{T^2} \left(\frac{\overline{U'^2_1}}{\overline{U'^2_2}} - 1 \right) R_L^{1/2} \quad , \tag{3.21}$$

where $T = k\, \overline{q^2}/\bar{D}$, k and A_{33} are constant.

The curvature term cannot be treated in the same manner. The contribution to turbulence dissipation due to streamline curvature will always be present whether the flow is isotropic or anisotropic. However, the extent of this contribution is a function of anisotropy. The effect of curvature is hidden in Equation (3.13) through the Christoffel symbols.

3.4 Classification of Cascade and Rotor Wakes

3.4.1 Cascade Wake

Characteristics of a cascade wake can be classified and discussed under two categories depending upon the mean and turbulence properties (see Figure 4.1 for notation):

(a) Near Wake: When $\bar{U}_{zo} - \bar{U}_c \simeq \bar{U}_{zo}$ and at the wake centerline, $\overline{U_z'^2} > \overline{U_x'^2} > \overline{U_y'^2}$. The wake width increases rapidly with streamwise distance downstream of the trailing edge. Here, $\overline{U_z'^2}$, $\overline{U_x'^2}$, $\overline{U_y'^2}$ are the mean turbulence intensities along the z, x, y directions.

(b) Far Wake: When $\bar{U}_{zo} - \bar{U}_c < \bar{U}_{zo}$ (i.e. $(\bar{U}_{zo} - \bar{U}_c)^2$ is negligible compared to $\bar{U}_{zo}^2$). At the wake centerline, $\overline{U_z'^2} \simeq \overline{U_x'^2} \simeq \overline{U_y'^2}$. The wake width becomes either constant or increases very slowly.

3.4.2 Rotor Wake

Depending upon the mean and turbulence properties, a rotor wake can be classified under two categories (see Figure 3.1 for notation):

(a) Near Wake: When $\bar{U}_{so} - \bar{U}_s \simeq \bar{U}_{so}$, the difference between the turbulence intensities $\overline{U_s'^2}$, $\overline{U_n'^2}$, and $\overline{U_r'^2}$ is large. Nothing is known about their relative order of magnitude at this time. In a rotating coordinate system, the relative order of magnitude of $\overline{U_s'^2}$, $\overline{U_n'^2}$, and $\overline{U_r'^2}$ is probably the same as in a cascade or an isolated airfoil for which the effect of rotation is weak.

(b) Far Wake: (When $\bar{U}_{so} - \bar{U}_c < \bar{U}_{so}$ i.e. $(\bar{U}_{so} - \bar{U}_s)^2 << \bar{U}_{so}^2$, where $\bar{U}_c$ is the wake centerline velocity in the s and n plane.) The turbulence intensities $\overline{U_s'^2}$, $\overline{U_n'^2}$, and $\overline{U_r'^2}$ will significantly be different from a cascade and the effect of rotation will be strong.

The mean radial velocity component has not been considered in the above classification for the following reasons:

(1) The mean radial velocity component close to the trailing edge is only ten to twenty percent of the mean axial velocity components.

(2) The mean radial velocity component usually disappears in a short distance behind the trailing edge.

CHAPTER IV

ANALYSIS OF THE WAKE OF A CASCADE OF AIRFOILS

A study of the wake of a cascade of airfoils was started with the objective of discerning the effect of pressure gradient and the interference effect of adjoining blades on the wake decay. Cascade wake models may be satisfactory for stationary guide vanes or a stator. The cascade wake models occupy an intermediate position in accuracy between the isolated airfoil and the rotor wake models. In addition, a thorough understanding of the wakes of a cascade of airfoils is essential for the development of the rotor wake models.

Three regions can be identified in the wake of a cascade of airfoils depending upon the characteristics of each region. The three wake regions are as follows:

(a) The region very close to the trailing edge of the blade where the effect of thickness of the trailing edge (bluffness) dominates. This region is similar to the regions behind other bluff bodies and is characterized by large unsteadiness.

(b) The region very close to the trailing edge is followed by the near wake region where the effect of the cascade geometry dominates and the effect of bluffness of the body is considerably less. A study of this region is extremely important from the point of view of many considerations such as design, loss estimate, and noise generation in turbomachinery. The near wake region is of utmost practical importance in turbomachinery since the rotor or stator row is usually followed by another blade row spaced approximately one chord length downstream of the blade trailing edge.

(c) The near wake region is followed by the far wake region where the effect of the geometry of the body (thickness and profile, etc.) disappears. However, the spacing of the blades and flow parameters still control the wake characteristics.

The velocity distributions in the region (a) is the most complicated to analyze. Even when the free stream flow is steady, large scale unsteadiness exists in this region. However, compared to the region due to bluff bodies such as cylinders, etc., the extent of this region is likely to be small for streamlined bodies with sharp or round trailing edges unless there is flow separation at the trailing edge (as in the case of supersonic turbomachinery or heavily loaded blades). These regions are difficult to analyze mathematically. Furthermore, even the relevant flow measurement is hard to obtain in view of the unsteadiness and physical constraint of the probe dimensions.

The analyses of the regions (b) and (c) are less complicated as long as the flow is well behaved at the trailing edge of the blade. Moreover, these regions are of boundary layer nature since the vorticity shed from the surface of the airfoil is being convected in the streamwise direction and diffused by viscosity and turbulence. Since the vorticity is spreading continually, it follows that the convection is more important than streamwise diffusion and that streamwise gradients of velocity are small compared to the gradients in the lateral plane. Thus, the boundary layer type of approximations are applicable for high Reynolds number flows usually encountered in turbomachinery practice.

The mean properties of the cascade wake are completely described by the following three parameters: (i) width, (ii) wake centerline velocity, and (iii) shape of the profile. Therefore, attention will be first given to the prediction of the above mentioned parameters. Later, part of this chapter will deal with the description and qualitative estimate of the turbulence quantities.

4.1 Theoretical Considerations

Equations of continuity, mean motion, and Reynolds stress derived in generalized tensor form (Chapter III) can be written in cartesian tensors as follows:

$$\bar{U}_{i,i} = 0 \tag{4.1}$$

$$\dot{\bar{U}}_i + \bar{U}_{i,j}\bar{U}_j + (\overline{U'_i U'_j})_{,j} = - \bar{P}_{,i}/\rho + \nu\, \bar{U}_{i,jj} \tag{4.2}$$

$$\begin{aligned} &\overline{\dot{U_i U_k}} + \bar{U}_{i,j}\,\overline{U'_j U'_k} + \bar{U}_{k,j}\,\overline{U'_j U'_i} + (\overline{U'_i U'_k})_{,j}\,\bar{U}_j + \\ &+ (\overline{U'_i U'_k U'_j})_{,j} = - (\overline{U'_k P'_{,i}} + \overline{U'_i P'_{,k}}) / \rho + \nu\, [(\overline{U'_i U'_k})_{,jj} - \\ &- 2\, \overline{U'_{k,j} U'_{i,j}}] \quad , \end{aligned} \tag{4.3}$$

where P, ν, ρ are static pressure, kinematic viscosity and density, respectively and the superscript dot denotes a time derivative.

The dissipation equation with terms of the order $R_L^{-1/2}$ retained (36) can be written as

$$\dot{\bar{D}} + \bar{D}_{,j}\,\bar{U}_j + \nu\,(\overline{U'_{i,k} U'_{i,k} U'_j})_{,i} = 4\,\bar{D}^2/\overline{q^2} \tag{4.4}$$

where

$$\overline{q^2} = \overline{U'_i U'_i}, \qquad \bar{D} = \nu \, \overline{U'_{i,k} U'_{i,k}} \quad .$$

The terms $(\overline{U'_i U'_k U'_j}),_j$ and $\nu \, (\overline{U'_{i,k} U'_{i,k} U'_j}),_j$ may be modeled by simple gradient transport while the deviatoric part of $(\overline{U'_k P',_i + U'_i P',_k})$ may be expressed as (Ref. 38)

$$(\overline{U'_i U'_k} - \overline{q^2} \;\; \delta_{ik}/3) \; \frac{1}{T} \, . \tag{4.5}$$

The trace of $(\overline{U'_k P',_i} + \overline{U'_i P',_k})$ may be included in the gradient transport model of $(\overline{U'_i U'_k U'_j}),_j$. Here, T is the time scale for return to isotropy and δ_{ik} is Kronecker delta. T is given by Lumley (38).

$$T = \frac{1}{8} \; \frac{\overline{q^2}}{\bar{D}} \quad . \tag{4.6}$$

Using the above modeling, Equations (4.3) and (4.4) can be expressed as

$$\overline{U'_i U'_k} + \bar{U}_{i,j} \, \overline{U'_j U'_k} + \bar{U}_{k,j} \, \overline{U'_j U'_i} + (\overline{U'_i U'_k}),_j \, \bar{U}_j$$

$$- \, [(\overline{U'_i U'_k}),_\ell \, \overline{U'_i U'_j} \; T],_j + \frac{1}{T} \, (\overline{U'_i U'_k} - \overline{q^2} \delta_{ik}/3) \; +$$

$$+ \; 2/3 \; \bar{D} \; \delta_{ik} = 0 \tag{4.7}$$

$$\dot{\bar{D}} + \bar{D},_j \bar{U}_j - (\overline{D,_\ell \, U'_\ell U'_j \; T}),_j = - \, 4 \; \bar{D}^2/\overline{q^2} \tag{4.8}$$

For a two-dimensional cascade, wake Equations (4.1), (4.2), (4.7), and (4.8) constitute a closed set of eleven equations in eleven unknowns. If it is assumed that velocity correlation

$$-\overline{U'_z U'_x} \simeq -\overline{U'_y U'_x} << -\overline{U'_z U'_y}$$

(see Figure 4.1 for notations), then the number of equations and unknowns are reduced to nine with boundary conditions to be satisfied as follows:

$$\text{At } y = 0 \text{ and } b \; ; \; \overline{U'_z U'_y} = 0 \quad .$$

4.2 Mean Quantities

Consider Equation (4.2) for steady and incompressible flow in two-dimensional Cartesian coordinate system. Applying boundary layer approximations, and neglecting the viscous diffusion and normal stress terms which are usually small, Equation (4.2) can be written as (see Figure 4.1 for notations)

$$\bar{U}_z \frac{\partial \bar{U}_z}{\partial z} + \bar{U}_y \frac{\partial \bar{U}_z}{\partial y} + \frac{\partial \overline{U'_z U'_y}}{\partial y} = \bar{U}_{zo} \frac{\partial \bar{U}_{zo}}{\partial z} \; . \qquad (4.9)$$

Assuming self-similarity (experimental results described later confirm this) and using Townsend's (62) model, the velocity ($\bar{U}_d$) and length (ℓ) scales are introduced by the relationship

$$\bar{U}_z = \bar{U}_{zo} - \bar{U}_d \, f(y/\ell) \quad , \qquad (4.10)$$

where

$\bar{U}_d$ = velocity defect at the wake centerline.

Replace $\overline{U'_z U'_y}$ in Equation (4.9) with eddy viscosity model,

$$-\overline{U'_z U'_y} = \nu_T \frac{\partial \bar{U}_z}{\partial y} \qquad (4.11)$$

Measuring Stations: z/c = 0.012, 0.08, 0.16, 0.24, 0.32, 0.40, 0.56, and 0.72.

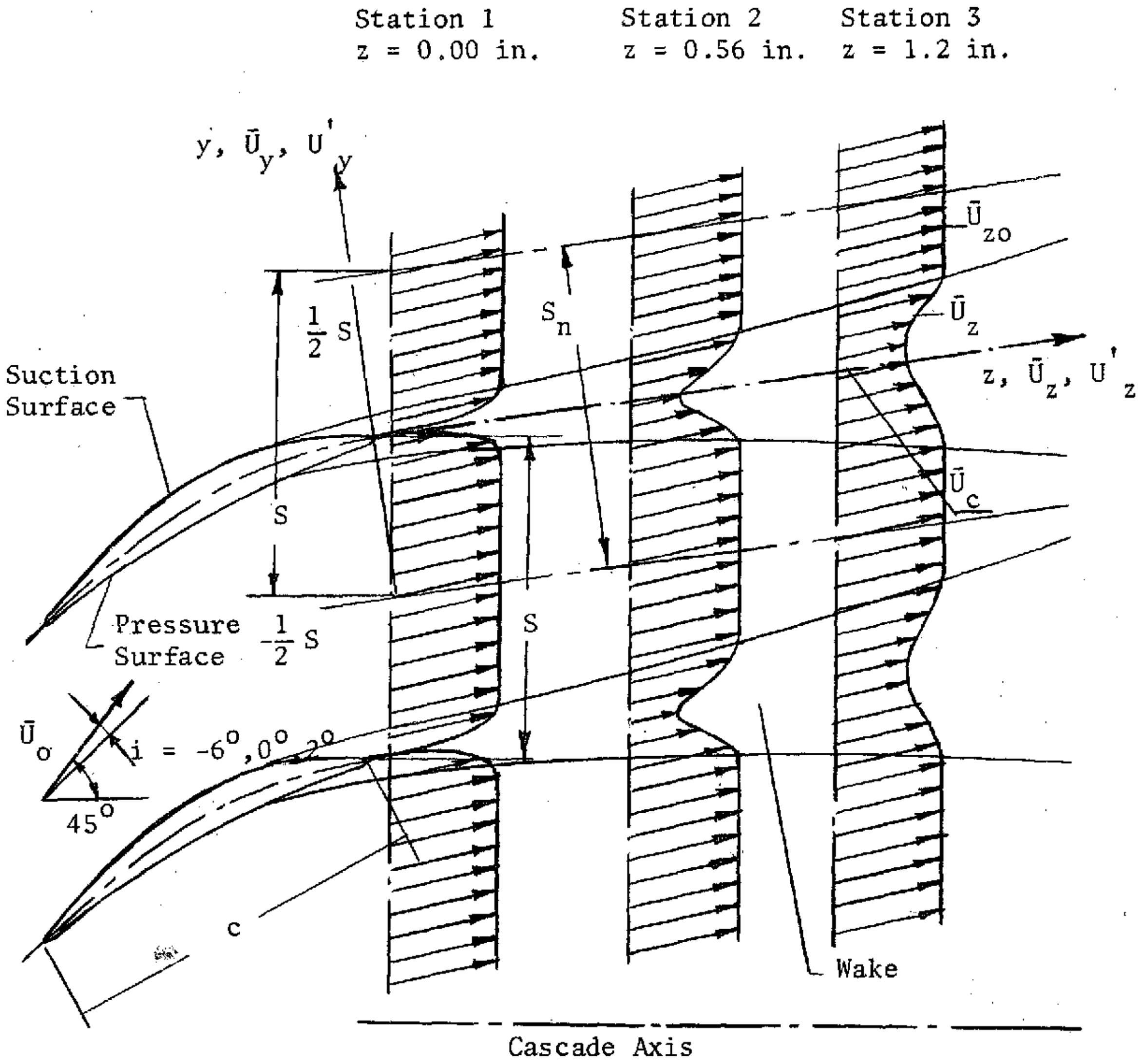

x is normal to y and z

Figure 4.1 Schematic Representation of Cascade Wake Development with Notation.

Substitute Equations (4.10) and (4.11) in Equation (4.9) and eliminate $\bar{U}_y$ in the resulting equation by the use of continuity equation [see Reference (24) for details] we get:

$$\frac{\ell}{\bar{U}_d}\frac{d\bar{U}_d}{dz}[f^2] - \frac{\ell}{\bar{U}_d^{\,2}}\frac{d(\bar{U}_{zo}\bar{U}_d)}{dz}[f] +$$

$$\frac{1}{\bar{U}_d}\frac{d(\bar{U}_{zo}\ell)}{dz}\;[\eta f'] - \frac{1}{\bar{U}_d}\frac{d(\bar{U}_d\ell)}{dz}[f']\int_0^{\eta} f d\eta$$

$$+ \frac{\nu_T}{\bar{U}_d\ell}\; f'' = 0 \quad , \qquad (4.12)$$

where

$\frac{\bar{U}_d\ell}{\nu_T} = R_d$ is Reynolds number and is assumed to be constant,

$\bar{U}_d$ = wake velocity defect at the wake centerline,

ℓ = half the wake width, and

$\bar{U}_{zo}$ = wake edge velocity .

It is easy to show that the condition of self-similarity in the mean velocity profile is satisfied only if coefficients of f, f^2, and f' are constant in Equation (4.12); i.e.

$$\frac{\ell}{\bar{U}_d}\frac{d\bar{U}_d}{dz}\;,\;\frac{\ell}{\bar{U}_d^{\,2}}\frac{d(\bar{U}_{zo}\bar{U}_d)}{dz}\;,\;\frac{1}{\bar{U}_d}\frac{d(\bar{U}_{zo}\ell)}{dz}\text{ and }\frac{1}{\bar{U}_d}\frac{d(\bar{U}_d\ell)}{dz} \qquad (4.13)$$

are constant.

4.2.1 Near Wake

When z/c is small, the first term in Equation (4.12) is small compared to other terms because the wake centerline velocity recovers to about 60 to 70 percent between z/c = 0 to z/c = 0.2 (Chapter VII). Furthermore, experimental results (Chapter VII) indicate that $\bar{U}_d \ell$ is nearly constant across the near wake. Hence, self-similarity is attained if

$$\frac{\ell}{\bar{U}_d^{\,2}} \frac{d(\bar{U}_{zo}\bar{U}_d)}{dz} = K_1 \text{ and } \frac{1}{\bar{U}_d} \frac{d(\bar{U}_{zo}\ell)}{dz} = K_2 \quad , \tag{4.14}$$

where K_1, K_2 are constants. Substituting $\bar{U}_d \ell = K_3$ (constant) in Equation (4.14), we get

$$\frac{1}{\bar{U}_{zo}^{\,3}} \frac{d(\bar{U}_{zo}\bar{U}_d)}{dz} = \frac{K_1}{K_3} = K_4 \tag{4.15}$$

and

$$\frac{1}{\bar{U}_{zo}} \frac{d(\bar{U}_{zo}/\bar{U}_d)}{dz} = \frac{K_2}{K_3} = K_5 \quad . \tag{4.16}$$

Adding Equations (4.15) and (4.16), we get

$$\bar{U}_d \frac{d\bar{U}_{zo}}{dz} = \frac{K_4 + K_5}{2} \; \bar{U}_{zo}^{\,3} \quad . \tag{4.17}$$

Let $\bar{U}_{zo} \sim \frac{1}{z^m}$; then, from Equation (4.17), we get

$$\bar{U}_d \sim \frac{1}{z^{(m+1)/2}} \text{ or } \frac{\bar{U}_d}{\bar{U}_{zo}} \sim \frac{1}{z^{(1-m)/2}}$$

$$\ell \sim z^{(m+1)/2} \quad . \tag{4.18}$$

Case I:

When m is very small ($m \simeq 0$), i.e., $\bar{U}_{zo}$ is nearly constant, then,

$$\bar{U}_d \sim 1/z^{1/2}, \ \ell \sim z^{1/2} \quad .$$

This is the case of a cylinder wake ($z > 100$ diameters), near wake of a flat plate, and isolated airfoil when placed in uniform stream without pressure gradient.

Case II:

When $m > 0$ (adverse pressure gradient), the wake centerline velocity will recover slower than Case I. This is the case in cascade of airfoils and compressors. If the pressure gradient is large enough ($m > 1$), the wake may grow rather than decay. Hill et al. (29) demonstrated this experimentally.

Case III:

When $m < 0$ (favorable pressure gradient), the wake centerline velocity will recover faster than Case I.

Considering the momentum integral relationship relating the velocity defect in the wake to the profile drag, it can be easily shown that the constant of proportionality in Equation (4.18) is a function of the coefficient of drag ($c_d^{1/2}$) of the cascade of blades (62).

Therefore, a general expression of the form

$$\frac{\bar{U}_c}{\bar{U}_{zo}} = 1 - \frac{K_o \, c_d^{1/2}}{(z/c + z_o/c)^{(-m+1)/2}} \tag{4.19}$$

will predict the wake centerline velocity recovery in the near wake of a cascade of airfoils. The value of K_o from various experimental data (including that of Chapter VII) is found to be 1.25, and z_o/c is the virtual origin. In all practical cases z_o/c for a cascade of airfoils is between 0.02 and 0.03 (Ref. 37). In the present investigation (Chapter VII), it is found to be 0.02.

Therefore, the final expression for the wake centerline velocity is

$$\frac{\bar{U}_c}{\bar{U}_{zo}} = 1 - \frac{1.25 \cdot c_d^{1/2}}{(z/c + 0.02)^{(1-m)/2}} \quad . \tag{4.20}$$

4.2.2 <u>Far Wake</u>

When $\bar{U}_{zo} - \bar{U}_c << \bar{U}_{zo}$, the wake width is nearly equal to spacing (S). Hence, $d\ell/dz = 0$. The pressure gradient effects are also negligible in the case of a cascade far wake. Therefore, from Equation (4.14), we have

$$\frac{\ell}{\bar{U}_d^2} \frac{d(\bar{U}_{zo}\bar{U}_d)}{dz} = K_6$$

or (4.21)

$$\bar{U}_d \sim \frac{1}{z} \quad .$$

The constant of proportionality can be evaluated from the momentum integral equation and from the periodic nature of the solution. It can easily be shown that the wake centerline velocity in this case recovers as

$$\frac{\bar{U}_c}{\bar{U}_{zo}} = 1 - \frac{K_7 c_d^{1/2}}{c/S} \left[\frac{1}{z/c}\right] \quad , \tag{4.22}$$

where constant K_7 is dependent upon the turbulence characteristics and the wake width. If the spacing and the turbulence characteristics at the far wake of cascade are similar to the far wake of an equally spaced row of bars, then according to Reference (54),

$$K_7 = \frac{1}{8\pi^3} \left(\frac{S}{L}\right)^2 , \tag{4.23}$$

where L is the mixing length. For low free stream turbulence (< 1%), K_7 is found to be 0.40 (Ref. 56).

The coefficient of drag given in the above analysis can be evaluated theoretically as follows: the total pressure loss in a cascade is mainly caused by (i) the viscous and turbulent stresses in the boundary layer, (ii) the flow separation, if any, at the trailing edge, and (iii) by the wake mixing downstream of a cascade. The total pressure loss coefficient (ζ) can be evaluated from the following relation [see References (18) and (55) for details]:

$$\zeta = \frac{\Delta\, P_o}{\frac{1}{2}\, \rho\, \bar{U}_a^{\,2}} = \frac{0.075}{R_e^{\,1/5}}\ c/S\ \frac{(\bar{U}_{zo_s}^{\,3} + \bar{U}_{zo_p}^{\,3})}{2\, \bar{U}_a^{\,3}} , \tag{4.24}$$

where

ΔP_o = total pressure loss,

R_e = Reynolds number based on chord length and inviscid axial velocity,

$\bar{U}_{zo_s}, \bar{U}_{zo_p}$ = inviscid maximum velocities on the blade suction and pressure, respectively, and

$\bar{U}_a$ = inviscid axial velocity at the trailing edge.

Relating the cascade geometry to the pressure losses, it can be proved (18) that the drag coefficient is

$$c_d = \zeta\ \ S/c\ \ \frac{\cos^3\beta_m}{\cos^2\beta_1} , \tag{4.25}$$

where

β_m = cascade mean air angle, and

β_1 = air inlet angle to the cascade (measured from the axial direction).

Hence, the expression for the drag coefficient is

$$c_d = \frac{0.075}{R_e^{1/5}} \frac{(\bar{U}_{zo_s}{}^3 + \bar{U}_{zo_p}{}^3)}{2\,\bar{U}_a{}^3} \frac{\cos^3\beta_m}{\cos^2\beta_1} \; . \qquad (4.26)$$

Therefore, in the final form, the wake centerline velocity recovery for the near and far wake can be written as follows:

Near Wake:

$$\frac{\bar{U}_c}{\bar{U}_{zo}} = 1 - \frac{1.25}{(z/c + 0.02)^{(1-m)/2}} \left[\frac{0.075(\bar{U}_{zo_s}{}^3 + \bar{U}_{zo_p}{}^3)\cos^3\beta_m}{R_e^{1/5}(2\bar{U}_a{}^3)\;\cos^2\beta_1}\right]^{1/2} \; . \qquad (4.27)$$

Far Wake:

$$\frac{\bar{U}_c}{\bar{U}_{zo}} = 1 - \frac{0.40}{z/c} \, . \, (S/c) \left[\frac{0.075(\bar{U}_{zo_s}{}^3 + \bar{U}_{zo_p}{}^3)\cos^3\beta_m}{R_e^{1/5}(2\bar{U}_a{}^3)\;\cos^2\beta_1}\right]^{1/2} \qquad (4.28)$$

A few important conclusions can be drawn from Equations (4.27) and (4.28) regarding the characteristics of wake decay as a function of the cascade geometry and the flow parameters. These conclusions are as follows:

(i) In the high Reynolds number flows, the wake decays much faster as compared to the low Reynolds number flows.

(ii) The high solidity (c/S) cascade wake decays faster than the low solidity cascade wake.

(iii) The wakes of a cascade of highly staggered blades decay faster than the wakes of a low staggered cascade of blades.

(iv) The wake decay law is a function of the pressure gradient. The wake decays faster in a favorable pressure gradient as compared to adverse or zero pressure gradient.

4.3 Turbulence Quantities

Turbulence characteristics of the near and far wake of a cascade are quite different. The qualitative nature of the turbulence characteristics is discussed below.

4.3.1 Near Wake

Equation (4.7) will be used to determine the qualitative nature of the turbulence intensities at the wake centerline very near the trailing edge of the cascade.

Assume that the flow is steady and the development of flow is confined to a narrow region ($\partial/\partial z << \partial/\partial y$). Then, the quantities with dots over them vanish. Near the wake centerline, $\bar{D}$, $\overline{U'^2_z}$, $\overline{U'^2_y}$, $\overline{U'^2_x}$ (and hence, $\overline{q^2}$) are nearly constant across the wake. Moreover, $\overline{U'_z U'_y} = 0$, while $d\bar{U}_z/dy$ need not necessarily be zero, but will be small. Using the continuity equation and applying the above mentioned conditions to Equation (4.7) and rearranging the terms, we get, for turbulent intensities at the wake centerline,

$$\bar{U}_c \frac{d\overline{U'^2_z}}{dz} = -\left[\frac{1}{T}\left(\overline{U'^2_z} - \overline{q^2}/3\right) - \frac{2\bar{D}}{3}\right] - 2\frac{d\bar{U}_c}{dz}\left(\overline{U'^2_z}\right)$$

$$\bar{U}_c \frac{d\overline{U'^2_y}}{dz} = -\left[\frac{1}{T}\left(\overline{U'^2_y} - \overline{q^2}/3\right) - \frac{2\bar{D}}{3}\right] + 2\frac{d\bar{U}_c}{dz}\overline{U'^2_y}$$

$$\bar{U}_c \frac{d\overline{U'^2_x}}{dz} = -\left[\frac{1}{T}\left(\overline{U'^2_x} - \overline{q^2}/3\right) - \frac{2\bar{D}}{3}\right] . \qquad (4.29)$$

Qualitatively, Equation (4.29) suggests that (since $d\bar{U}_c/dz$ is always positive):

$$\left|\frac{d\overline{U_z'^2}}{dz}\right| > \left|\frac{d\overline{U_x'^2}}{dz}\right| > \left|\frac{d\overline{U_y'^2}}{dz}\right| \quad .$$

Far downstream ($z/c > 1$), the turbulence in a wake tends to be nearly isotropic, i.e., $\overline{U_z'^2} \approx \overline{U_y'^2} \simeq \overline{U_x'^2}$. If there aren't any abrupt changes, i.e., the process is continuous from $z/c < 1$ to $z/c > 1$, we conclude that near the wake centerline

$$\overline{U_z'^2} > \overline{U_x'^2} > \overline{U_y'^2} \quad .$$

Experimentally (Ref. 49), it is found that

$$\frac{[\overline{U_z'^2}]_{max}}{[\overline{U_y'^2}]_{max}} = 4.84 \qquad (4.30)$$

near the trailing edge of the cascade of airfoils. This effect is due to the confinement of the flow by the wall. The ratio $\overline{U_z'^2}/\overline{U_y'^2}$ in the case of the near wake of a flat-plate is 3.8 (Ref. 14). It is not possible to compare these results with the available data on a cylinder (62) since the measurements in the wake of a cylinder are carried out at distances farther downstream.

4.3.2 Far Wake

In a far wake, the width of the wake becomes equal to the spacing. As a result of this, the wakes of adjacent airfoils interact and are no longer separated by the inviscid velocity profile. The peak turbulence intensity and shear stress occur away from the wake centerline. Therefore, it is not possible to calculate the variation of turbulence intensity at the wake centerline by the proposed method. However, it is possible to calculate the relative magnitude of the turbulence intensities away from the wake centerline in the region of maximum shear where the intensities are nearly independent of y. Since the wake edge velocity is nearly constant far downstream, Equation (4.7) takes the following forms (neglecting $\overline{U'_z U'_x}$ and $\overline{U'_y U'_x}$):

$$2(\overline{U'_z U'_y})\,\frac{\partial \bar{U}_z}{\partial y} = -\frac{1}{T}\,(\overline{U'^2_z} - \overline{q^2}/3) - 2\bar{D}/3, \tag{4.31}$$

$$\overline{U'^2_z}\,\frac{\partial \bar{U}_z}{\partial y} = -\frac{1}{T}\,\overline{U'_z U'_y} \ , \tag{4.32}$$

$$0 = \frac{1}{T}\,(\overline{U'^2_y} - \overline{q^2}/3) + 2\bar{D}/3 \ , \tag{4.33}$$

and

$$0 = \frac{1}{T}\,(\overline{U'^2_x} - \overline{q^2}/3) + 2\bar{D}/3 \ . \tag{4.34}$$

It is evident from Equations (4.33) and (4.34) that $\overline{U'^2_y} = \overline{U'^2_x}$. Substituting this result and Equation (4.6) in Equation (4.33) or (4.34), it can be shown that $\overline{U'^2_z}/\overline{U'^2_y} = 2$. Similarly, using these results in Equations (4.31) and (4.32), it can be shown that $\overline{U'_z U'_y}/\overline{U'^2_z} = 0.354$. From the experimental data at z/c = 0.72 (Chapter VII), it is found that

$$\frac{[\overline{U'^2_z}]_{\max}}{[\overline{U'^2_y}]_{\max}} = 2.5$$

and the wake data near half of the wake width indicates that (Figure 7.15)

$$\frac{\overline{U'_z U'_y}}{\overline{U'^2_z}} = 0.515 \quad .$$

If the turbulence properties in the cascade near and far wake are self-preserving, the turbulence quantities could be represented by the following relations (Ref. 61, 62):

$$\overline{U'^2_z} \propto (z - z_o)^{-n_1} , \tag{4.35}$$

where n depends on anisotropy. For isotropic turbulence and plane wakes, $n_1 = 1$. The experimental data on the wakes closer to the flat-plate trailing edge (Ref. 14) and cascade of airfoils (Ref. 47) give different values of $n_1 (n_1 \neq 1)$ for the decay of $\overline{U'^2_z}$ and $\overline{U'^2_y}$. This indicates that the cascade wake is not self-preserving close to the trailing edge. This is found to be in contradiction to Kiock's (32) suggestion about the cascade wake turbulence decay law which is based on the concept of self-preservation. Streamline curvature and pressure gradient, etc., are some of the other parameters that can affect the self-preservation. Further discussion on this subject is presented in Chapter VII.

CHAPTER V

ANALYSIS OF THE WAKE OF A ROTOR BLADE

Study of flow field induced by a compressor rotor can be investigated under three headings:

(a) Flow field upstream of the rotor.

(b) Flow field inside the rotor passage.

(c) Flow field downstream of the rotor.

In each of the abovementioned headings, the flow is inviscid as well as viscous in character.

In fact, the real fluid is viscid and turbulent and, though the viscous effects are predominant only in a small portion of the flow field, still they play a decisive part in the determination of the actual flow characteristics. In addition to the hub and the annulus wall boundary layers which are common to all the three cases (a), (b), and (c) the predominant viscous regions are:

In Case (a): undiffused wake of the previous row of stator blades.

In Case (b): blade surface boundary layer and the undiffused wakes if any from the previous row of stator blades which might have entered the blade passage.

In Case (c): blade surface boundary layer which develops into a wake region after the flow leaves the trailing edge of the blade.

In the investigation of compressor rotor wake characteristics, we are essentially concerned with viscous regions discussed in Case (c). These viscous regions are three-dimensional, unsteady, turbulent and anisotropic which make the analytical and experimental investigations horrendous.

Characteristics of the rotor wake are dependent on a number of variables such as the pressure gradient in the radial and the axial directions, blade spacing, blade camber, geometry of the rotating blade, free stream turbulence, speed of rotation, etc. It is certainly not possible to take into account all the abovementioned parameters in addition to the already mentioned complexities in the flow field. Therefore, the problem has to be solved step by step in coordination with the experiments to determine the gradients of normal and shear turbulence stresses which play a significant role in the analytical modeling of the mean flow characteristics.

In this chapter, the rotor wake models are developed for two types of rotor geometries. The main objective is to predict analytically the mean velocity profiles in the axial as well as the radial planes and to establish the decay laws for the viscous wakes developing downstream of the rotor blades. In addition to this, it was found desirable to qualitatively establish the turbulence characteristics of the rotor wake.

Since a stationary observer cannot visualize continuous development of a wake from a rotor, it is appropriate to transform the coordinate system from stationary to rotating where the observations can be theoretically made from the rotor. In this way, it is possible to visualize the development of a compressor wake more clearly. The equations of motion along with the continuity equation in the cylindrical rotating coordinates are given in Appendix A (Ref. 50) and in generalized tensor form in Chapter III.

In the analysis presented in Section (5.1), we have used a cylindrical rotating coordinate system while, in Section (5.2), we have used a curvilinear coordinate system. The choice of the systems is dependent upon the type of the rotor geometry considered. In the following sections, we shall consider two types of rotor geometries; one with unstaggered rotor blades and a second with staggered rotor blades.

5.1 Wakes of Unstaggered Rotor Blades

This is a very restricted case and the investigation of this geometry was undertaken solely as a basic step in the eventual analysis of the generalized rotor wake model. The analysis is applicable to unloaded or slightly loaded rotor blades and is termed as the fan wake model (Ref. 50). Although the analysis is restricted, it provides a considerable insight into the viscid and quasi-three-dimensional character of the rotor wakes.

5.1.1 Mean Velocity Profiles

In this section, mean characteristics of the near and the far wake of an unstaggered rotor blade are analyzed and simplified wake models are developed to predict the mean axial and radial velocity distribution. The cylindrical rotating coordinate system is employed for the analysis (see Figure 5.1 for notation).

Consider the equations of mean motion (A-5 to A-7 in Appendix A, Ref. 50) and apply the following assumptions:

(a) Inviscid flow outside the wake is in radial equilibrium and the absolute tangential velocity is specified.

(b) Static pressures outside and inside the wake are equal.

(c) The boundary layer thickness (δ), the mean radius (r_m) of a fan and the distance (z_1) downstream of the trailing edge, in the region of interest are such that $\delta << z_1 << r_m$.

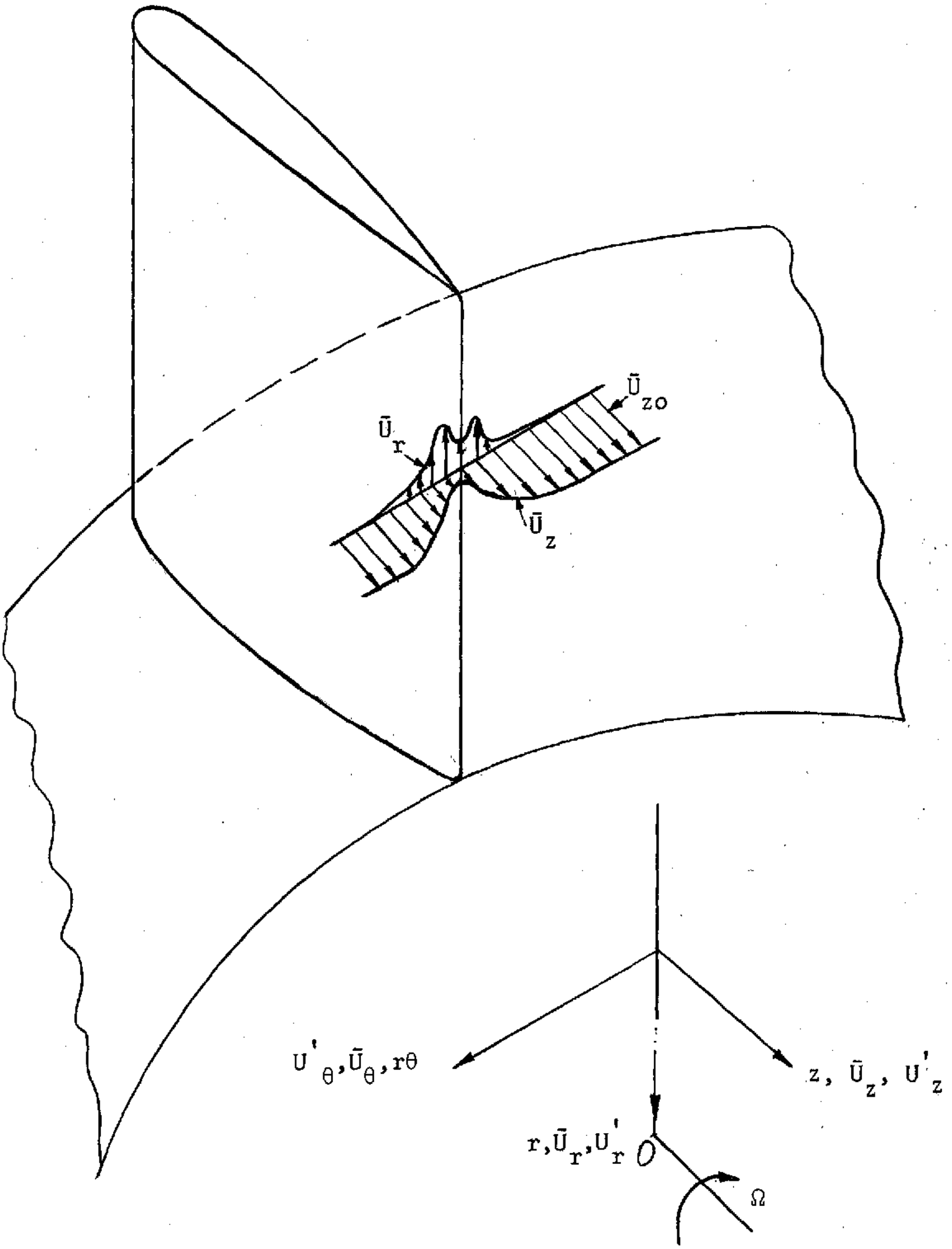

Figure 5.1 Schematic Representation of the Wakes of Unstaggered Rotor Blades and Notations Used.

(d) There is no flow separation at the trailing edge of the blade.

(e) The radial component of velocity $\bar{U}_r$, the speed of rotation (Ω) and the boundary layer thickness (δ) are such that $\Omega\,\delta \sim \bar{U}_r$ and $\Omega\,\delta << \bar{U}_{zo}$.

(f) The hub to tip ratio of the rotor is large so that the variations in the flow properties in the radial direction can be neglected.

(g) The viscous diffusion terms which are assumed to be small compared to the turbulence diffusion terms are ignored.

(h) The distance from the trailing edge where the wake defect recovers to about 60 to 70 percent of the free stream velocity is small (in terms of chord length) (Ref. 49), so that the far wake approximations are applicable and $\bar{U}_z$ is replaced by $\bar{U}_{zo}$.

Using the above assumptions together with the concept of eddy viscosity ν_T in r and z momentum equations, we get

$$\bar{U}_{zo}\frac{\partial \bar{U}_r}{\partial z} - 2\Omega\bar{U}_\theta = \nu_T\,\frac{\partial^2 \bar{U}_r}{r^2\partial\theta^2} \tag{5.1}$$

and

$$\bar{U}_{zo}\frac{\partial \bar{U}_z}{\partial z} = \nu_T\,\frac{\partial^2 \bar{U}_z}{r^2\partial\theta^2} \tag{5.2}$$

Equations (5.1) and (5.2) are valid for a blade row with zero stagger and large spacing since the rotation term in Equation (5.1) originates only due to the spreading of the wake and there is no interaction of the wakes of the one blade with the other.

If self-similarity in the mean axial velocity profile is maintained and the axial moment is conserved, then, the asymptotic solution of Equation (5.2) is

$$1 - \frac{\bar{U}_z}{\bar{U}_{zo}} = K_8 \quad (z)^{-1/2} \exp \left(- \frac{\bar{U}_{zo}}{2} \frac{(r\theta)^2}{2\nu_T z} \right) , \tag{5.3}$$

where K_8 is a constant of proportionality depending upon the blade characteristics and the turbulence structure of the wake.

Substituting Equation (5.3) in Equation (5.1) and using continuity we obtain:

$$\bar{U}_{zo} \frac{\partial \bar{U}_r}{\partial z} - \nu_T \frac{\partial^2 \bar{U}_r}{r^2 \partial \theta^2} = \frac{\Omega K_8 \bar{U}_{zo} (r\theta)}{z^{3/2}} \exp - \frac{\bar{U}_{zo} (r\theta)^2}{4\nu_T z} ,$$

with $\eta_1 = \frac{r\theta}{z^{1/2}} \left(\frac{\bar{U}_{zo}}{2\nu_T}\right)^{1/2}$.

The above equation can be rewritten as follows:

$$\bar{U}''_r + \eta \, \bar{U}'_r = \phi_1 \eta_1 \quad \exp \left(- \eta_1^2/2\right) , \tag{5.4}$$

where

$$\phi_1 = (4\Omega K_8) \left(\frac{2\nu_T}{\bar{U}_{zo}}\right)^{1/2}$$

is constant and has dimensions of velocity. Therefore, the dimensionless form of Equation (5.4) is, writing $\bar{U}_r = g \, \phi_1$,

$$g'' + \eta_1 \, g' = \eta_1 \exp \left(- \eta_1^2/2\right) \tag{5.5}$$

The general solution of Equation (5.5) constitutes a set of error functions and is written as follows:

$$g = \int \eta_1^2 /2 \exp(-\eta_1^2/2) d\eta_1 + C_1 \int \exp(-\eta_1^2/2) \, d\eta_1 + C_2 . \tag{5.6}$$

If there is no radial flow outside the wake, then the constant C_2 in Equation (5.6) is identically zero. The nature of g is now dependent upon the constant C_1 and the functions under the integral sign. There are two possibilities; in the first, the set of the error functions may be arranged to satisfy the boundary conditions such that their combination vanishes at the edge of the wake ($C_1 = -1$). The radial velocity profile in this case turns out to be antisymmetric. In the second case, the combination of the error functions does not vanish ($C_1 \geq 0$) at the wake edge. Such a situation corresponds to the secondary flow in the blade passage and is not consistent with the assumptions made in the analysis.

The analysis carried out above indicates that the wake decay law for velocity defect in the axial plane is similar to that of an isolated airfoil or a cascade of airfoils. However, the empirical constants necessary to describe the quantitative behavior of the wake velocity defect in the case of a rotor wake will be different from that of a cascade of airfoils or an isolated airfoil. The behavior of the radial velocity profile in the above analysis is surprising. It indicates that either there is no radial flow or, if there is a radial flow, it does not decay downstream of the rotor but remains self-similar.

The above analysis also indicates that it is, in general, feasible to represent the rotor wake mean velocity profiles in axial and radial planes in the following form:

$$\bar{U}_z = \bar{U}_{zo} - \bar{U}_d \, f \, (\eta_2) \tag{5.7}$$

and

$$\bar{U}_r = \phi_2 g_1 (\eta_2).$$

Consider the second case, i.e., when the wakes of adjacent blades interact. Such a situation is possible in many ways, e.g., in the case of very closely spaced blades or far downstream of the rotor. The solution of Equation (5.1) in this case will be periodic and will be similar to that of equally spaced cylinders given by Olsson (44); i.e.,

$$1 - \frac{\bar{U}_z}{\bar{U}_{zo}} = A_1 \frac{1}{z/S} \cdot \cos \frac{\pi\eta_2}{2} , \tag{5.8}$$

where $\eta_2 = 2r\theta/S$, and S is the blade spacing.

Substituting Equation (5.8) in the continuity equation, we get

$$\bar{U}_\theta = - \frac{\bar{U}_{zo}}{\pi} \frac{S^2}{z^2} \sin \frac{\pi\eta_2}{2} . \tag{5.9}$$

Substituting Equations (5.9) and (5.8) in Equation (5.1), we get, writing $\bar{U}_r = \phi_2(z)\ g_1(\eta_2)$,

$$[S \frac{\phi'_2}{\phi_2}]\ g_1 + [\frac{2\Omega}{\pi} \frac{S^3}{z^2} \frac{A_1}{\phi_2}]\ \sin \frac{\pi\eta_2}{2} = [\frac{4\nu_T}{\bar{U}_{zo} S}]\ g''_1 . \tag{5.10}$$

If the similarity exists, then the coefficients of g_1, $\sin \frac{\pi}{2}\ \eta_2$ and g_1 [terms in the square brackets of Equation (5.10)] should be constant. Therefore, the following decay laws result

$$\phi_2 \sim e^{-z/S} \quad \text{or} \quad \phi_2 \sim (z/S)^{-2} .$$

The two solutions are not identical, even though the qualitative trend is similar. The general trend of the functions is shown in Figure 5.2. Therefore, Equation (5.10) takes the following form after multiplying throughout by $\bar{U}_{zo}S/4\nu_T$, i.e.,

$$g''_1 + A_2\ g_1 = A_3 \sin \frac{\pi}{2}\ \eta_2 . \tag{5.11}$$

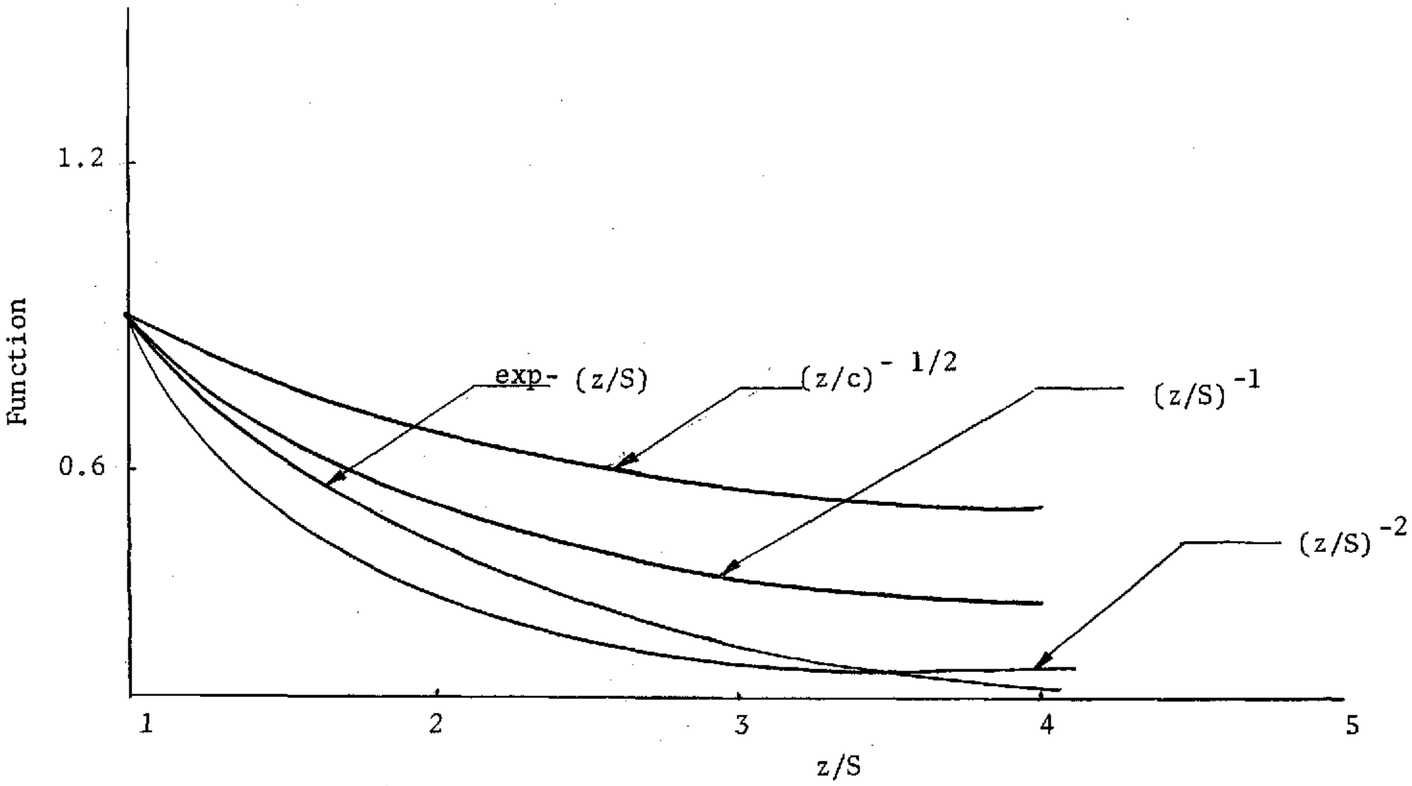

Figure 5.2 Behavior of General Functions Governing The Decay of Isolated Airfoil, Cascade and Turbomachinery Wakes.

The general solution of Equation (5.11) is

$$g_1 = A_4 \cos \sqrt{A_2}\ \eta_2 + A_5 \sin \frac{\pi}{2}\ \eta_2 \ . \tag{5.12}$$

As before [see Equation (5.6)], there are two possible profiles of $\bar{U}_r$ corresponding to function g_1. In one case, g_1 does not vanish when $\eta_2 = 1$. This case corresponds to secondary flows in the blade passage. In the second case, g_1 is antisymmetric but satisfies the boundary condition at the edge of the wake.

The above analysis indicates that the decay rate of the axial component of velocity due to interaction of wakes of adjacent blades increases compared to a single blade [Equations (5.3) and (5.6)]. The decay rate of the radial component of velocity is faster than that of the axial component of velocity.

5.1.2 Turbulence Structure

Raj and Lumley (50) have carried out an extensive investigation on the behavior of turbulence intensities in the wake of an unstaggered rotor using Reynolds stress and mean momentum equations. Some conclusions of the analysis are given below:

(i) A non-zero value of $\bar{U}'_r$ is necessary to see an effect of rotation.

(ii) If speed of rotation Ω is very small compared to $\bar{U}'_r$ then $\overline{U'^2_r} > \overline{U'^2_\theta} > \overline{U'^2_z}$.

(iii) If speed of rotation Ω is large compared to $\bar{U}'_r$ then $\overline{U'^2_\theta} > \overline{U'^2_r} > \overline{U'^2_z}$.

5.2 Wakes of Staggered Rotor Blades

A more general case is considered in this section. The rotor wake model developed in the previous section is valid only for a particular case, i.e., when the wake leaves the trailing edge of the rotor blade axially. However, that is not the case in actual compressors or turbines. In all those cases of axial flow turbomachinery where the flow leaves the trailing edge at some stagger angle, the velocity distribution in the main stream as well as in the radial direction is affected by the Coriolis forces; i.e. there is distortion of velocity profiles in both of these planes in contrast to previous cases where the Coriolis forces distort only the velocity distribution in the radial plane.

The equations of motion (see Figure 3.1 for notations) for a flow field in which the inviscid main stream direction is at an angle to the axis of the shaft of rotation can be written in the rotating coordinate system as follows (ignoring viscous diffusion and unsteady terms);

In the r-direction:

$$\bar{U}_r \frac{\partial \bar{U}_r}{\partial r} + \bar{U}_n \frac{\partial \bar{U}_r}{\partial n} + \bar{U}_s \frac{\partial \bar{U}_r}{\partial s} + 2\Omega \bar{U}_n \cos\lambda - 2\Omega \bar{U}_s \sin\lambda -$$

$$- \frac{\bar{U}_s^{\,2}}{r} \sin^2\lambda - \frac{\bar{U}_n^{\,2}}{r} \cos^2\lambda = - \frac{1}{\rho} \frac{\partial p^*}{\partial r} - \{ \frac{\partial}{\partial r} \overline{U_r'^{\,2}} + \frac{\partial}{\partial n} (\overline{U_r' U_n'}) + \frac{\partial}{\partial s} (\overline{U_r' U_s'})$$

$$+ \frac{\overline{U_r'^{\,2}}}{r} - \frac{\overline{U_n'^{\,2}}}{r} \cos^2\lambda - \frac{\overline{U_s'^{\,2}}}{r} \sin^2\lambda \}.$$

In the n-direction:

$$\bar{U}_r \frac{\partial U_n}{\partial r} + \bar{U}_n \frac{\partial \bar{U}_n}{\partial n} + \bar{U}_s \frac{\partial \bar{U}_n}{\partial s} + 2\Omega \bar{U}_r \cos\lambda + \frac{\bar{U}_r \bar{U}_n}{r} \cos^2\lambda$$

$$= -\frac{1}{\rho}\frac{\partial p^*}{\partial n} - \left\{\frac{\partial}{\partial r}(\overline{U'_r U'_n}) + (1 + \cos^2\lambda)\frac{\overline{U'_r U'_n}}{r} + \frac{\partial}{\partial n}\overline{U'^2_n} + \right.$$

$$\left. + \frac{\partial}{\partial s}(\overline{U'_n U'_s})\right\}.$$

In the s-direction:

$$\bar{U}_r \frac{\partial \bar{U}_s}{\partial r} + \bar{U}_n \frac{\partial \bar{U}_s}{\partial n} + \bar{U}_s \frac{\partial \bar{U}_s}{\partial s} + 2\Omega \bar{U}_r \sin\lambda + \frac{\bar{U}_r \bar{U}_s}{r} \sin^2\lambda$$

$$= -\frac{1}{\rho}\frac{\partial p^*}{\partial s} - \left\{\frac{\partial}{\partial r}(\overline{U'_r U'_s}) + (1 + \sin^2\lambda)\frac{\overline{U'_r U'_s}}{r} + \frac{\partial}{\partial n}(\overline{U'_n U'_s}) \right.$$

$$\left. + \frac{\partial}{\partial s}\overline{U'^2_s}\right\}, \qquad (5.13)$$

where $P^* = P - \rho/2\ \Omega^2 r^2$, and λ is the angle of the reference direction and is equal inviscid blade outlet angle.

The following assumptions are now made to simplify the equations of motion with a view to develop a simplified rotor wake model to predict the mean axial and the radial velocity profiles. The assumptions are:

1. The boundary layer does not separate from the trailing edge and the boundary layer thickness (δ), the mid-radius (r_m) and the distance (s_1) downstream which the flow is investigated are such that

$$\delta << s_1 << r_m \quad .$$

2. The turbulence of the rotor wake is weakly anisotropic and homogeneous such that

$$\overline{U'^2_n} \sim \overline{U'^2_s} \sim \overline{U'^2_r} \sim 0(\overline{u^2})$$

$$\overline{U'_n U'_r} \sim \overline{U'_r U'_s} \sim \overline{U'_s U'_n} \sim 0(\overline{u^2})$$

3. The distance from the trailing edge where the boundary layer approximations begin to apply is small.
4. The choice of the coordinate leads to

$$\bar{U}_n << \bar{U}_s \text{ and } \bar{U}_r$$

5. It is assumed that the hub/tip ratio of the rotor is large so that any variation in the radial direction is negligible.
6. The turbulent stresses can be represented by

$$\tau_{rn}/\rho = -\overline{U'_n U'_r} = \nu_T\, \partial\bar{U}_r/\partial n$$

$$\tau_{sn}/\rho = -\overline{U'_n U'_s} = \nu_T\, \partial\bar{U}_s/\partial n$$

where ν_T = eddy viscosity.

Using the above assumptions, the equations of mean motion [Equation (5.13)] can be simplified to

$$\bar{U}_s \frac{\partial\bar{U}_r}{\partial s} - 2\Omega\bar{U}_s \sin\lambda = -\frac{1}{\rho}\frac{\partial p^*}{\partial r} + \nu_T\left(\frac{\partial^2\bar{U}_r}{\partial n^2}\right) \qquad (5.14)$$

and

$$\bar{U}_s \frac{\partial\bar{U}_s}{\partial s} + 2\Omega\bar{U}_r \sin\lambda = -\frac{1}{\rho}\frac{\partial p^*}{\partial s} + \nu_T\left(\frac{\partial^2\bar{U}_s}{\partial n^2}\right) \quad . \qquad (5.15)$$

Equations (5.14) and (5.15) are non-linear equations. Therefore, only a numerical solution is possible. Since the wake defect decays to about 80 to 90 percent in a very short distance (referred to blade spacing) behind the trailing edge (Chapter VIII), it is possible to apply the far wake approximation. Also, assuming that the external pressure gradient is impressed on the wake flow,

$$\frac{1}{\rho}\ \frac{\partial p^*}{\partial s} = 0$$

and

$$\frac{1}{\rho}\ \frac{\partial p^*}{\partial r} = 2\Omega \bar{U}_{so} \sin \lambda .$$

With these assumptions, Equations (5.14) and (5.15) reduce to

$$\bar{U}_{so} \frac{\partial \bar{U}_r}{\partial s} + 2\Omega\ (\bar{U}_{so} - \bar{U}_s) \sin \lambda = \nu_T \left(\frac{\partial^2 \bar{U}_r}{\partial n^2}\right) \tag{5.16}$$

and

$$\bar{U}_{so} \frac{\partial \bar{U}_s}{\partial s} + 2\Omega\ \bar{U}_r \sin \lambda = \nu_T \left(\frac{\partial^2 \bar{U}_s}{\partial n^2}\right) . \tag{5.17}$$

Eliminating $\bar{U}_r$ from Equations (5.16) and (5.17) and writing
$\bar{U}_{so} - \bar{U}_s = \bar{U}_d\ f\ (\eta_3)$, where $\eta_3 = n/\ell$ and ℓ is half the (5.18)
wake width, the following equation results:

$$\begin{aligned}
&\left[\frac{\ell^2}{\bar{U}_d} \frac{d^2\bar{U}_d}{ds^2}\right] f - \left[\frac{2\ell}{\bar{U}_d} \cdot \frac{d\ell}{ds} \cdot \frac{d\bar{U}_d}{ds}\right] [\eta_3 f'] \\
+ \quad &\left[\frac{d\ell}{ds}\right]^2 [\eta_3^2 f'' + 2\eta_3 f'] - \left[\ell \cdot \frac{d^2\ell}{ds^2}\right] [\eta_3 f'] \\
+ \quad &\left[\frac{2\nu_T}{\bar{U}_{so}}\ \frac{1}{\ell} \frac{d\ell}{ds}\right] [\eta_3 f'''] - \left[\frac{2\nu_T}{\bar{U}_{so}\bar{U}_d} \frac{d\bar{U}_d}{ds}\right] f'' \\
+ \quad &\left[\frac{4\nu_T}{\bar{U}_{so}}\ \frac{1}{\ell}\ \frac{d\ell}{ds}\right] f'' + \left[\frac{\nu_T^2}{\ell^2 \bar{U}_{so}^2}\right] f'''' = - \left[\frac{4\Omega^2 \ell^2 \sin^2\lambda}{\bar{U}_{so}^2}\right] f,
\end{aligned} \tag{5.19}$$

where $\bar{U}_d$ is the defect in centerline velocity ($\bar{U}_{so} - \bar{U}_s$ min).

The condition of self similarity in longitudinal velocity $(\bar{U}_s)$ profile is satisfied only if the coefficients of f, $\eta_3 f'$, f'', $\eta_3^2 f''$, $\eta_3 f'''$ and f'''' are constant. This is a remote possibility in the present form of Equation (5.19). However, some simplification can be made at this point. Assume that the rotor we are considering is of high solidity, i.e., the wakes of two adjacent blades start interacting. In this case, the wake width is constant and is equal to the blade spacing (S cos λ) width. Under such circumstances, it is possible to consider half blade spacing as the characteristic length so that $d\ell/ds = 0$. This situation also corresponds to that of a far wake or high solidity rotors. Equation (5.19), with these considerations, takes the following form:

$$[\frac{S^2\cos^2\lambda}{4\bar{U}_d}\ \frac{d^2\bar{U}_d}{ds^2}]\ f - [\frac{2\nu_T}{\bar{U}_{so}\bar{U}_d}\ \frac{d\bar{U}_d}{ds}]\ f'' +$$

$$[\frac{4\nu_T^{\ 2}}{S^2\cos^2\lambda\ \bar{U}_{so}^{\ 2}}]\ f'''' = -\ [\frac{\Omega^2 S^2}{\bar{U}_{so}^{\ 2}}\ \cos^2\lambda\ \sin^2\lambda]\ f. \qquad (5.20)$$

If similarity exists, coefficients of f and f'' in the first two terms of the above equation should be constant. Hence,

$$\frac{\bar{U}_d}{\bar{U}_{so}} = \exp\ [\frac{-B_1\bar{U}_{so}S\cos\lambda}{2\nu_T}\ (\frac{s}{S\cos\lambda})], \qquad (5.21)$$

where B_1 is a constant.

It is also evident that,

$$[\frac{4\nu_T}{S\cos\lambda\ \bar{U}_{so}}]^2 << 1 \qquad .$$

So that Equation (5.20) along with Equation (5.21) can be written as,

$$(A + \phi') f + B_1 f'' = 0 \ , \qquad (5.22)$$

where A and B_1 are constants and

$$\phi' = \frac{\Omega^2 S^2}{\bar{U}_{so}^{\;2}} \ \mathrm{Sin}^2\lambda \ \cos^2\lambda \ .$$

The solution of Equation (5.22) is

$$f = A_6 \cos \{[\frac{A + \phi'}{B_1}]^{1/2} \eta_3\}. \qquad (5.23)$$

Therefore, substituting Equations (5.23) and (5.21) in Equation (5.17), we get:

$$\frac{\bar{U}_r}{\bar{U}_{so}} = \frac{\bar{U}_d}{\bar{U}_{so}} \ \frac{-2(A+\phi') \ \nu_T + \bar{U}_{so} B_1 S \cos}{B_1 \Omega \sin \lambda \ (S^2 \ \cos^2\lambda)} \cdot A_6 \cos \{[\frac{A+\phi'}{B_1}]^{1/2} \ \eta_3 \ \} \ . \qquad (5.24)$$

An estimate of the unknown constants A and B_1 can be carried out. The coefficient A can be expressed in terms of the coefficient B_1 using Equation (5.21),

$$A = B_1^{\;2} \ (\frac{\bar{U}_{so} S'}{4\nu_T})^2 \qquad (5.25)$$

where $S' = S \cos\lambda$. Applying the boundary conditions ($\eta_3 = 1$, $f = 0$) to Equation (5.23) we get:

$$(\frac{A + \phi'}{B_1})^{1/2} = \frac{\pi}{2} \ . \qquad (5.26)$$

Eliminating A from Equations (5.25) and (5.26), we get:

$$B_1^{\;2} \ (\frac{\bar{U}_{so} S'}{4\nu_T}) + \phi' = \frac{\pi^2}{4} B_1 \ . \qquad (5.27)$$

Hence, B_1 can be calculated from Equation (5.27).

For the rotor under investigation, the value of rotation parameter ϕ' is of the order of 0.02; hence the value of B_1 from Equation (5.27) can be nearly expressed as:

$$B_1 = \pi^2 / \left(\frac{\bar{U}_{so} S'}{2\nu_T}\right)^2 \quad .$$

Denoting $\bar{U}_{so}\, S'/2\nu_T$ by R_s, we get:

$$B_1 R_s^{\ 2} = \pi^2 \ .$$

Hence, the decay law for wake velocity defect [Equation (5.21)] can be written as

$$\frac{\bar{U}_d}{\bar{U}_{so}} = \exp - \left[\frac{\pi^2}{R_s} \frac{s}{S'}\right]$$

It is important to comment on the value R_s. In the regions very close to the trailing edge, the value of R_s is of order one, since eddy viscosity is very large in these regions. Farther downstream, the value of R_s is of the order of ten and remains nearly constant. Therefore, basically, we should use two decay laws governing decay of rotor wake, one closer to the trailing edge; i.e., $s/S' < 0.1$ and the other for $s/S' > 0.1$.

Although the analysis presented in this section is over simplified, it provides very important information.

1. The rate of decay of $\bar{U}_r$ is the same as that of the velocity defect in the longitudinal direction.
2. The radial velocity profile is a function of the longitudinal velocity profile, speed of rotation, rotor cascade parameters and the turbulence characteristics.

3. The decay law for the rotor wake is much different than that of a cascade or an isolated airfoil for the same case and is the fastest of the three.

CHAPTER VI

EXPERIMENTAL EQUIPMENT, METHODS, INSTRUMENTATION AND DATA PROCESSING

The primary objective of the experimental program was to study the characteristics of a cascade of airfoils and rotor wake. The study included the measurement of the mean velocity, turbulence intensity, Reynolds stress and their decay characteristics downstream of the blade trailing edge. All the measurements were carried out in a stationary frame of reference. The abovementioned experimental information was needed, not only for an understanding of the wake characteristics, but also for the simplification of the various terms in the equations of motion used in the theoretical formulation of the wake models and verification of the assumptions made in the theoretical analysis. The measurements also aided in the evaluation of some constants in the analytical solution which otherwise could not be determined from the boundary conditions or other theoretical considerations.

6.1 Cascade Wake Experiment

6.1.1 Equipment Used in the Experiment

6.1.1.1 Subsonic Cascade Tunnel. A subsonic cascade tunnel with porous side walls, designed and constructed at the ARL (Applied Research Laboratory), The Pennsylvania State University was used in the experiment. The cascade set up is shown in Figure 6.1. The cascade test section permits a blade span of fourteen inches. Details on subsonic cascade tunnel design is given in Reference (25). The

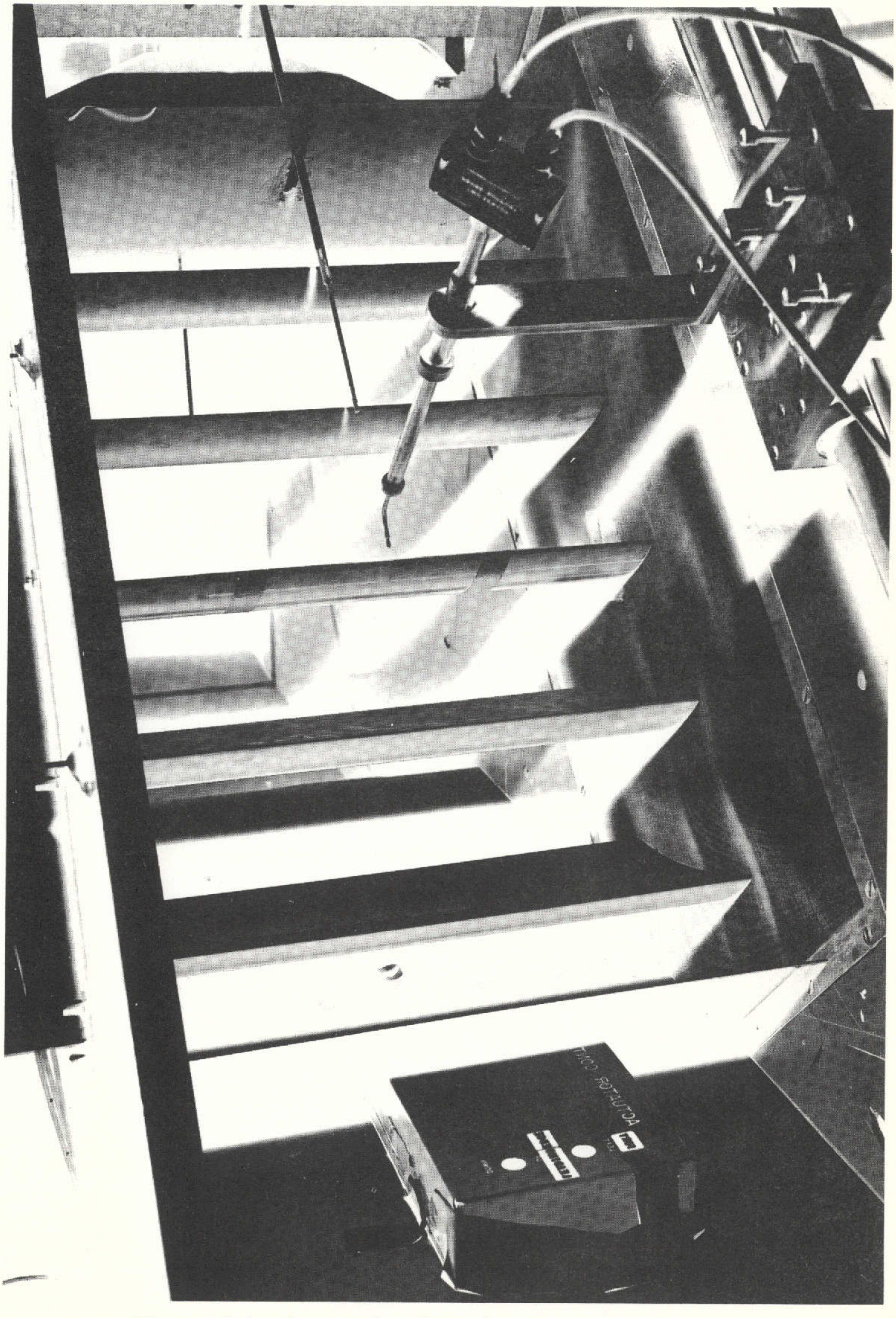

Figure 6.1 Set Up for Cascade Wake Measurements.

condition of two-dimensionality and its practical realization during the test was carried out according to Reference (11).

6.1.1.2 Cascade Blade Configuration. The profile of the blades used in the cascade is shown in Figure 6.2. The blade span and the chord are 14 and 7 inches respectively. The blade profile was designed at the ARL. The blade profile (of trailing edge loaded type) is very similar to the NACA-65 ($8A_2I_{8b}$) 10-blade section. The only difference lies in the thickness distribution. The ARL blade profile is thinner in the loading edge region to reduce the tendency of high surface velocities due to the blade thickness blockage. The maximum thickness is near the fifty-five percent chord position and its value is ten percent of the chord length. The cascade was operated with the following characteristics:

Number of Blades = 7

Inlet Angle (β_1) = 45°

Solidity (c/S) = 1.505

Incidence (i) = -6°, 0°, $+2^\circ$

Turning Angle (θ_4) = 22°, 28°, 30°

The turbulence quantities were measured only for -6° incidence. The velocity of the free stream flow was 90 ft/sec and Reynolds number based on the chord length was 3.2×10^5. The free-stream turbulence level was 0.16 percent.

6.1.1.3 Traversing Mechanism. Two different types of traversing mechanisms were used for measurements of mean velocity profile (with a five-hole prism-shaped probe) and turbulence quantities

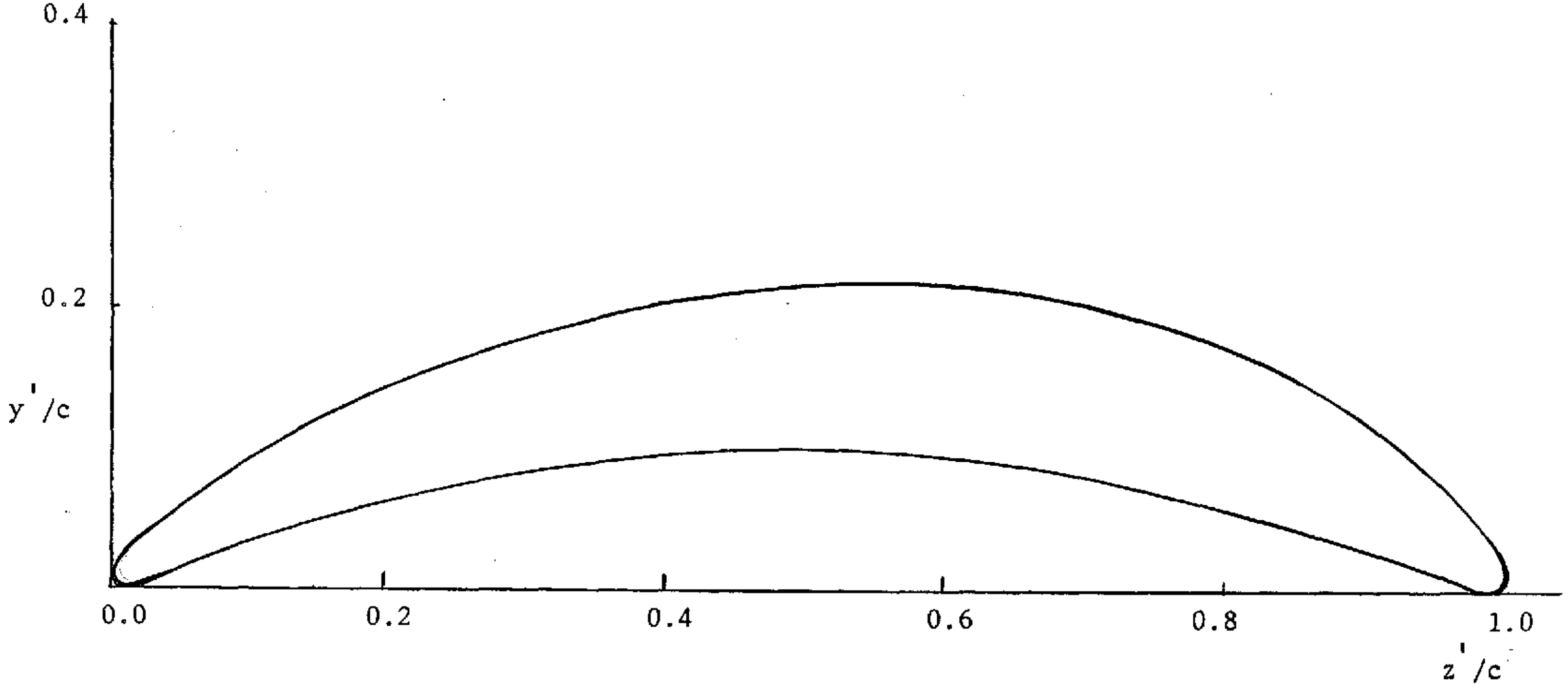

Figure 6.2 Profile of Blade Used for Cascade Set Up.

(with cross wire). Both types of traversing mechanisms could control the three motions of the probe:

(i) Traversing the probe across the wake (y direction).

(ii) Varying the axial location of the probe (z direction).

(iii) Rotating the probe about its own axis.

All these motions were controlled mechanically. The traversing mechanisms are shown in Figure 6.1. Both the traversing mechanisms were made rigid enough so that the vibrations and the consequent fluctuating voltages were small.

6.1.2 Experimental Method and Instrumentation

6.1.2.1 Measurements of Mean Velocity Profile. A five-hole prism-shaped probe manufactured by the United Sensors was used to measure total and static pressures. Three pressure transducers of Validyne Type DP15 (with pressure range ± 0.5 P.S.I.D.) along with a Validyne Type CD15 carrier demodulator were used to transfer mechanical to electrical signals. The pressure transducers along with carrier demodulator were calibrated against a precision manometer. The first transducer was used to measure the difference between the total and the static pressure $(P_T - P_s)$ upstream of the cascade. The second pressure transducer was used to measure the difference between the total and the static pressure $(P_T - P_s)$ downstream of the cascade. The third pressure transducer was used to locate the direction of the flow so that the difference between the measurements of two static pressure holes is zero. All the three pressure transducers were fed to a Serial Converter Type 264 of the Non-Linear Incorporation. The Serial Converter was connected to a Friden Flexowriter Type FI for printing the data.

The measurements were taken at five axial stations (see Figure 4.1). The probe was traversed across the full wake width so as to clearly determine the wake edge and wake centerline. The calculations for mean velocity in the wake non-dimensionalized with respect to local edge velocity were performed according to the following relation:

$$\frac{\bar{U}_z}{\bar{U}_{zo}} = \left[\frac{P_T - P_s}{(P_T - P_s)_{zo}}\right]^{1/2} . \tag{6.1}$$

6.1.2.2 Measurement of Turbulent Quantities. The turbulence quantities ($\overline{U'^2_z}$, $\overline{U'^2_y}$, and $\overline{U'_z U'_y}$) were measured across the wake at eight different axial locations (see Figure 4.1). The block diagram for turbulence instrumentation is shown in Figure 6.3. A two sensor cross wire with nearly equal resistances (10.85, 10.84 ohms) and length to diameter ratio $(\ell_1/D_1) = 250$ was used for this purpose. The calibration of the cross wire was done in the inviscid core of a jet. The signals from the cross wires were fed to two DISA Type 55D01 constant temperature anemometers. An overheat ratio of 1.8 was used in the anemometers. No linearizers were used since the level of turbulence intensity was less than twenty percent. Moreover, the addition of linearizers in the circuit introduces an error of $\pm$ 2%. Also, the calibration curve $E^2 - E_o^2 \propto \bar{U}^{1/2}$ was linear in the velocity range used in the experiment. The output from Channel 2 of the anemometer was fed to the DISA Type 55D25 auxiliary unit so as to inverse the input signal. The signals were then fed to a DISA Type 55D71 battery operated dual summing unit. The summing unit introduced a gain of 0.33. The two outputs e_1 and e_2 from the summing unit were fed to two DISA

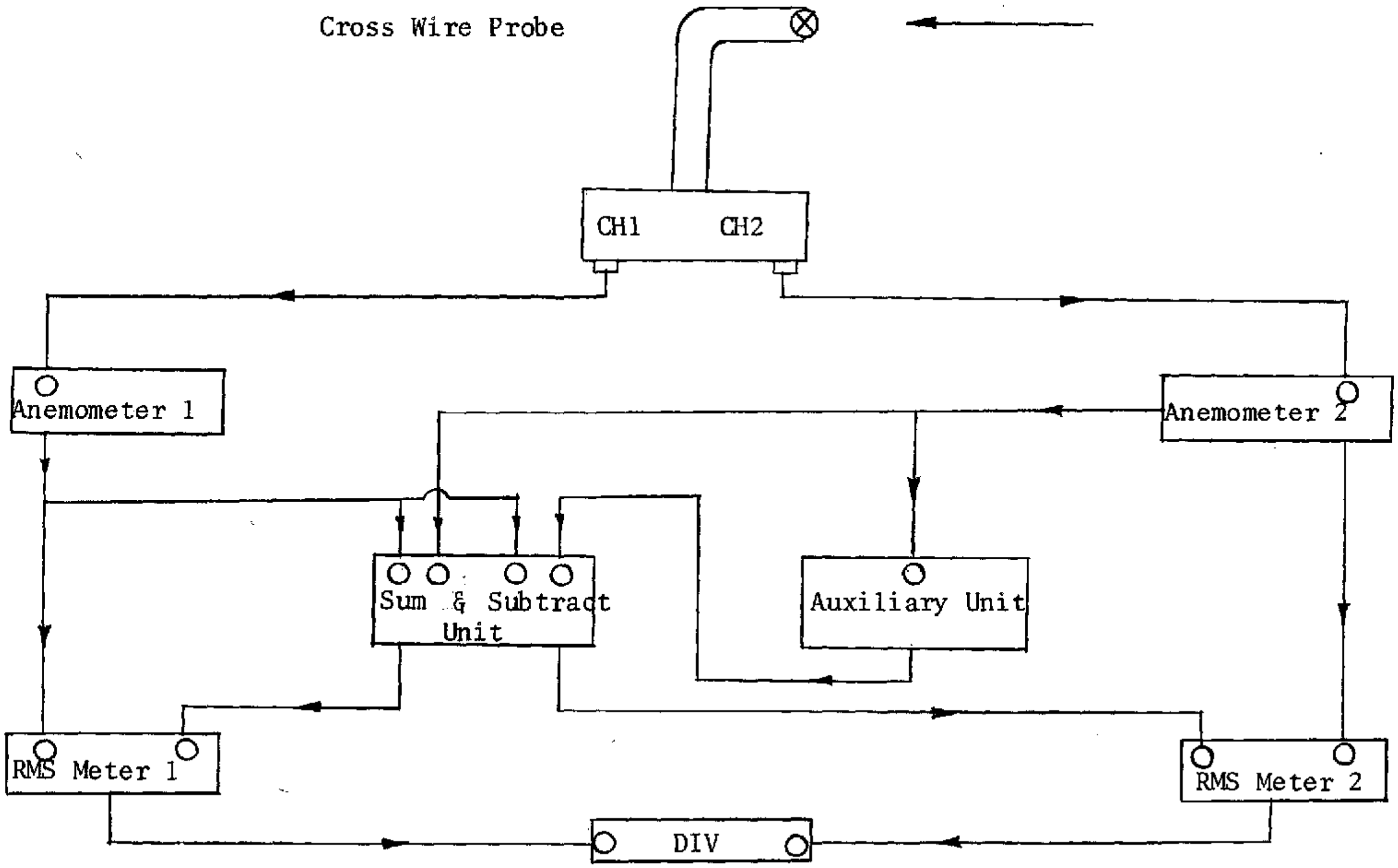

Figure 6.3 Block Diagram of Turbulence Instrumentation for Cascade.

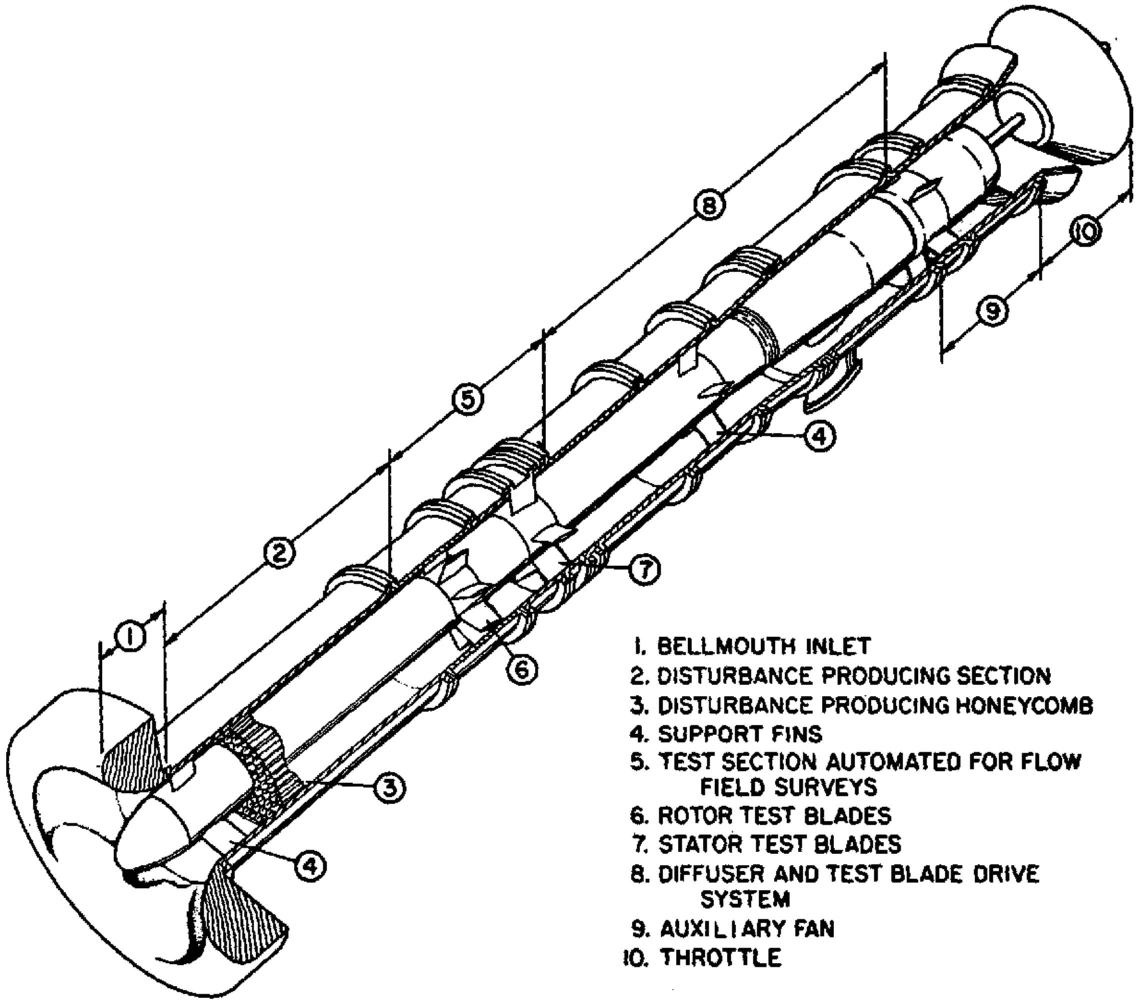

Figure 6.4 Axial Flow Research Fan Facility of the Applied Research Laboratory.

lift on the rotor can be produced by controlling the relative speed of the fan and the rotor.

A twelve-bladed rotor used in the test program is shown in Figure 6.5. The rotor blades are symmetrical airfoils with a zero camber. The blades are twisted from the hub to the tip so that the blades have no loading at all the radial locations. The rotor blades are of circular arc (British profile C1) base profile with a maximum thickness-to-chord-length ratio (t/c) of 0.1 at 33 percent chord point. The blades have a chord of 6 inches and a span of 5.9 inches. The operating conditions of the rotor were:

Speed of rotation (rev/min) = 1010

Blade chord/spacing ratio (c/S) at the mean radius = 1.98

Flow coefficient = 0.58

Stagger angle at the mean radius = 45^o

Coefficient of drag (c_d) = 0.012.

A photocell mounted on the rotor shaft was used to measure the rotor speed to an accuracy of 1/10 of a revolution per minute.

6.2.1.2 Probes Used in the Experiment. Three types of probes were used in the experiment: spherical heat static pressure probe, a single sensor hot-wire probe, and a three-sensor hot-wire probe.

The static pressure probe used in the experiment was manufactured by the Flow Corporation. The diameter of the sphere was 1/8 inch. The probe has two separate rings mounted on the sphere to stabilize the wake region by tripping the boundary layer on the sphere. The probe was insensitive to yaw and pitch angles in a wide range of variation ($\pm 40^o$).

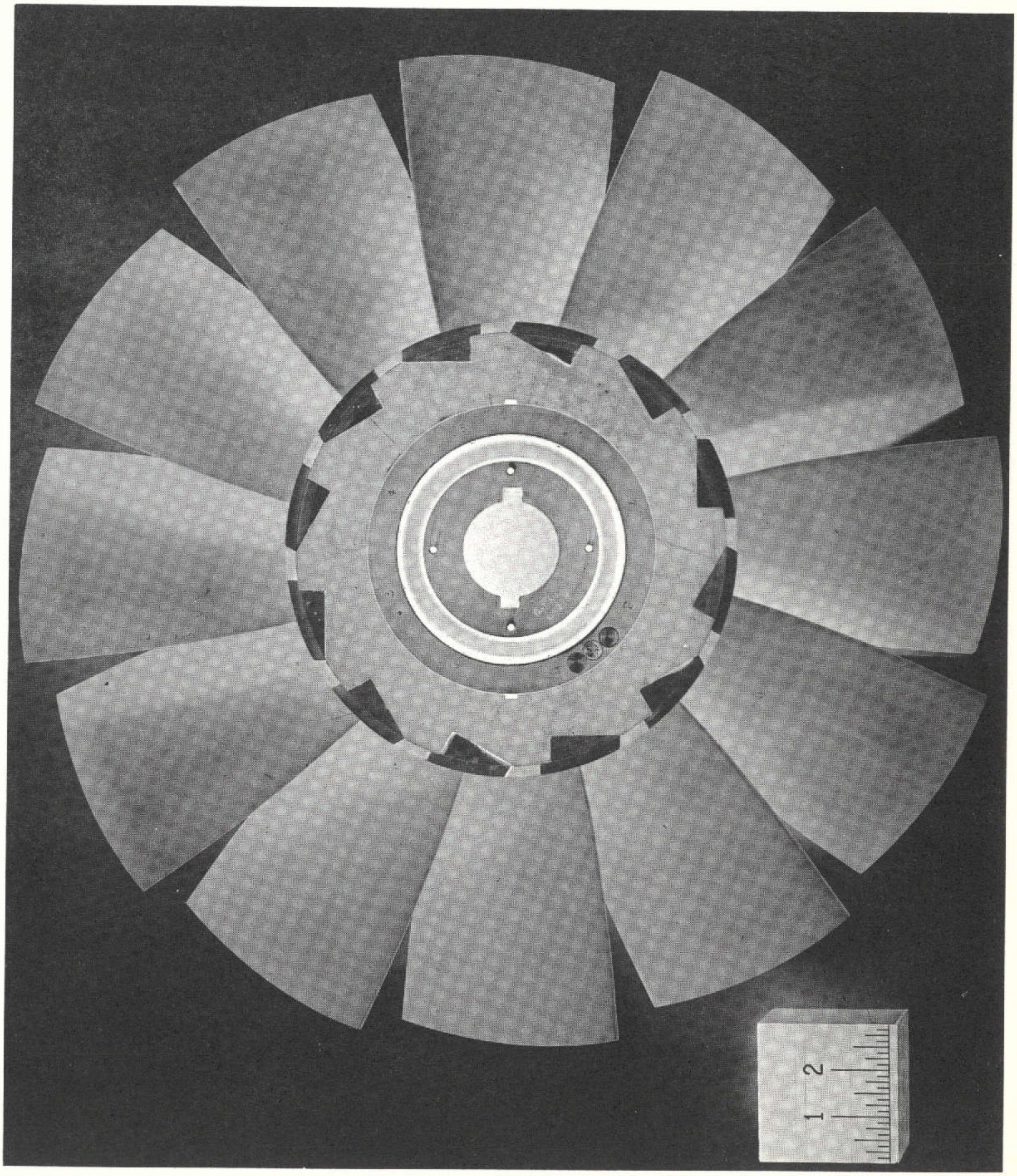

Figure 6.5 Axial Flow Research Fan Test Rotor with Twelve Blades Installed.

The single- and three-sensor hot-wire probes used in the experiment were manufactured by the Thermo-Systems, Inc. The length-to-diameter ratio (ℓ_1/D_1) was 400 with resistance of 6.72 ohms. The three-sensor hot-wire probe used in the experiment is shown in Figure 6.6. The probe had three sensors orthogonal to each other. The material of the sensors was tungsten. The length-to-diameter-ratio (ℓ_1/D_1) of all the sensors was 400 with resistances of 7.02, 7.08, and 7.05 ohms. The leads from the sensors were properly shielded.

6.2.1.3 Traversing Mechanism. A traversing mechanism was built for traversing the probe upstream and downstream of the rotor. The traversing mechanism was mounted on the outercasing of the rotor and is shown in Figure 6.7. The principle function of this mechanism was to locate the probe direction such that the vortex line of the cone formed by the three sensors of the hot-wire probe always pointed in the direction of the machine axis. This adjustment was carried out with the help of two allen head screws 1 and 2 (see Figure 6.7). The pointer 3 could slide only in a vertical slot along with the probe holder and the probe could be held in any vertical position by the allen head screw 2. This arrangement avoided the circumferential motion of the probe holder while changing the radial location. The probe and the probe holder had marks which could be easily aligned to give a known direction to the sensors of the probe relative to the machine axes. The probe was located in the probe holder with the help of two allen head screws.

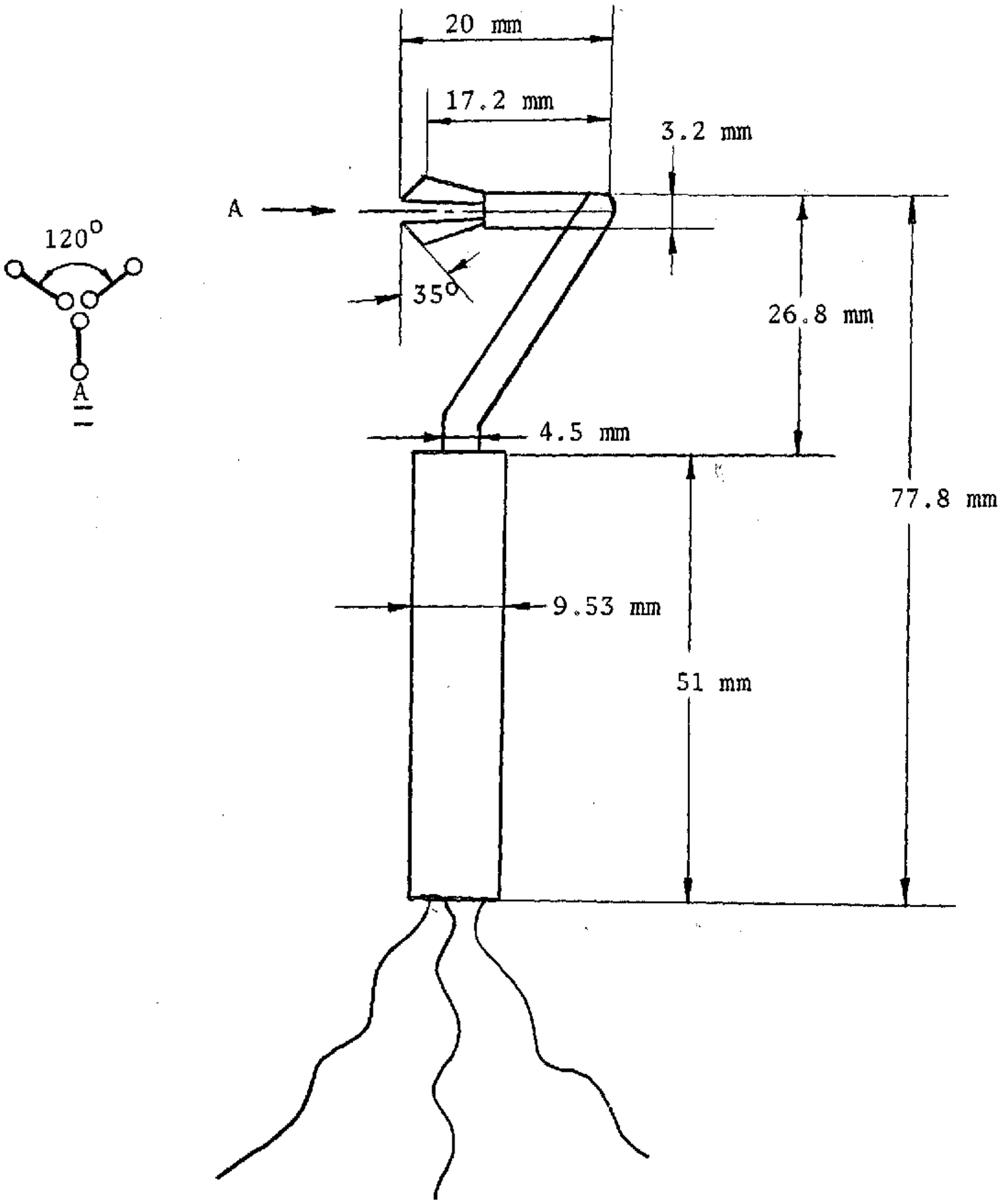

Figure 6.6 Three Sensor Hot Wire Probe Used in the Rotor Wake Measurements.

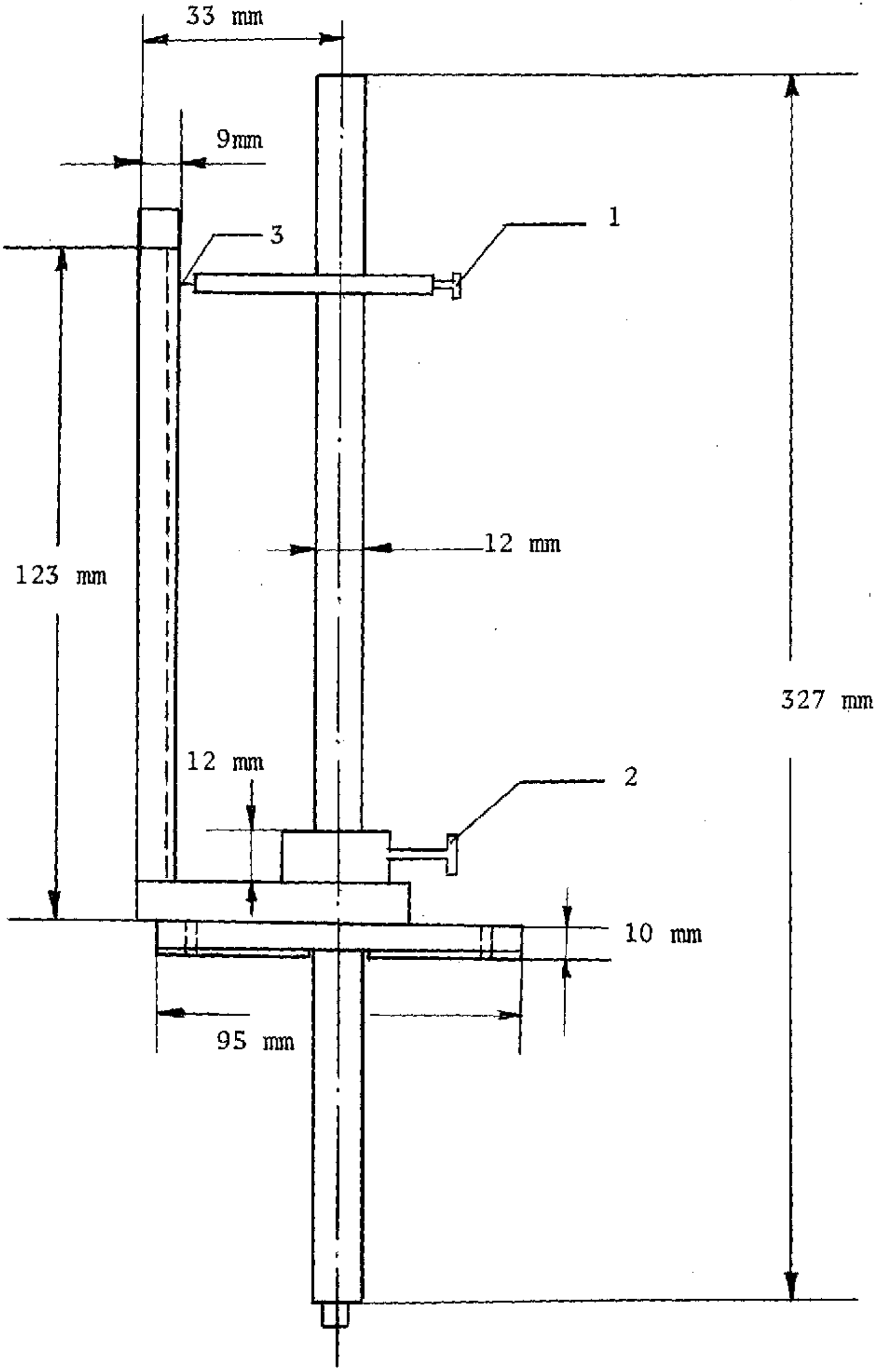

Figure 6.7 Traversing Mechanism Used for Rotor Wake Measurements.

A second traversing mechanism was built to be used for carrying out future measurements in a relative rotating frame of reference. Description of this mechanism is given in Appendix B.

6.2.1.4 Tape Recorder. A magnitic tape recorder/reproducer CPR-4010 of Bell and Howell was used to record the A.C. signals from the three channels of the anemometers and a pulse signal from photo cell. The tape recorder used was a 14-channel system and was set to operate as an FM recorder. The recording was carried out at a tape speed of 15 i.p.s. The choice of the speed was based on the maximum frequency limit on the wake data required. The tape speed accuracy was ± 0.15%. The signal-to-noise ratio was 44 dB. The center frequency of recording was 54 khz and the frequency of the signals to be recorded could vary from 0 to 10 khz. The band width adjustment was of the wide band group. The amplitude of input signal had to be kept from ± 0.5 to ± 10 volts peak to peak for ± 40% deviation. The system drift after 10 minutes of warmup was ± 0.5% of full deviation in 8 hours with a temperature variation of 20°C in the operating range of 0° to 50°C.

6.2.1.5 Analog to Digital Conversion Unit (ADC Unit). For conversion of analog to digital data, ADC unit of Pastoriza Electronics, Inc., was used. It has seven channels for analog input voltages and each channel may be set to a gain of 8, 4, 2, or 1 by adjusting the input gain selectors. The ADC unit transmits the digital data into an Ampex digital tape recorder which writes each data point as one byte or 8 bits on the IBM tape in binary format. This gives a 7 bit resolution, which corresponds to a range of integer numbers between 1 and 255. With the gain set to one, the input peak-to-peak acceptable voltage is +4 to -4 volts. The sampling rate of the ADC units is 36,000 data points per second. The record length can be set by the Bytes/Record Switch from 4K to 512K (K=100). Before the mathematical operations can be performed on the digitized data, it is necessary to decode the digitized tape. The reason is that IBM operates in integer mode in two or four bytes and in real mode in four bytes.

6.2.2 Experimental Method and Hot-Wire Equations

6.2.2.1 Static Pressure Measurements. The static pressure (P_S) measurements were carried out using a spherical probe described in the Section (6.2.1.2). The probe measured the average pressure in the wake of the sphere and the wake pressure (p_W) was then correlated to the free-stream static pressure at that point. The probe was precalibrated in a known static pressure and was evaluated as follows:

$$P_S - P_W = K' (P_T - P_S)$$

where K' is a calibration constant and P_T is the total pressure. The value of K' could be evaluated from the calibration curve Figure (6.8). In the present experiment, the probe was connected to a pre-calibrated pressure transducer whose one end was open to the atmosphere. The reading on the integrating digital voltmeter was read as P_W-P_a. The static pressure is measured at five axial locations and six radial locations corresponding to each axial location downstream of the rotor (Figure 6.9).

6.2.2.2 Hot-Wire Measurement Method. The hot-wire measurements (with the three-sensor probe) and data processing technique are

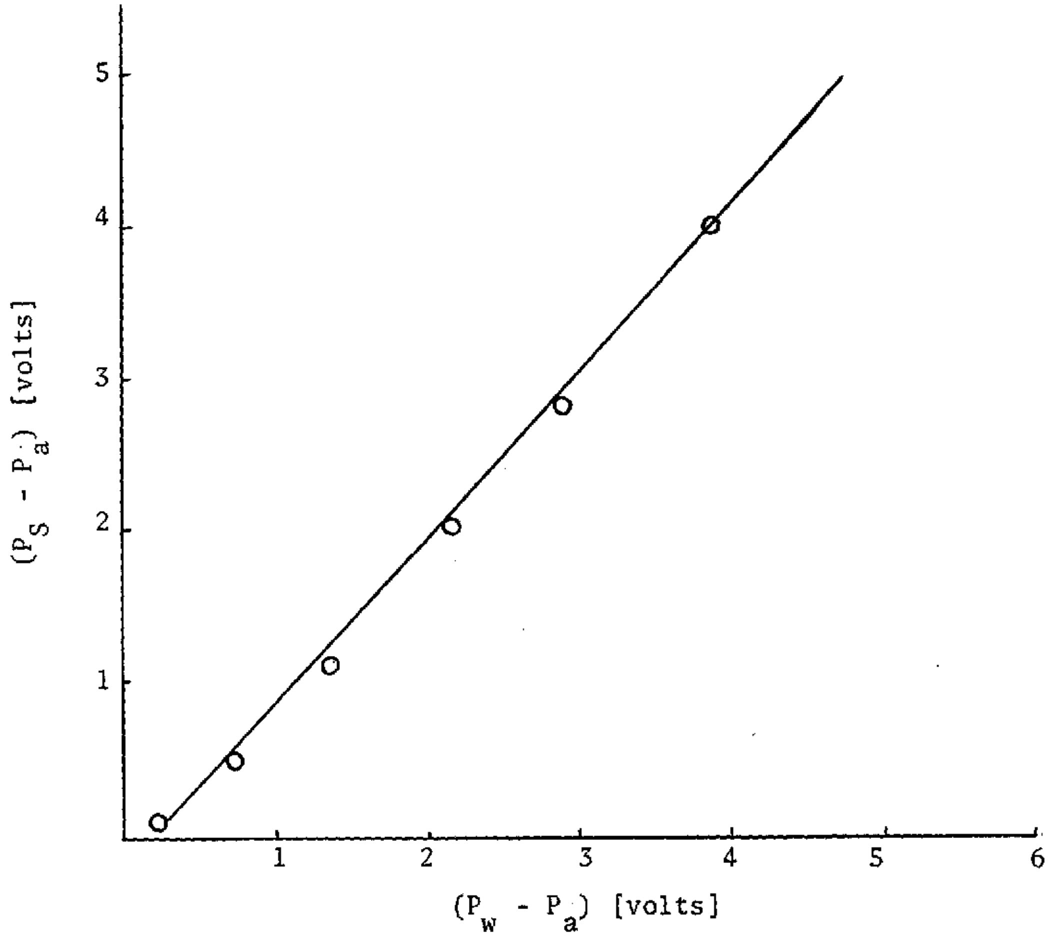

Figure 6.8 Calibration Curve for Three-Dimensional Static Pressure Probe.

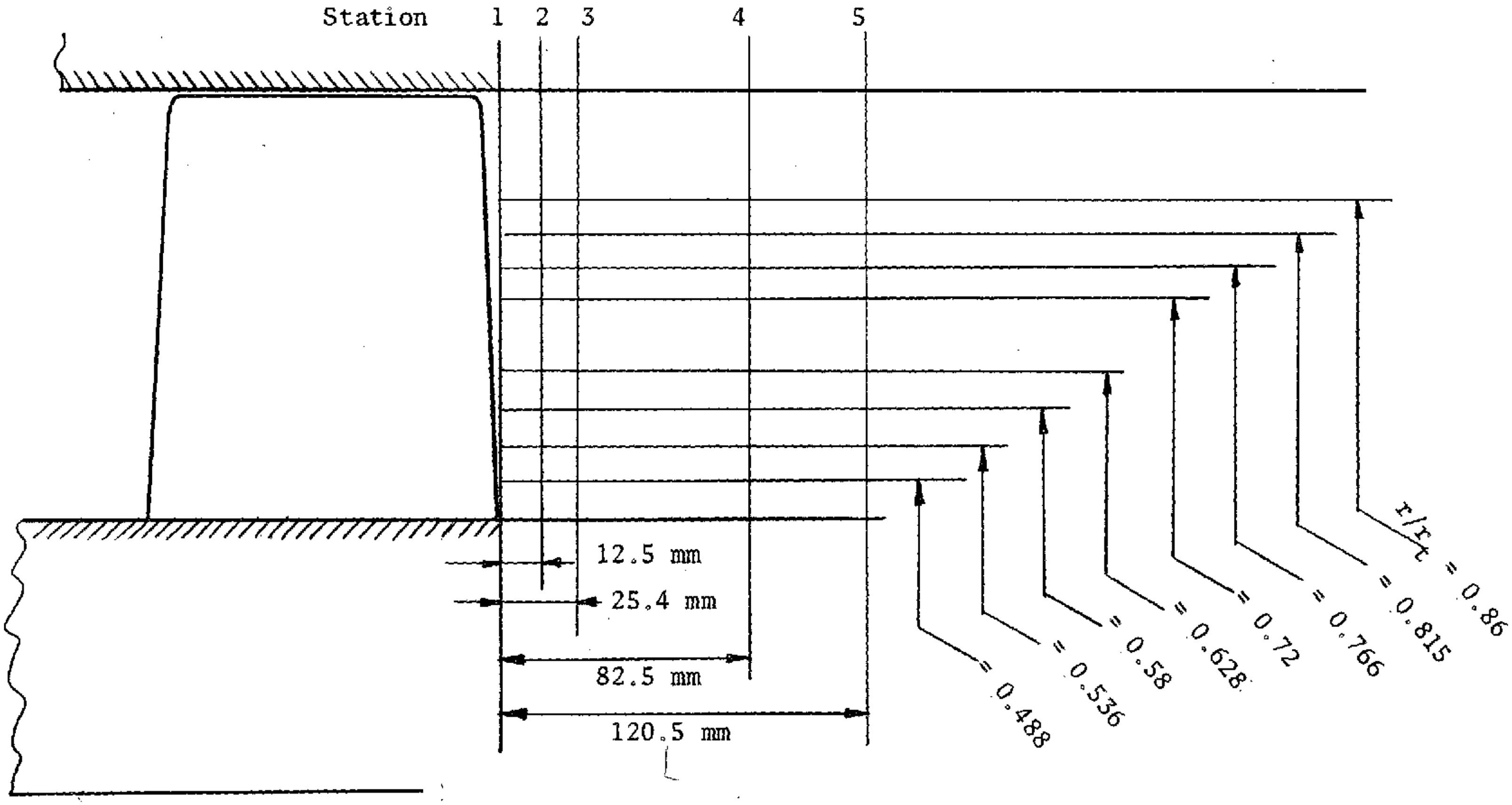

Figure 6.9 Measuring Stations for Rotor Wake Experiment.

similar to that used by Lakshminarayana and Poncet (33). Additional information on the experimental details and the difficulties encountered in the data processing is described in the following sections.

The block diagram of instrumentation used for the measurement with a three-sensor hot-wire probe is shown in Figure 6.10. The measurements were carried out at five axial locations and at eight radial locations corresponding to each axial location (Figure 6.9). Electrical signals from the three-sensor probe were fed to the three DISA Type 55D01 constant temperature anemometers. An overheat ratio of 1.5 and a frequency gain of 4 was set. A frequency gain of 4 provided a range of frequency in data from 16 to 100 khz. No linearizers were used since the measurements with a single sensor hot-wire probe (Chapter VIII) indicated that the disturbance levels were much below twenty percent.

In addition, single sensor hot-wire measurements were carried out with an objective to measure the overall disturbance levels upstream and downstream of the rotor and to study the effect of rotation on the overall disturbance level (Chapter VIII).

The output from the hot-wire anemometers was divided into two branches. One of these went to the integrating digital voltmeter and the second branch was fed to an amplifier. The readings from the integrating digital voltmeter were read and noted while the signals from the amplifiers were memorized in a tape recorder. It is extremely important that the amplification does not introduce a phase lag between the three anemometer signals. Therefore, three identical amplifiers were used for amplifying the signals from the three anemometers. Secondly, the amplification of the signals is dependent upon the acceptable range of the input recording voltage of the tape recorder

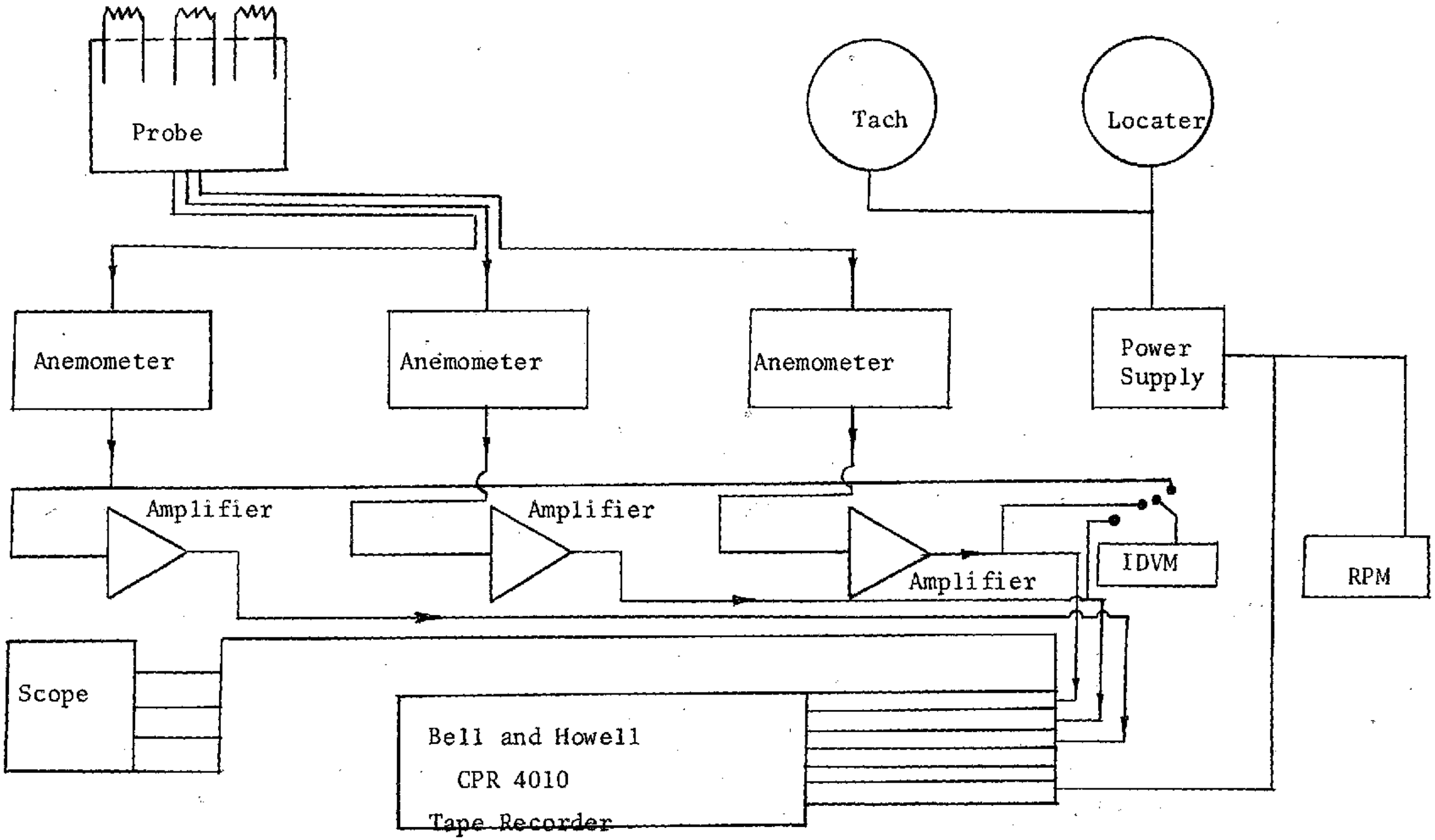

Figure 6.10 Block Diagram of Turbulence Instrumentation for Rotor Wake Measurements.

[see Section (6.2.1.4)]. For details on the alignment of the probe direction see Section (6.2.1.3).

6.2.2.3 Hot-Wire Equations. Standard hot-wire equations were used to process the data. The well-known King's Law was used to convert voltages ($E_{cm\ell}$) to cooling velocities ($V_{cm\ell}$),

$$V_{cm\ell} = \left(\frac{E^2_{cm\ell} - E_o^2}{B_2}\right)^{n_2} \qquad (6.4)$$

where subscript c corresponds to cooling, m corresponds to an instantaneous point and ℓ corresponds to probe sensor. Constants E_o^2 and B_2 are obtained from the calibration curve (Figure 6.11) of the three-sensor hot-wire probe. The value of n_2 was found to be 0.5. The instantaneous cooling velocities ($V_{cm\ell}$) sensed by the sensors 1, 2, and 3 (Figure 6.12) were referred to V_{cm1}, V_{cm2}, and V_{cm3} respectively. Knowing V_{cm1}, V_{cm2}, and V_{cm3}, it is possible to determine the absolute value of the instantaneous velocity vector $\underline{V}_{om}$ by applying the cosine law to all the three sensors of the probe separately and, adding the resulting equations we get:

$$|\underline{V}_{om}| = \left(\sum_{\ell=1}^{3} \frac{V_{cm\ell}}{2+k_9^2}\right)^{0.5} . \qquad (6.5)$$

Deviation from the cosine law correction is also incorporated in the above derivation. In Equation (6.5), K_9 is a constant whose value depends upon length-to-diameter ratio, (ℓ_1/D_1), of the sensor. The value of K_9 for the sensor used ($K_9 = 0.19$) in these experiments was derived from Reference (9) and is the same for all the sensors. Once the absolute value of $\underline{V}_{om}$ is known, it is possible to establish the direction of $\underline{V}_{om}$ relative to the sensors of the probe; i.e.,

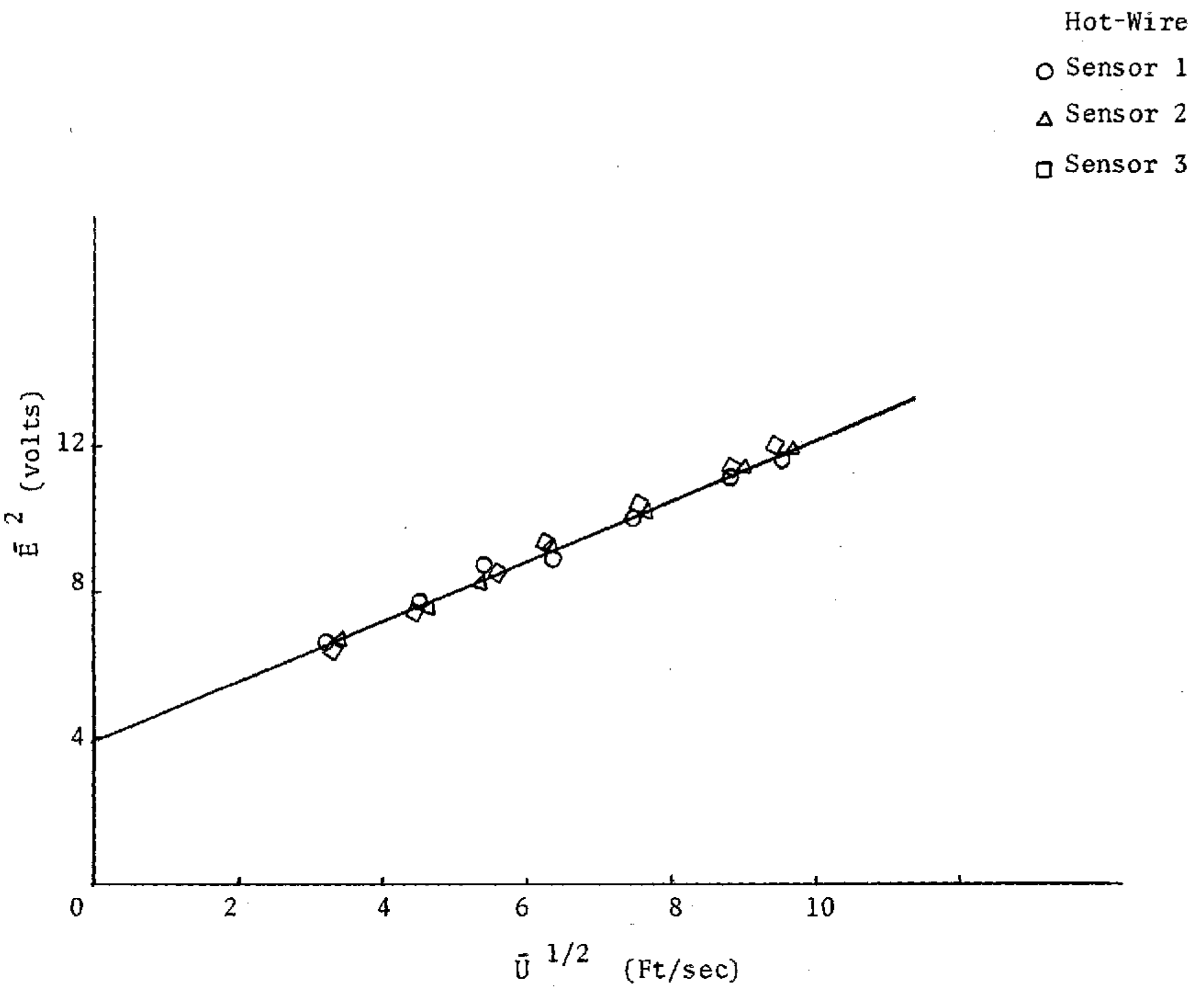

Figure 6.11 Calibration Curve for Three-Sensor Hot-Wire Probe.

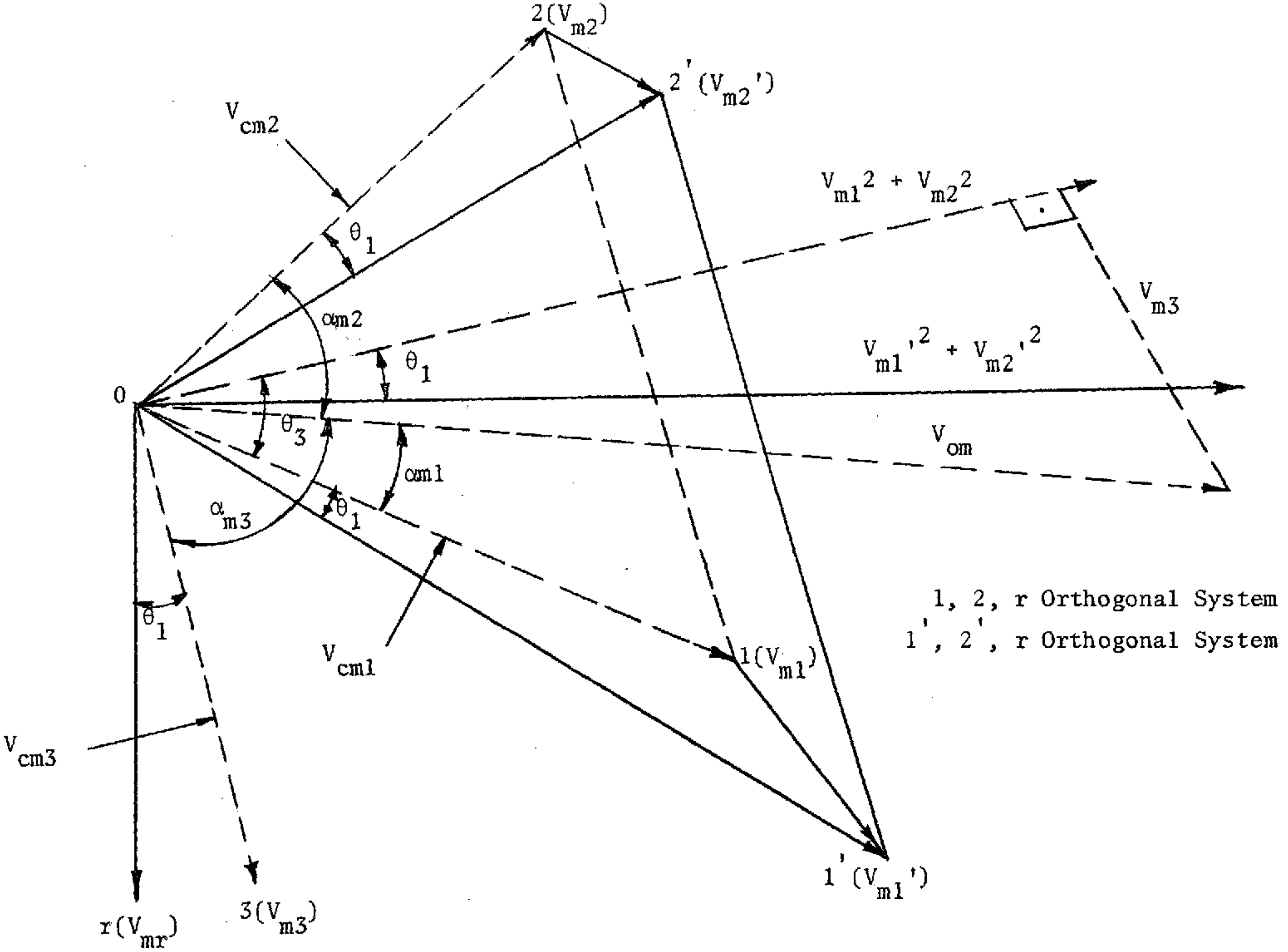

Figure 6.12 Coordinate Transformation and Symbols Used in Hot-Wire Data Processing.

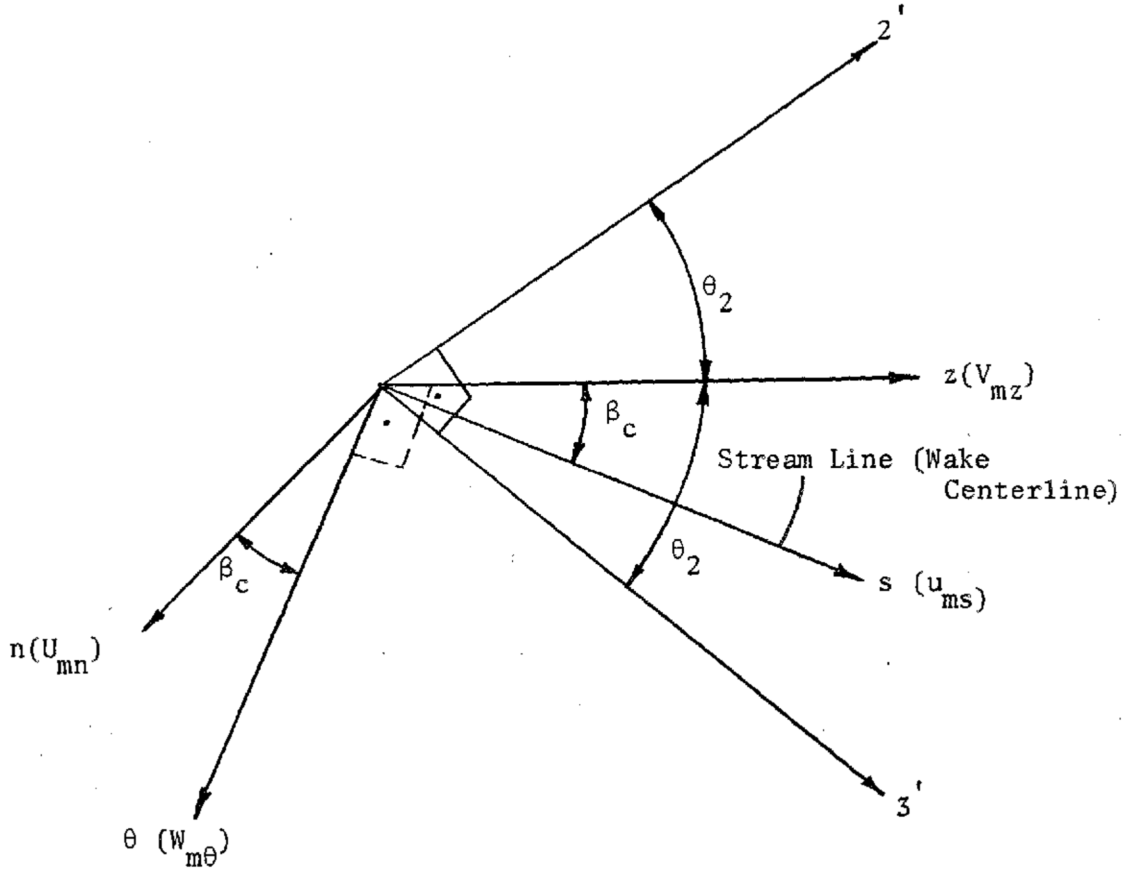

Figure 6.12 (continued) Coordinate Transformation and Symbols Used in Hot-Wire Data Processing.

$$\sin \alpha_{m\ell} = [(\frac{V_{cm\ell}}{|\underline{V}_{om}|})^2 - K_9{}^2/1 - K_9{}^2]^{0.5} \quad . \tag{6.6}$$

Also, it is possible to obtain components of the absolute velocity vector along the three-sensors of the probe; i.e.,

$$V_{m\ell} = |\underline{V}_{om}| \cos \alpha_{m\ell} \quad . \tag{6.7}$$

There is a need for the transformation of the velocity components obtained so far (Figure 6.12) to the coordinate axes of the machine (r, z, and y) for design purposes and to the coordinate axes (s, n, and r) used in the theoretical analysis. This, involved in the present case two transformations (Figure 6.12, a and 6.12, b).

(a) The plane containing wires 1 and 2 is rotated by an angle θ_1 so that wire 3 is in the radial direction. The magnitude of angle θ_1 is 35° (obtained from probe configuration).

(b) The plane containing wires 1 and 2 is rotated about the radial direction by an angle θ_2 so that the probe sensors point in the direction of the machine axes. Here θ_2 is 45° (obtained from the probe configuration).

If 1, 2, and 3 are the directions of the three sensors of the probe (Figure 6.12) which form an orthogonal coordinate system, then the first transformation of the component of velocities give

$$\begin{aligned} (V_{m1}'^2 + V_{m2}'^2)^{0.5} &= (V_{m1}^2 + V_{m2}^2)^{0.5} \cos \theta_1 + V_{m3} \sin \theta_1 \\ V_{mr} &= -(V_{m1}^2 + V_{m2}^2)^{0.5} \sin \theta_1 + V_{m3} \cos \theta_1 , \end{aligned} \tag{6.8}$$

where

$$(V_{m1}^2 + V_{m2}^2)^{0.5} = |\underline{V}_{om}| \sin \alpha_{m3} \ .$$

If θ_3 is the angle, the velocity $|\underline{V}_{om}| \sin \alpha_{m3}$ makes relative to the wire 1 then,

$$\cos \theta_3 = \cos \alpha_{m1} / \sin\alpha_{m3}$$

and

$$\sin \theta_3 = \cos \alpha_{m2} / \sin\alpha_{m3} \quad .$$

Hence

$$V_{m1}' = (V_{m1}'^2 + V_{m2}'^2)^{0.5} \cos \theta_3$$

and

$$V_{m2}' = (V_{m1}'^2 + V_{m2}'^2)^{0.5} \sin \theta_3 \quad .$$

From the probe configuration, it is clear that V_{m1}' and V_{m2}' make an angle (θ_2) of 45° to the machine axes.

Therefore, the component of the tangential and axial velocity are given by the following relations, respectively:

$$V_{m\theta} = 0.707 \, (V_{m1}' - V_{m2}')$$

and

$$V_{mz} = 0.707 \, (V_{m1}' + V_{m2}') \qquad (6.9)$$

In the relative coordinate system we have:

$$W_{mz} = V_{mz} \, ,$$

$$W_{m\theta} = \Omega r - V_{m\theta}$$

and

$$W_{mr} = V_{mr} \quad . \qquad (6.10)$$

In the streamwise coordinate system we have:

$$U_{ms} = W_{mz} \cos \beta_c + W_{m\theta} \sin \beta_c$$

and

$$- U_{mn} = W_{mz} \cos \beta_c - W_{m\theta} \cos \beta_c \qquad (6.11)$$

where

$$\tan \beta_c = \bar{W}_{m\theta}/\bar{W}_{mz}$$

β_c is the flow angle, which the wake centerline velocity makes with the machine axis. $\bar{W}_{m\theta}$ and $\bar{W}_{mz}$ are time averaged relative tangential and axial velocities.

6.2.3 Data Processing

The flow at the exit of a rotor (viewed from a stationary frame of reference) is three-dimensional and unsteady with periodic as well as random components as shown in Figure 6.13. The extent of three dimensionality and the statistical properties of turbulence depend, to a large extent, on the Reynolds number, Mach number, Rossby number and the type of machinery. Any component of the wake velocity consists of a turbulent fluctuation V' superposed on a mean velocity $\bar{V}$ (ensemble average of velocities at any particular location of blade passage or wake). The periodicity is $2\pi/\Omega$, where Ω is the angular velocity of the rotor. The block diagram for processing the data from the tape recorder is shown in Figure 6.14. The undermentioned steps were followed in processing the data:

Step 1: Digitizing the analog data using ADC unit is a very crucial step, since it determines the number of data points (M) we can get in one blade passage. Depending upon the necessity of the number of data points, the speed of the tape recorder can be adjusted according to the following equation:

$$M = 2\pi f/\Omega n \quad , \qquad (6.12)$$

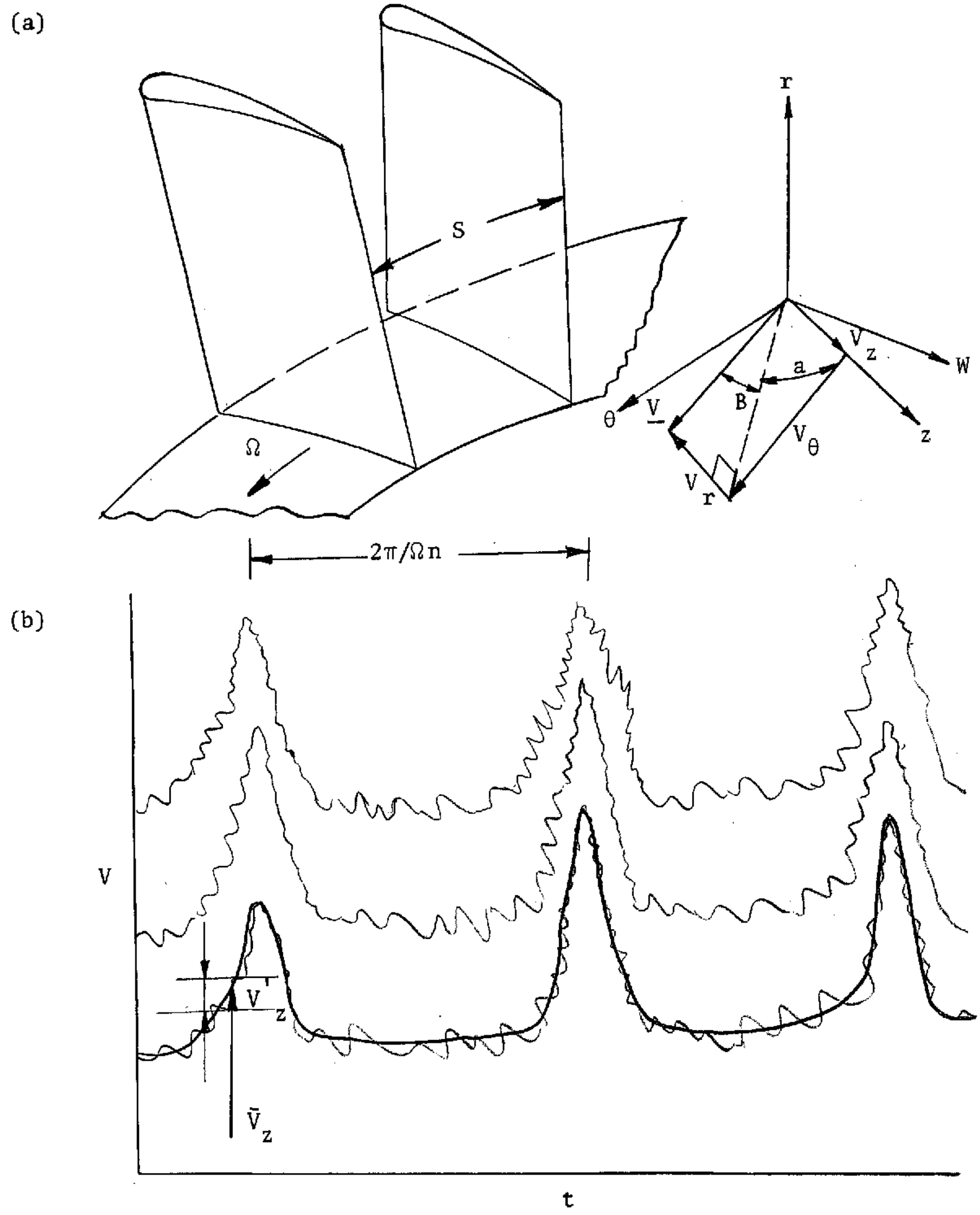

Figure 6.13 Flow Field Behind a Rotor.

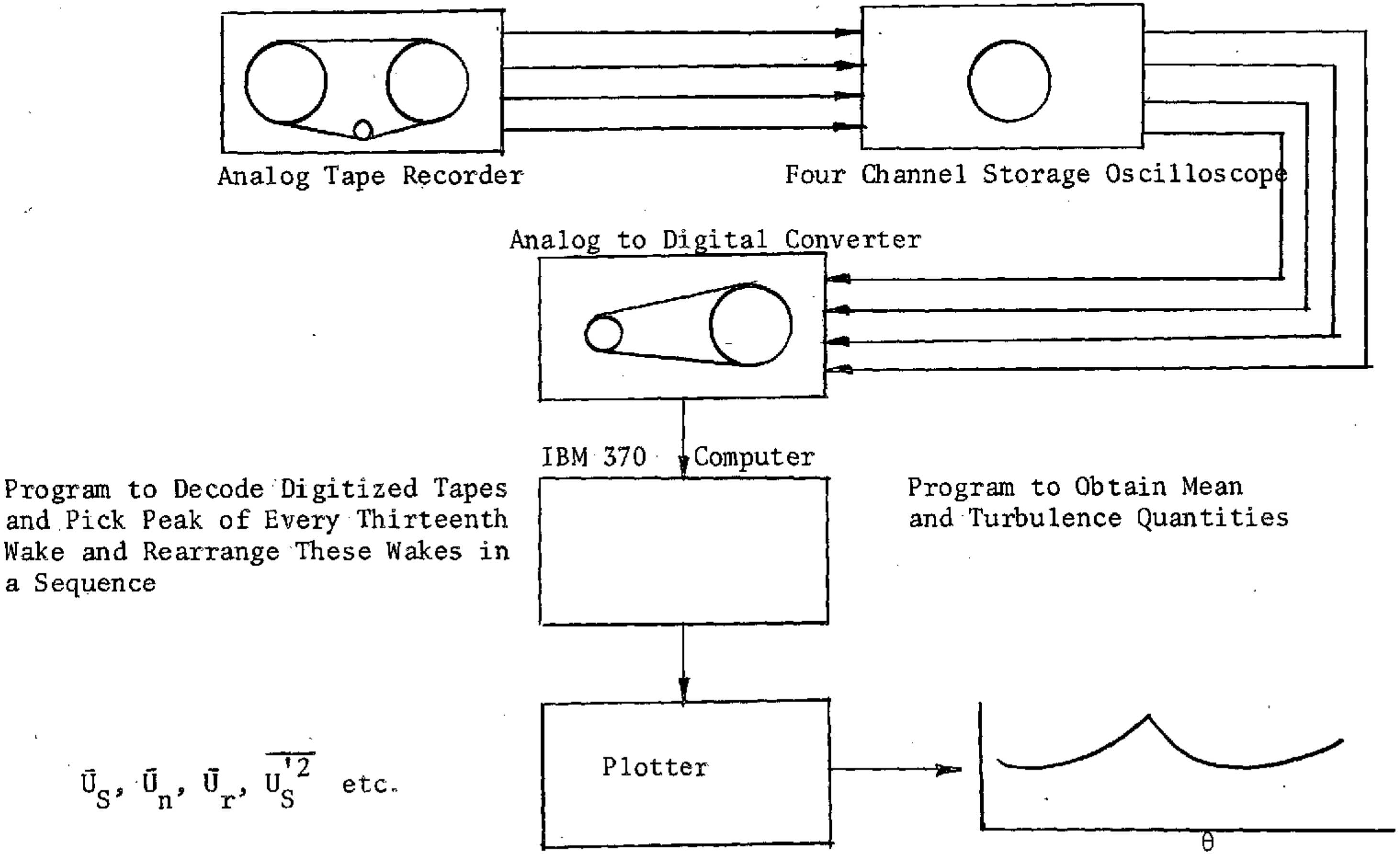

Figure 6.14 Block Diagram for Rotor Wake Data Processing.

where f is the sampling frequency of the ADC unit. The ADC unit used in the Department of Aerospace Engineering of The Pennsylvania State University has a fixed digitizing speed of 9000 words per second per channel. Hence, the number of data points within blade passage would be 44.5 at $\Omega = 105.71$. However, this number of data points was not enough to locate the wake. Hence, the tape recorder speed was reduced to 1/8 of the speed at which data was recorded and the number of records made per set of data was 128. The number of wakes to be processed was 160.

Step 2: A computer program (Appendix A) was used to copy the digitized tapes on a nine track labelled tape for use in the IBM 370. The program was developed to write every thirteenth wake which assures that the sampling points belong physically to the same passage, because the number of rotor blades were 12.

Step 3: For derivation of the mean velocity, turbulence intensity and Reynolds stress another computer program was written. The number of sampling points across the wake chosen for this purpose was 301; 150 on the one side of the peak and 150 on the other side of the peak. The computer program follows the undermentioned steps:

(i) Conversion of all voltages to velocities using King's Law.

(ii) Using Equation (6.7), determine the velocity components along the three-sensors of the probe.

(iii) Knowing the angles, which the probe sensors make with the machine axes, coordinate transformations of velocity components are carried out according to Equations (6.8 to 6.11). One set of Equations (6.10) transfer velocity components in the relative coordinate system while the second set of Equations (6.11) transfer the velocity components in the streamwise coordinate system. The data is processed in both coordinate systems.

(iv) Pointwise point ensemble average is carried out (33). Only the relative coordinate system is considered. The technique follows similarly for the streamwise coordinate system. Consider mth point on the recorded wake. If N_1 is the total number of similar wakes, then the averaged velocity along the z direction is obtained as follows:

$$\tilde{W}_{mz}\ (r,z,\theta_o) = \sum_{N=1}^{N=N_1} W_{mz}(r,z,\theta')/N_1,$$

where

$$\theta' = \theta_o + 2\pi N,$$

θ_o is the location of the blade passage at which the mean velocity is evaluated. Similarly other two components of velocity can be evaluated.

This approaches the time averaged value given below for large values of N_1 i.e.,

$$\bar{W}_{mz}(\underset{\sim}{r}) = 1/T \int_o^T W_{mz}\ (\underset{\sim}{r},t)\ dt. \tag{6.14}$$

where T is the period of integration.

The error involved in the estimate is given by the following expression (39, 33):

$$\text{error} = \sqrt{\overline{q^2}/\bar{V}_{om}/\ N_1}\quad , \tag{6.15}$$

where $\overline{q^2}/\bar{V}_{om}$ is the overall turbulence intensity and N_1 is the number of wakes.

(v) The components of fluctuating velocities are obtained as follows:

$$W'_{mz} = W_{mz} - \tilde{W}_{mz} \tag{6.16}$$

(vi) The turbulence intensities and Reynolds stress correlations are obtained as follows:

Turbulence Intensity:

$$\widetilde{(W'_{mz})^2} = \sum_{N=1}^{N=N_1} (W'_{mz})^2/N_1 \quad . \tag{6.17}$$

Reynolds Stress:

$$\widetilde{W'_{mz}W'_{m\theta}} = \sum_{N=1}^{N=N_1} W'_{mz}W'_{m\theta}/N_1 \quad . \tag{6.18}$$

Similarly, the other two components of turbulent intensity and Reynolds stress are evaluated.

The technique described in steps IV, V, and VI is similarly applied in the streamwise coordinate system to evaluate the components of mean velocity, turbulence intensity and Reynolds stress.

The overall error involved in evaluating the mean velocity, turbulence intensity and Reynolds stress is within two, five, and fifteen percents respectively.

CHAPTER VII

EXPERIMENTAL RESULTS AND COMPARISON WITH PREDICTIONS FOR CASCADE WAKE

The general behavior of the mean and turbulent characteristics of a cascade wake is predicted in Chapter IV. A few of the unknown constants are needed to specify the quantitative behavior of the cascade wake. These constants are evaluated from the experimental data discussed in this chapter. The cascade used and the measurement technique is described in the previous chapter. The general trend in the experimental data is found to be consistant with the theoretical analysis. The experimental data on the mean and turbulence quantities is compared with other available data on a flat plate (Ref. 14), isolated airfoil (Ref. 48) and cascade of airfoils (Ref. 37). A general discussion on the behavior of the mean and turbulence quantities is presented. Empirical decay laws for the turbulence quantities are established. The region where the flow achieves self-preservation is determined. Expressions are also given for evaluating the mixing losses in the wake.

7.1 Mean Velocity Profile

As already stated, mean velocity profile measurements in the wake of a cascade were carried out for three angles of incidence (-6^o, 0^o, $+2^o$). The choice of angle of incidence was based on the fact that there was sudden rise in the coefficient of drag beyond -6^o and $+2^o$ angle of incidence for the cascade under investigation. Plots of mean velocity profile across the wake at different axial locations and at different angles of incidence are shown in Figures 7.1, 7.2, 7.3.

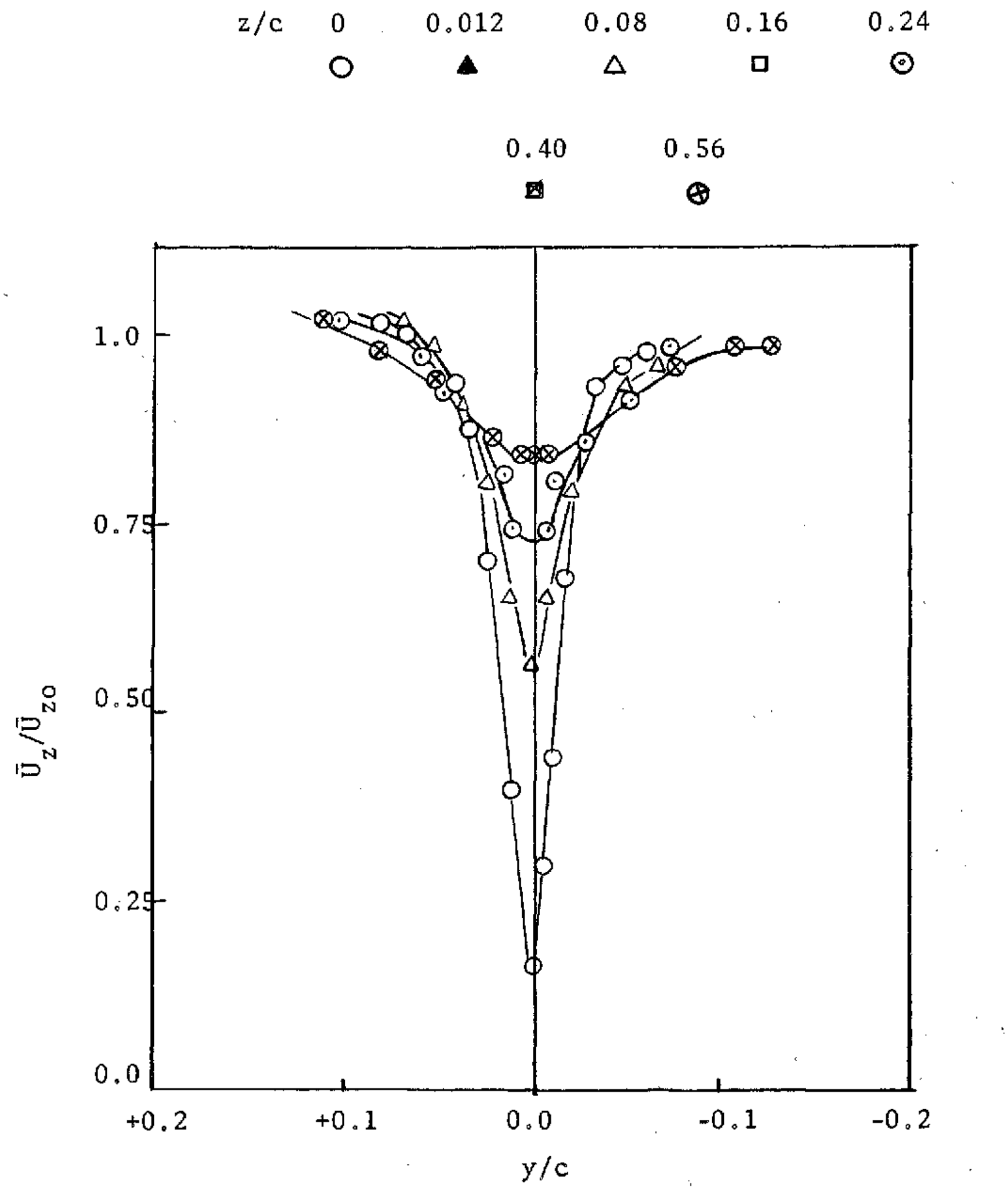

Figure 7.1 Mean Velocity Profile in a Turbulent Cascade Near Wake (incidence = 0°).

(See Figure 7.1 for Notation)

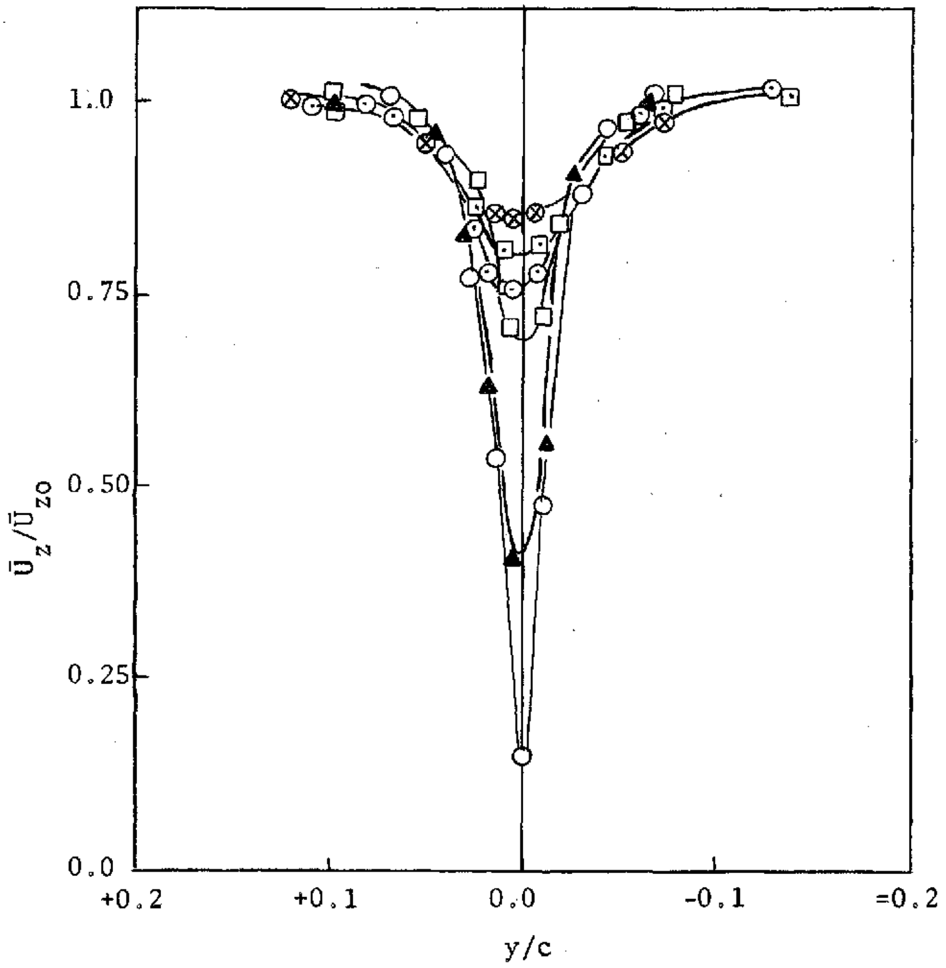

Figure 7.2 Mean Velocity Profile in a Turbulent Cascade Near Wake (incidence = +2°).

(See Figure 7.1 for Notation)

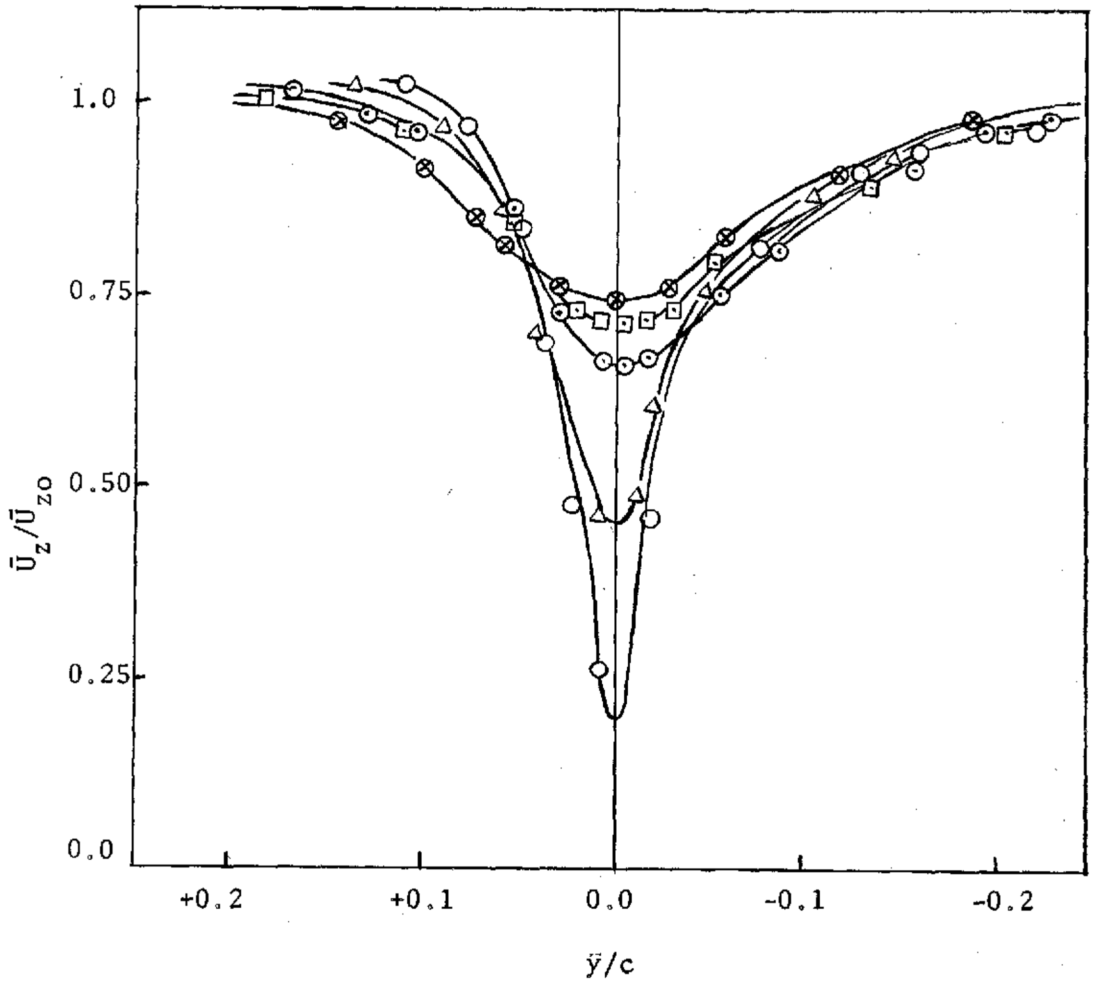

Figure 7.3 Mean Velocity Profile in a Turbulent Cascade Near Wake (incidence = -6°).

At the trailing edge ($z/c = 0.0$), the profiles exhibit characteristic features of boundary layer. The profiles are nearly symmetrical for zero angle of incidence, but show appreciable asymmetry at other angles of incidence (Figures 7.2 and 7.3). This asymmetry is preserved even at $z/c = 0.56$. The boundary layer thickness near the trailing edge is greater on the suction surface for angles of incidences, $i = 0$ and 2^{o}, and the trend is reversed for incidence at $i = -6^{o}$.

7.1.1 Self-Similarity

In Figures 7.4a and b, an attempt is made to reduce the mean velocity data to a single curve using scaling velocity as difference between the maximum and minimum velocity ($\bar{U}_d = \bar{U}_{zo} - \bar{U}_c$) and two different scaling lengths (ℓ_{os} and ℓ_{op}), which are distances on suction and pressure side of the wake centerline from the point of minimum velocity to a point where the velocity is $1/2\ (\bar{U}_{zo} - \bar{U}_c)$.

Figures 7.4a and b show the existence of similarity in the velocity profiles, when the velocity and the length scales described above are used. The profiles also become symmetrical about the wake centerline. The mean velocity can be represented by an expression of the type $(1 - \eta^{3/2})^2$, where $\eta = y/\ell_{os}$, or y/ℓ_{op} depending upon the suction or pressure side of the airfoil, respectively. The length scales ℓ_{os} and ℓ_{op} are different in the present case due to past history of the flow. However, in the case of the cylinder, flat plate or symmetrical airfoil at zero angle of incidence, $\ell_{os} = \ell_{op}$.

The ratio $\bar{U}_d\ \ell/\bar{U}_{ozt}\ c$ is found to be nearly constant at all axial locations and angles of incidence (Figure 7.5). This confirms the self-similarity assumption made in deriving Equation (4.12).

(See Figure 7.1 for Notation)

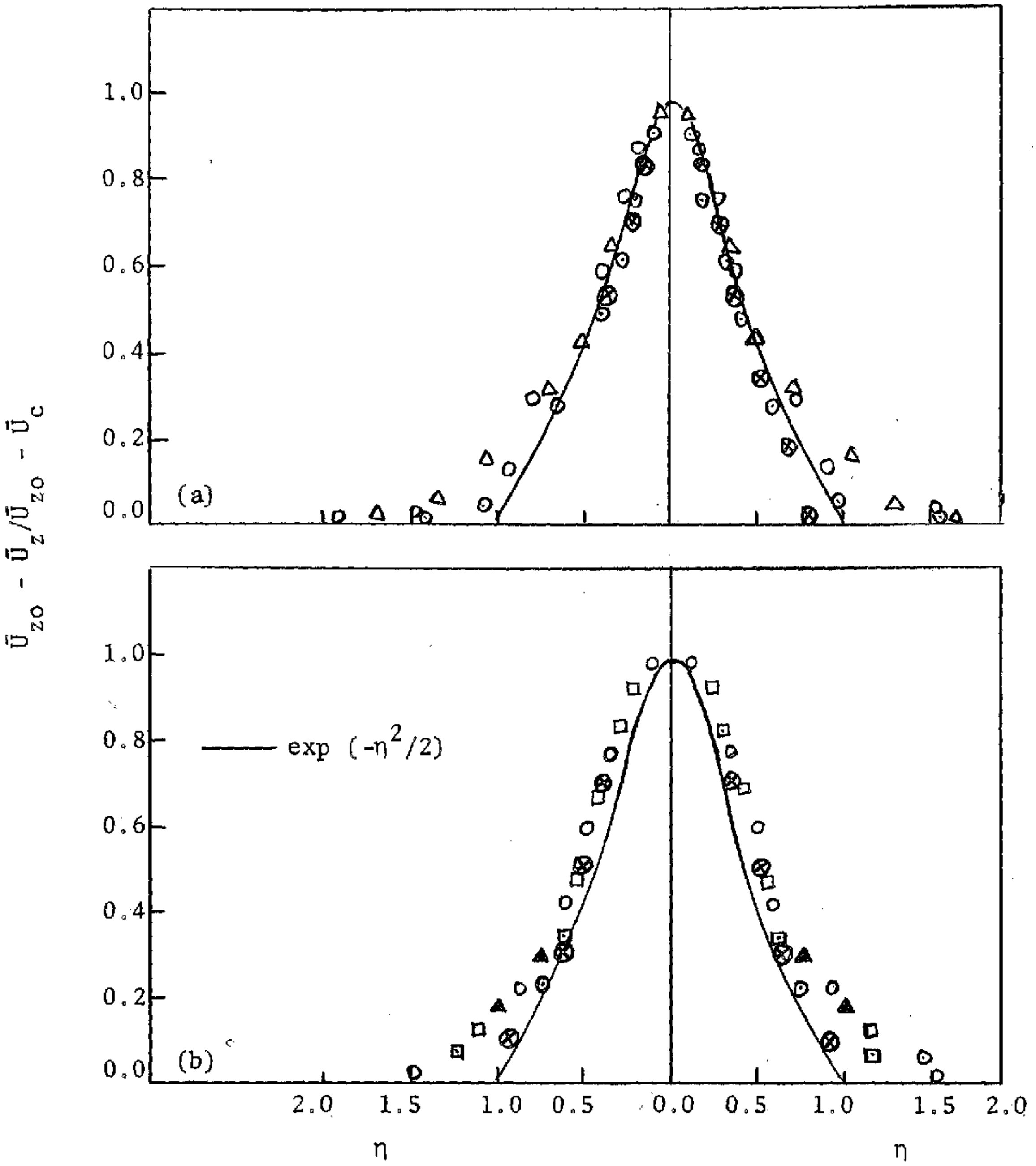

Figure 7.4 Similarity in Mean Velocity Profile of Turbulent Cascade Near Wake at Incidences: 0°, 2°.

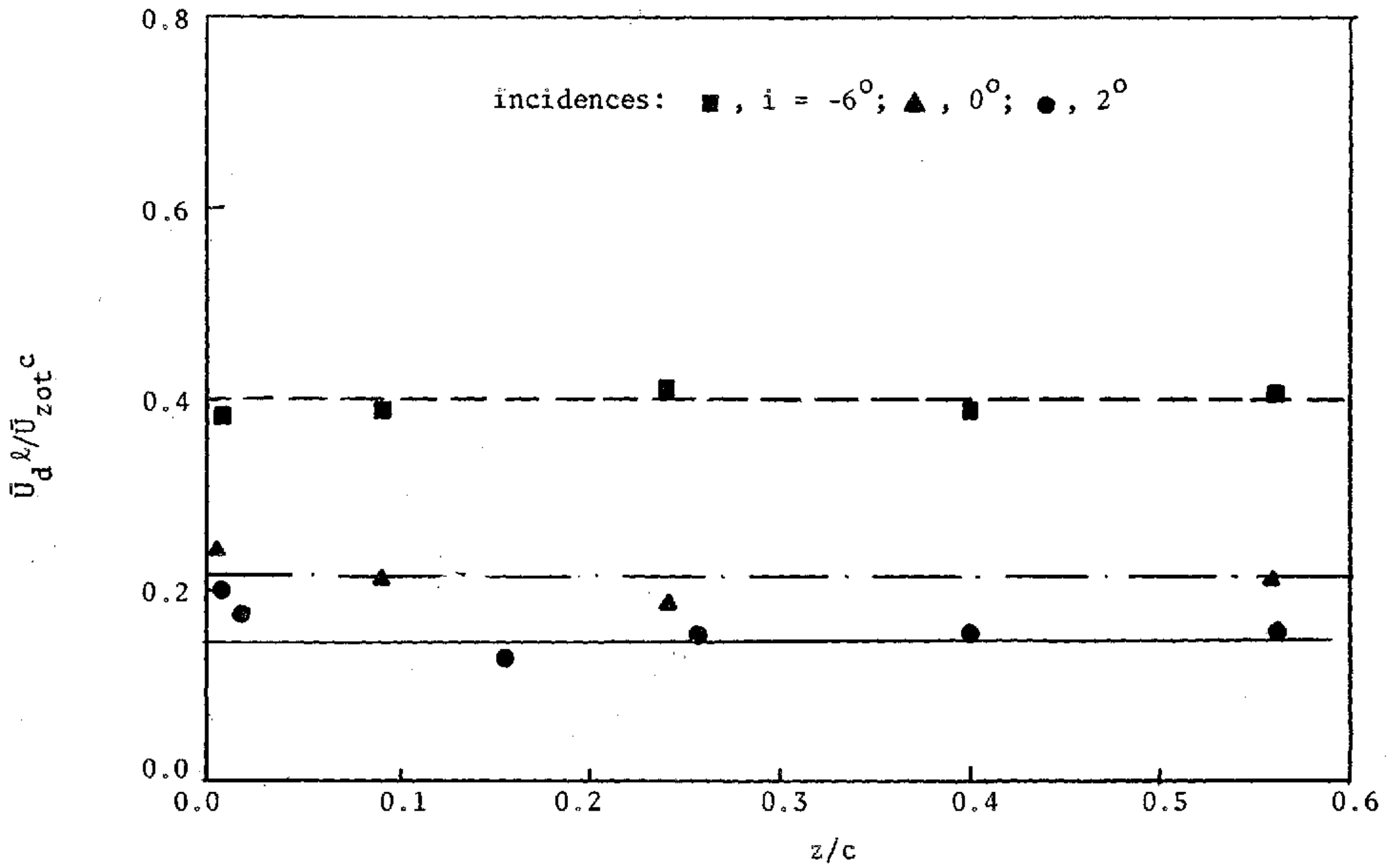

Figure 7.5 Variation of $\bar{U}_d \ell / \bar{U}_{zot}$ c with Downstream Distance.

7.1.2 Wake Centerline Velocity

In Figures 7.6 a and b are shown the variation of the wake centerline velocity with downstream distance at various angles of incidence. Leiblein and Roudebush's (37) data for a cascade, Chevray and Kovasznay's (14) data for a flat plate and Preston et al.'s (48) data for an isolated airfoil are shown compared with the authors's cascade data in Figure 7.6b.

It is clear from Figure 7.6a that the experimental results are in excellent agreement with the theoretical expression [Equation (4.19)]. Values of K and z_o/c are found to be 1.25 and 0.02, respectively. The values of coefficients of drag used for determining the constant k in the present investigation are determined experimentally. In the present investigation, (-m+1/2) changes from 0.39 to 0.487 for the change in angle of incidence from -6^o to $+2^o$. It is interesting to note that the value of k reported by Spence (58) for an isolated airfoil and the author's for a cascade of airfoils are about the same. While Spence's expression for $\bar{U}_c$ is valid for zero pressure gradient (m = 0), the author's [Equation (4.27)] for a cascade is more general.

A few important observations can be made from Figure (4.2) about the mean properties of cascade near wake.

(i) The wake centerline velocity is recovered to within 70 to 80 percent between trailing edge and half a chord length downstream.

(ii) Wake of a cascade decays slower than the wake of an isolated airfoil.

(iii) Wake decay of a cascade is dependent on the solidity and angle of incidence.

(See Figure 7.5 for Notation)

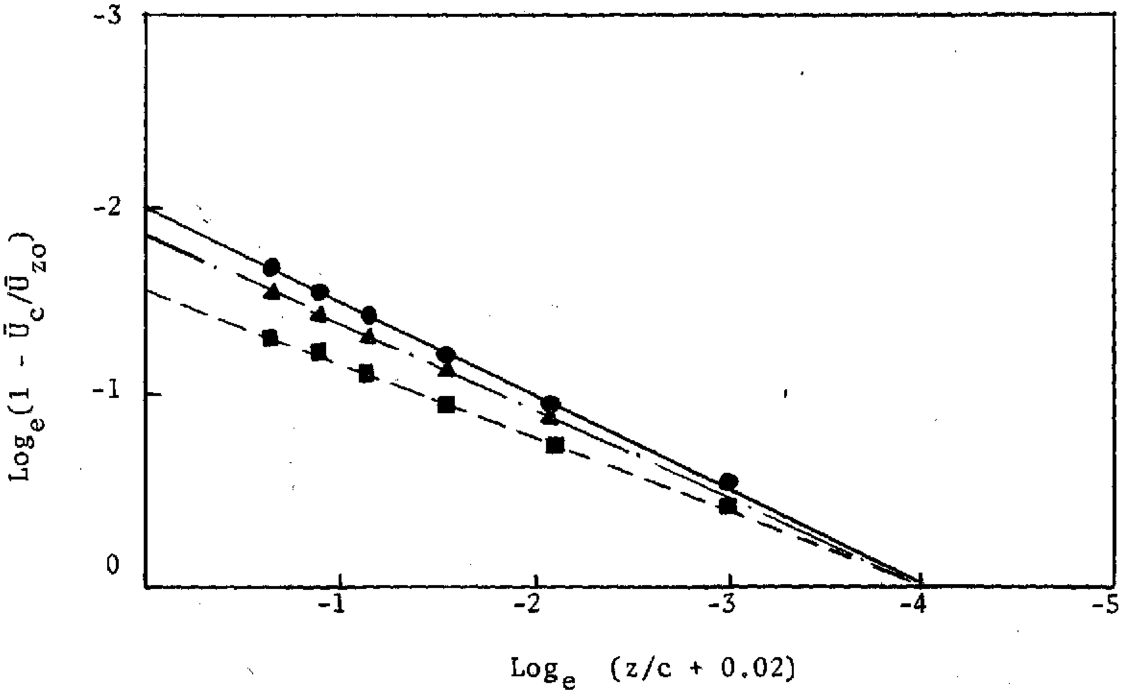

Figure 7.6(a) Logarithmic Variation of Wake Centerline Velocity with Downstream Distance at Incidences: 0°, 2°, -6°.

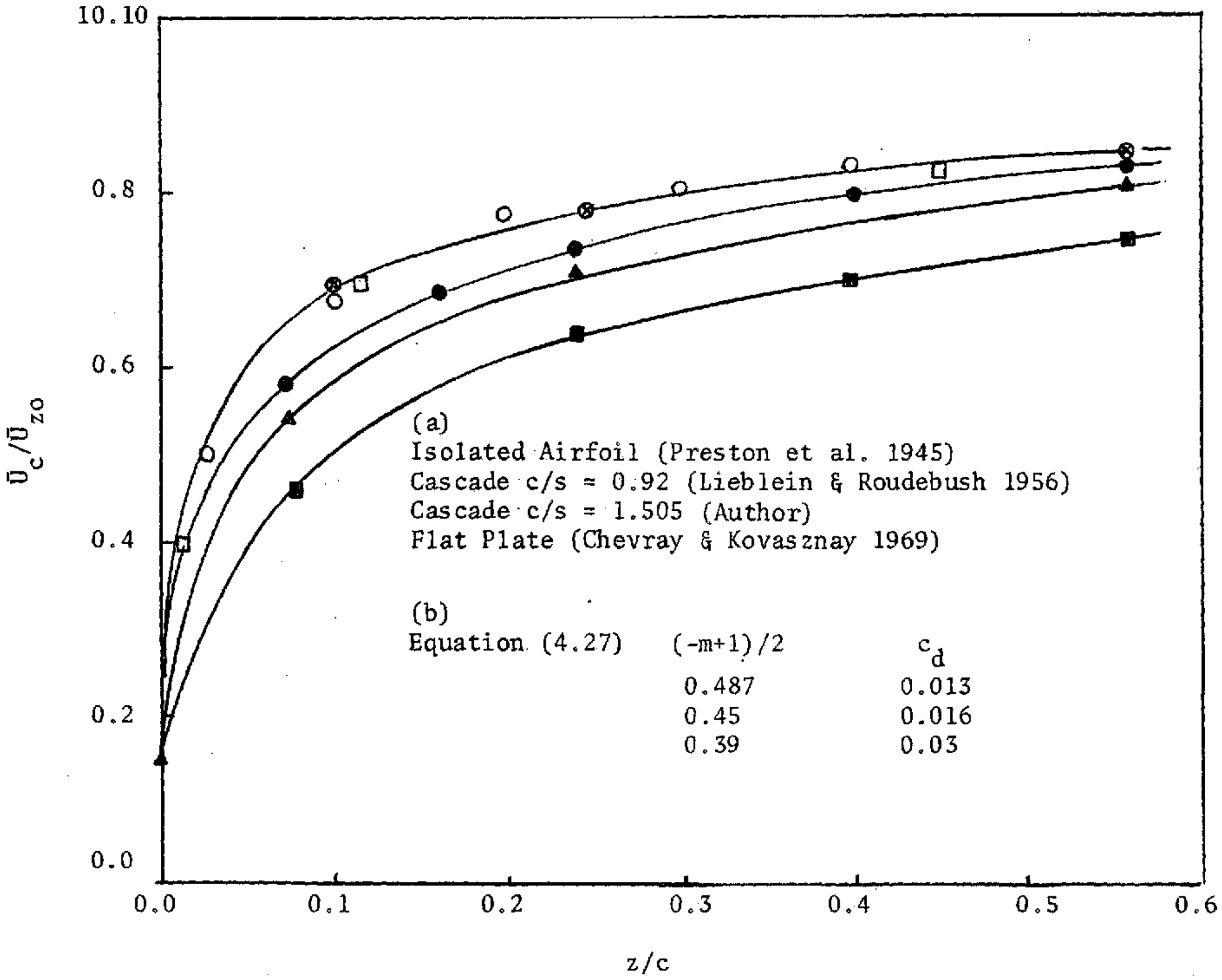

Figure 7.6(b) Variation of Wake Centerline Velocity with Downstream Distance for a Flat Plate, an Isolated Airfoil and a Cascade.

(iv) Wake decay of a cascade is dependent upon the geometry of the airfoil used. This is clear from the comparison of the wake of a flat plate and the symmetrical 12/40 Piercy airfoil (Ref. 48) at zero angle of incidence. These conclusions are in confirmity with the theoretical predictions (Chapter IV).

No measurements were carried out far downstream ($z/c > 1$). Therefore, it is difficult to comment on the accuracy of expression (4.28). However, Equation (4.28) for $c_d = 1$ reduces to the case of a far wake of equally spaced row of bars investigated by Olsson (44) who showed good agreement between experimental and theoretical results.

7.1.3 Wake Edge Velocity

The wake edge velocity measured in the cascade at various angles of incidence are shown plotted and compared with isolated airfoil data in Figure 7.7. It is evident that the wake edge velocity for a cascade first decreases very sharply near the trailing and then at a much slower rate. This trend is easily explained on the basis of the continuity equation

$$\bar{U}_{zot} (S_n - \delta^*) = \text{constant},$$

where $\bar{U}_{zot}$ is the wake edge velocity at the trailing edge and δ^* is the displacement thickness and S_n is defined in Figure 4.1. δ^* decreases rapidly near the trailing edge and at a slower rate further downstream. The wake edge velocity for an isolated airfoil increases, while that for a cascade decreases downstream (Figure 7.7).

The edge velocity can be expressed as (Figure 7.7),

$$\bar{U}_{zo} \sim 1/z^m \quad ,$$

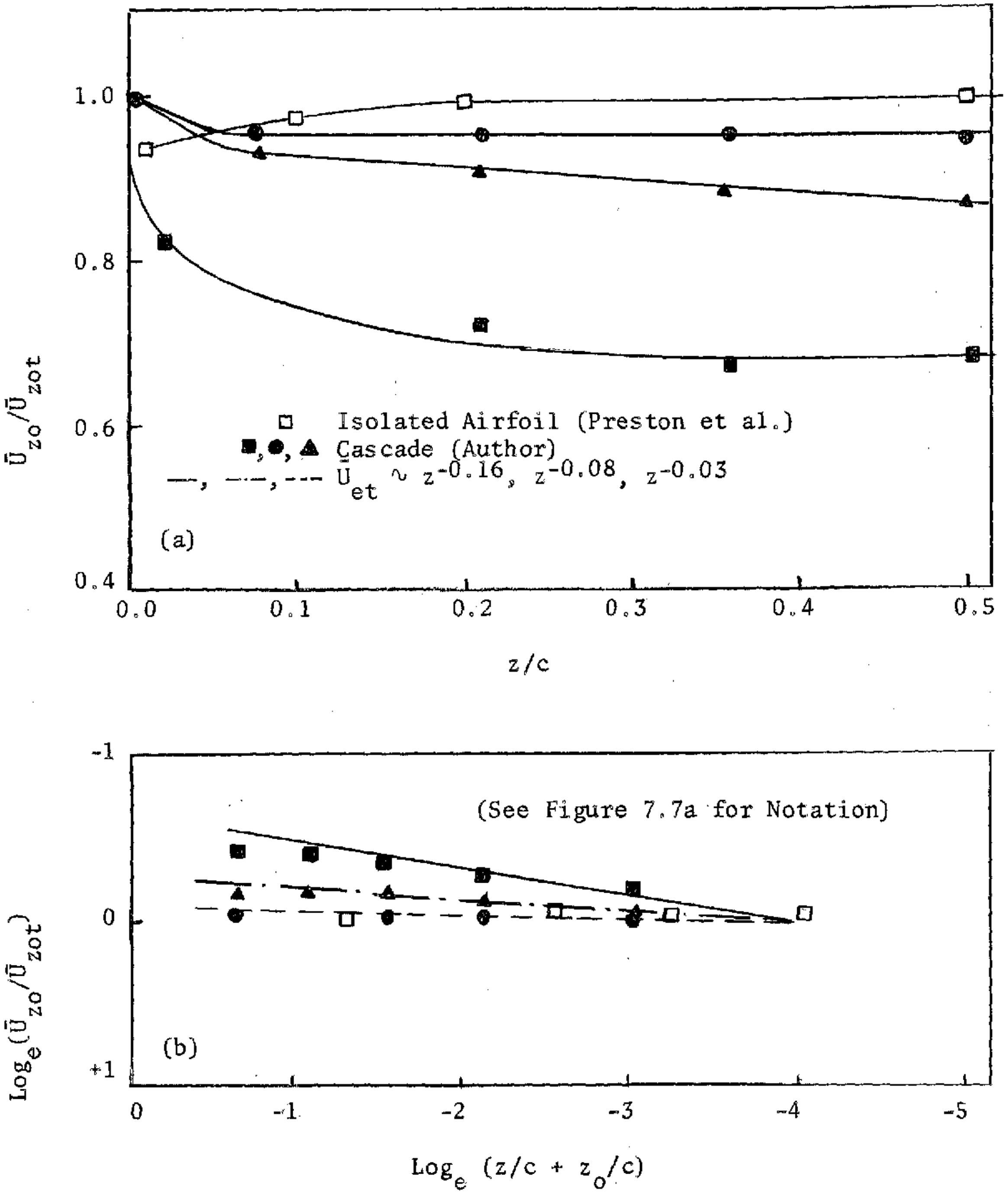

Figure 7.7 Variation of Wake Edge Velocity with Downstream Distance at Incidences; 0°, 2°, -6°.

where the value of m is found to be - 0.028 for an isolated airfoil and 0.16, 0.08 and 0.03 for cascade at angles of incidence -6°, 0° and 2°, respectively. Based on this, the exponent of $(z/c + z_o/c)$ in Equation (4.27) should be 0.42, 0.46, and 0.485, respectively, for the cascade of blades at -6°, 0°, and 2°, respectively. Values of this exponent derived directly from the wake measurements (Figure 7.6) are found to be 0.39, 0.46, and 0.487, respectively. Thus, the agreement between the theoretically predicted decay rate [Equation (4.27)] and the measured rate is good. This clearly points out the effect of external pressure gradient ($m \neq 0$) and its effect on wake decay.

7.1.4 Wake Width

A logrithmic plot of the variation of the wake width at various distances downstream is shown in Figure 7.8. It is interesting to note that most of the wake width data follows the relationship

$$\frac{b - b_o}{c c_d^{1/2}} = 1.35 \; (z/c + z_o/c)^{0.58} \tag{7.1}$$

where b = wake width, b_o its value at the trailing edge. The values of c_d used in Figure 7.8 are the measured values. The points up to z/c = 0.35 seem to be well represented by this equation and the exponent in Equation (7.1) is nearly 0.5 beyond this point.

Theoretically, the exponent in Equation (7.1) should be 0.58, 0.54, and 0.515 [Equation (4.18)] with m = 0.16, 0.08, and 0.03 for -6°, 0°, and 2°, respectively. The discrepancy between the theory and the experiment may be due to the difficulty in assessing the value of b from the measurements. Nevertheless, it is evident that the widely used representation of wake width ($b \sim z^{1/2}$) is not accurate, especially for a cascade wake with pressure gradient in the external flow.

(See Figure 7.5 for Notation)

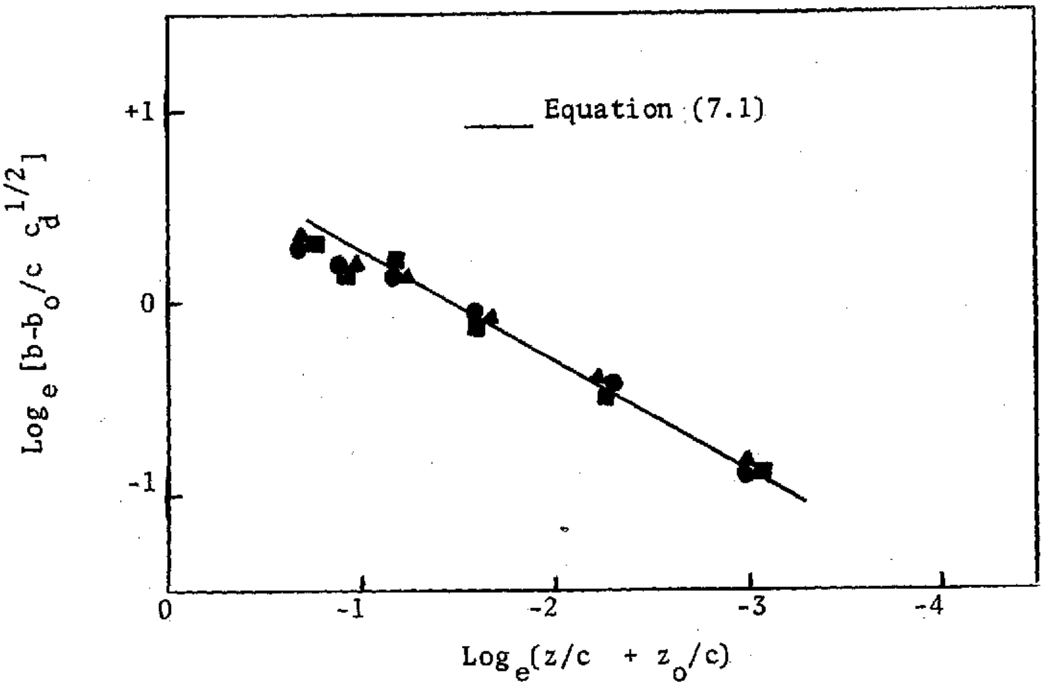

Figure 7.8 Logarithmic Variation of Wake Edge Velocity with Downstream Distance at Incidences; 0°, 2°, -6°.

7.1.5 Momentum Thickness (θ^*) and Shape Factor (H)

A plot of the variation of the momentum thickness θ^* is given by

$$\theta^* = \int \frac{\bar{U}}{\bar{U}_{zo}} (1 - \frac{\bar{U}_z}{\bar{U}_{zo}}) \, dy \quad ,$$

and the shape factor H (where $H = \delta^*/\theta$) with downstream distance from the trailing edge is given in Figure 7.9. The magnitude of the momentum thickness first increases and then becomes almost constant while the shape factor decreases first and then becomes nearly constant. Therefore, the maximum of mixing losses takes place very close to the trailing edge.

The characteristic behavior of θ^* is explained on the basis of the well-known Von Karman's momentum integral equation:

$$\frac{d\theta^*}{dz} + (H + 2) \frac{\theta^*}{\bar{U}_{zo}} \frac{d\bar{U}_{zo}}{dz} = \frac{\tau_o}{\rho \bar{U}_{zo}^2} \quad . \tag{7.2}$$

In a wake, skin friction is zero; therefore, Equation (7.2) reduces to the following form:

$$\frac{d\theta^*}{dz} + (H + 2) \frac{\theta^*}{\bar{U}_{zo}} \frac{\bar{U}_{zo}}{dz} = 0 \tag{7.3}$$

Equation (7.3) shows that increase or decrease of θ^* depends upon the variation of $\bar{U}_{zo}$. If $\bar{U}_{zo}$ increases, then θ^* decreases (isolated); if $\bar{U}_{zo}$ decreases, then θ^* increases (cascade). This is evident from Figure 7.9. The variation of shape factor with downstream distance from the trailing edge of an isolated airfoil is given by Spence (58):

$$(1 - \frac{1}{H}) = (1 - \frac{1}{H_t}) \; (40 \; z/c + 1)^{-1/2} \quad , \tag{7.4}$$

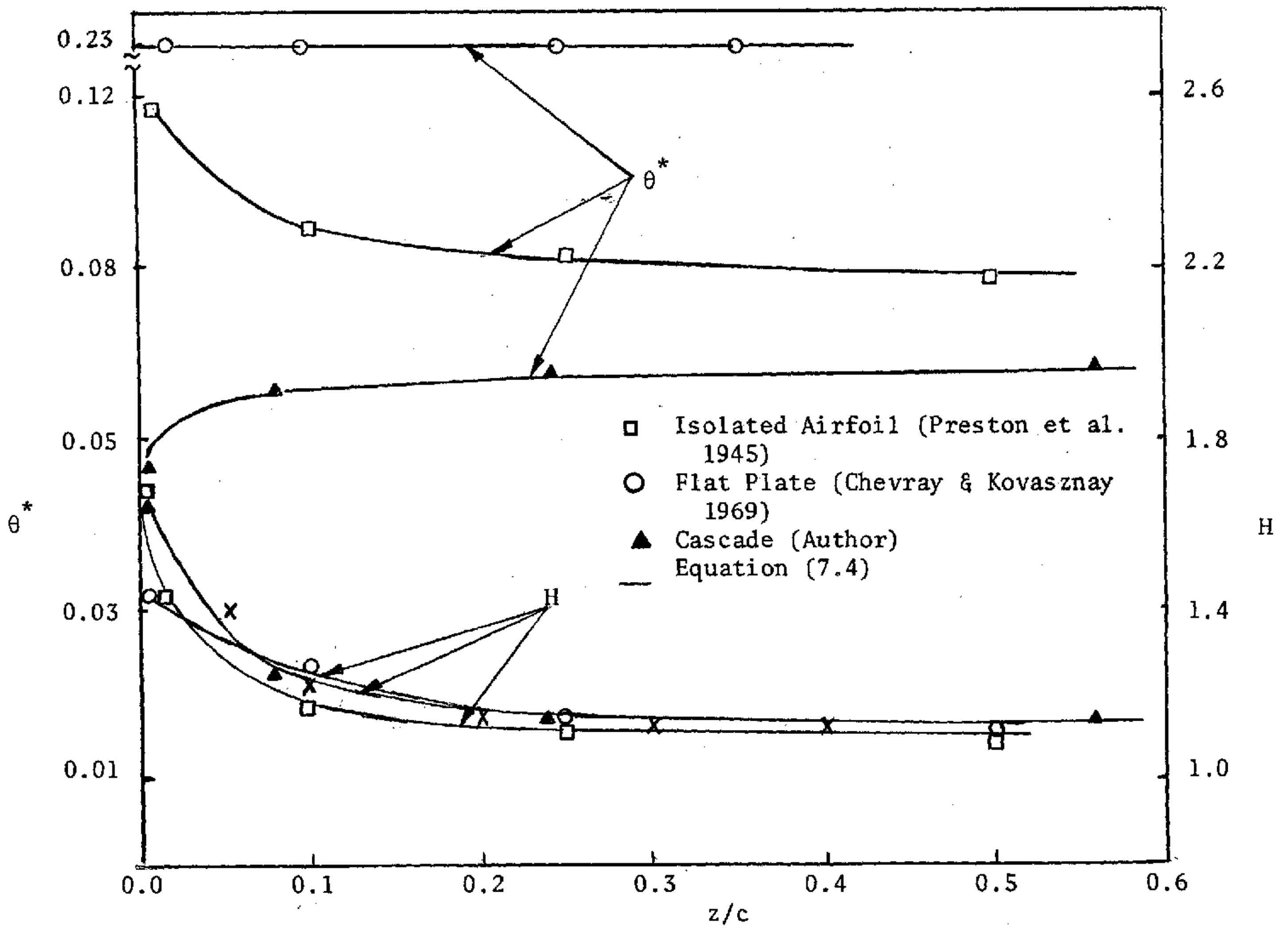

Figure 7.9 Variation of Shape Factor (H) and Momentum Thickness (θ^*) with Downstream Distance (incidence = 0^o)

where H_t is shape factor at the trailing edge. The same expression accurately predicts the variation of H in a cascade near wake (Figure 7.9).

Since H can be predicted and $\bar{U}_{zo}$ is known, θ* for the cascade can be predicted from Equation (7.3).

7.2 Turbulence Quantities

7.2.1 Turbulence Intensity

In Figures 7.10 and 7.11 are shown the plot of turbulence intensities in streamwise [$\sqrt{\overline{U'^2_z}}$] and transverse [$\sqrt{\overline{U'^2_y}}$] directions in the cascade wake at different axial locations. Initially, the curves are asymmetric about the wake centerline and the asymmetry is retained in the region of investigation ($0 < z/c < 0.72$). The asymmetry about the wake centerline is due to the past history of the flow. However, far downstream, the asymmetry may disappear because the flow tries to forget its past history. The maximum of turbulence intensity in the present case occurs almost at the wake centerline. The reasons for this are as follows. Exactly at the wake centerline Reynolds stress is either zero or has a very small value. The anisotropy introduced into the flow due to the presence of the body is an additional source of turbulence intensity at the wake centerline besides being the transport of turbulence energy by advection. The conversion of the energy of mean flow to turbulent energy takes place through the process of diffusion along the velocity gradients. Transport cannot bring kinetic energy from the center of the wake because gradients of turbulence intensities are negligible there. Therefore, the deposit of energy due to advection and turbulence

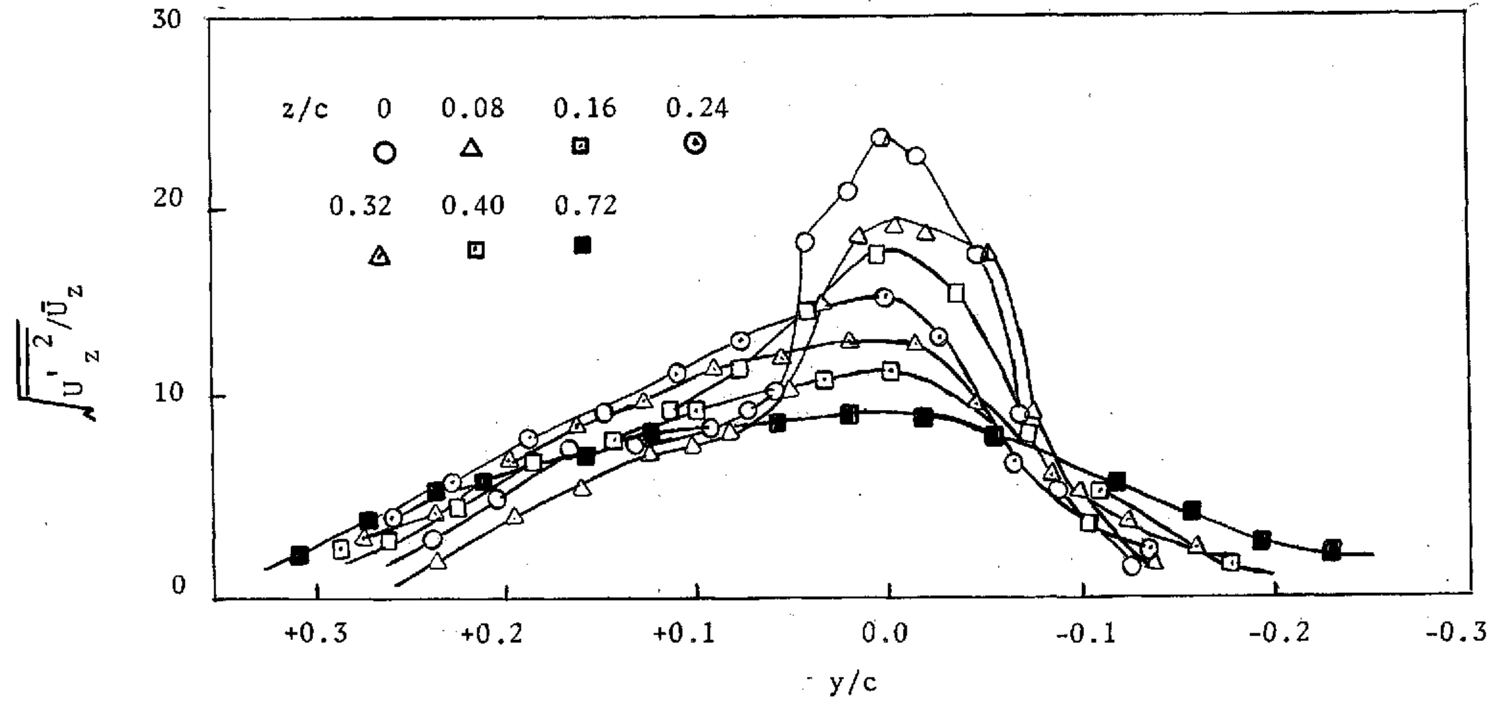

Figure 7.10 Turbulence Intensity of Streamwise Component of Velocity Fluctuations in a Wake Close Behind a Cascade.

(See Figure 7.10 for Notation)

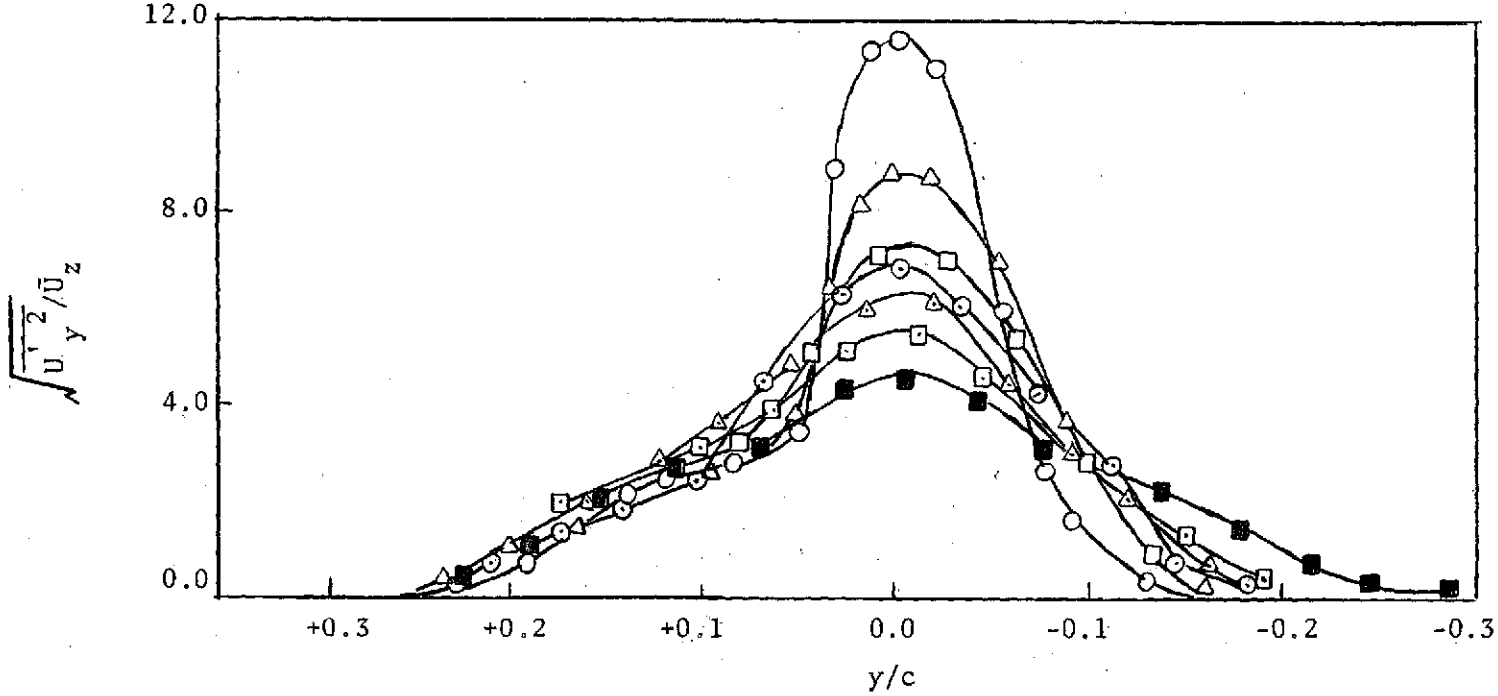

Figure 7.11 Turbulence Intensity of Normal Component of Velocity Fluctuations in a Wake Close Behind a Cascade.

production are completely dissipated there. At the same time, the region of maximum shear close to the wake centerline will behave in a different way. Due to the existence of large gradients, most of the energy transported to the outer part of the wake originates here, while the remaining dissipates. Hence, it is not unlikely that a maximum of turbulence intensity will occur at the wake centerline in the present situation.

However, far downstream of the cascade the maximum of turbulence intensity will not usually occur at the wake centerline, because the production due to anisotropy is negligibly small at the wake centerline and the turbulence production peaks (in the region of maximum shear) will be away from the centerline. Therefore, there will be a gradient transport of energy to the outer part of the wake, and hence, dissipation will be considerably less than in the case of the near wake.

The distance downstream where the peak of turbulence intensity will cease to occur at the wake centerline depends upon the maximum thickness-to-chord-length ratio in cascade of slender bodies. For a very thin flat plate, the peak of turbulence intensity may not occur at the wake centerline even close to the trailing edge of the plate (Ref. 14).

The decay rate of the maximum of T_{uz} $[\sqrt{\overline{U_z'^2}}/\overline{U}_z]$ and $T_{uy}[\sqrt{\overline{U_y'^2}}/\overline{U}_z]$ with distance downstream from the trailing edge is shown in Figure 7.12. As is evident from Figure 7.12 $(T_{uz})_{max}$ decays faster than $(T_{uy})_{max}$ in the region of investigation $(0 < z/c < 0.72)$. This confirms the earlier conclusion, based on theoretical considerations, made in Section (4.3.1) [Equation (4.30)]. The variation of $(T_{uz})_{max}$ and $(T_{uy})_{max}$ in a cascade can be represented by the following expressions:

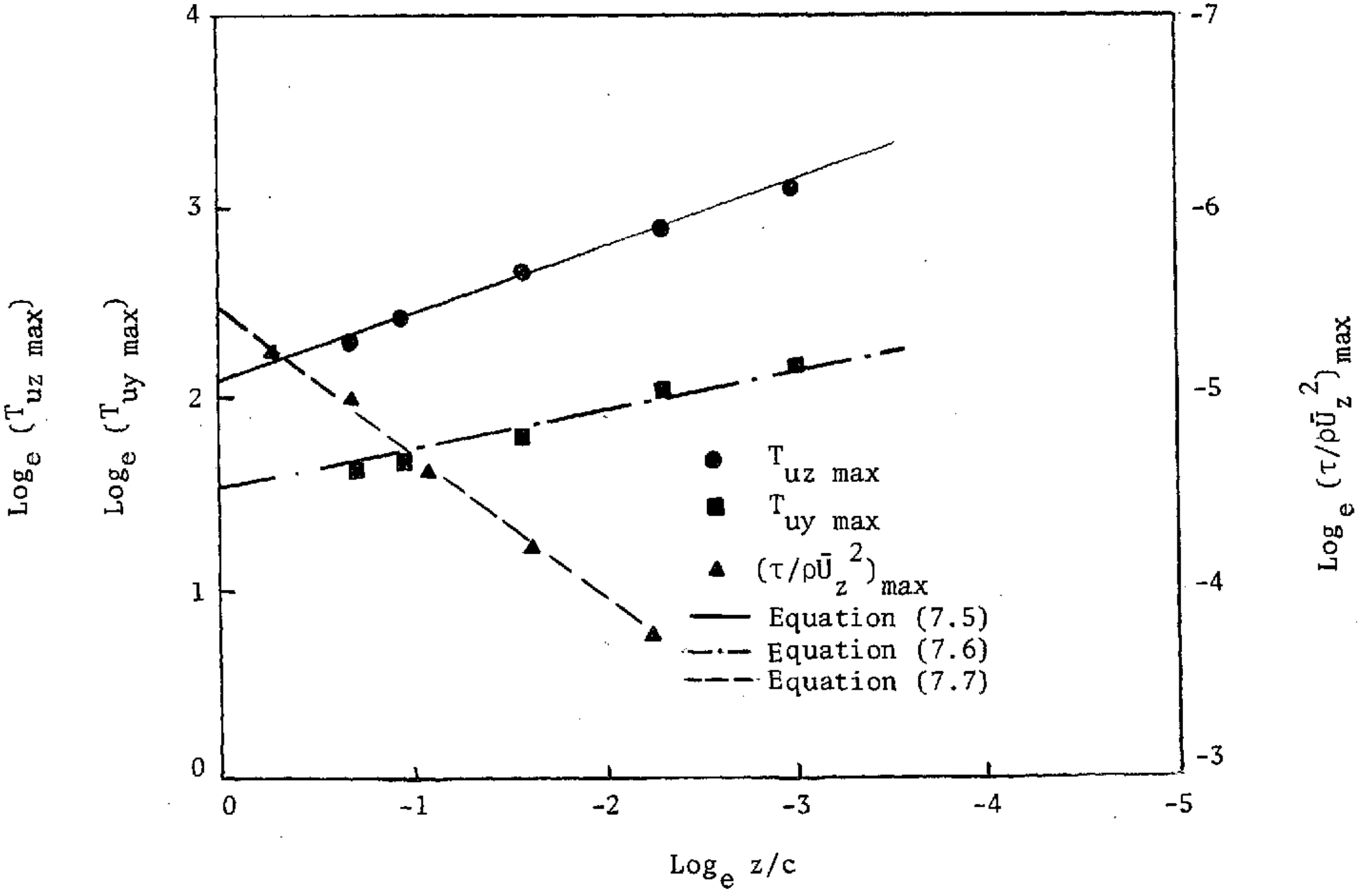

Figure 7.12 Decay of Maximum Turbulence Intensities and Reynolds Stress in a Cascade Wake with Downstream Distance.

$$T_{uz}\% = 8\ (z/c + z_o'/c)^{-\ 0.35} \tag{7.5}$$

and

$$T_{uy}\% = 4.6\ (z/c + z_o'/c)^{-\ 0.20} \tag{7.6}$$

It should be remarked here that all intensities are normalized with respect to local mean velocity. The value of the virtual origin $[z_o'/c]$ in this case is found to be 0.05.

$(T_{uz})_{max}$ is found to be roughly twice as large as $(T_{uy})_{max}$ near the trailing edge as expected due to wall constraints. Farther downstream they tend to become equal (Figures 7.10, 7.11, and 7.12). The quantitative nature of behavior of turbulence intensities at the wake centerline is consistent with Equation (4.30). Although the turbulence intensity T_{ux} was not measured, but it is predicted that T_{ux} will be close to T_{uy} than to T_{uz} in magnitude. But away from the trailing edge ($z/c > 0.1$) it will take an intermediate value between T_{uz} and T_{uy}.

It is interesting to note that $(T_{uz})_{max}$ and $(T_{uy})_{max}$ in the case of a flat plate (Ref. 14), also decay with the same power law as cascade, Equations (7.5) and (7.6) (see Figure 7.13).

7.2.2 Reynolds Stress

Figure 7.14 shows the distribution of Reynolds stress in a wake behind the cascade at different axial locations. It should be noted here that Reynolds stress changes sign abruptly at the wake centerline and the maximum of Reynolds stress on either side of the wake centerline need not necessarily be the same in magnitude and are in fact found to be different near the trailing edge (Figure 7.14) of the cascade of cambered airfoils investigated here. However, away from the

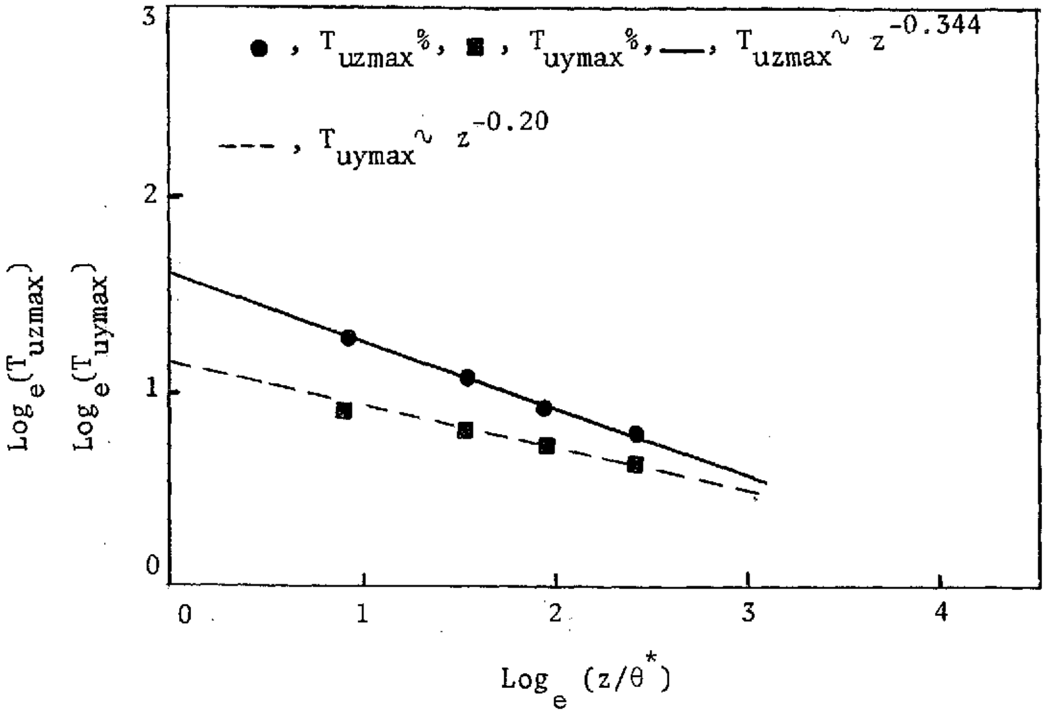

Figure 7.13 Decay of Maximum Turbulence Intensities for a Flat Plate (Data of Ref. 14).

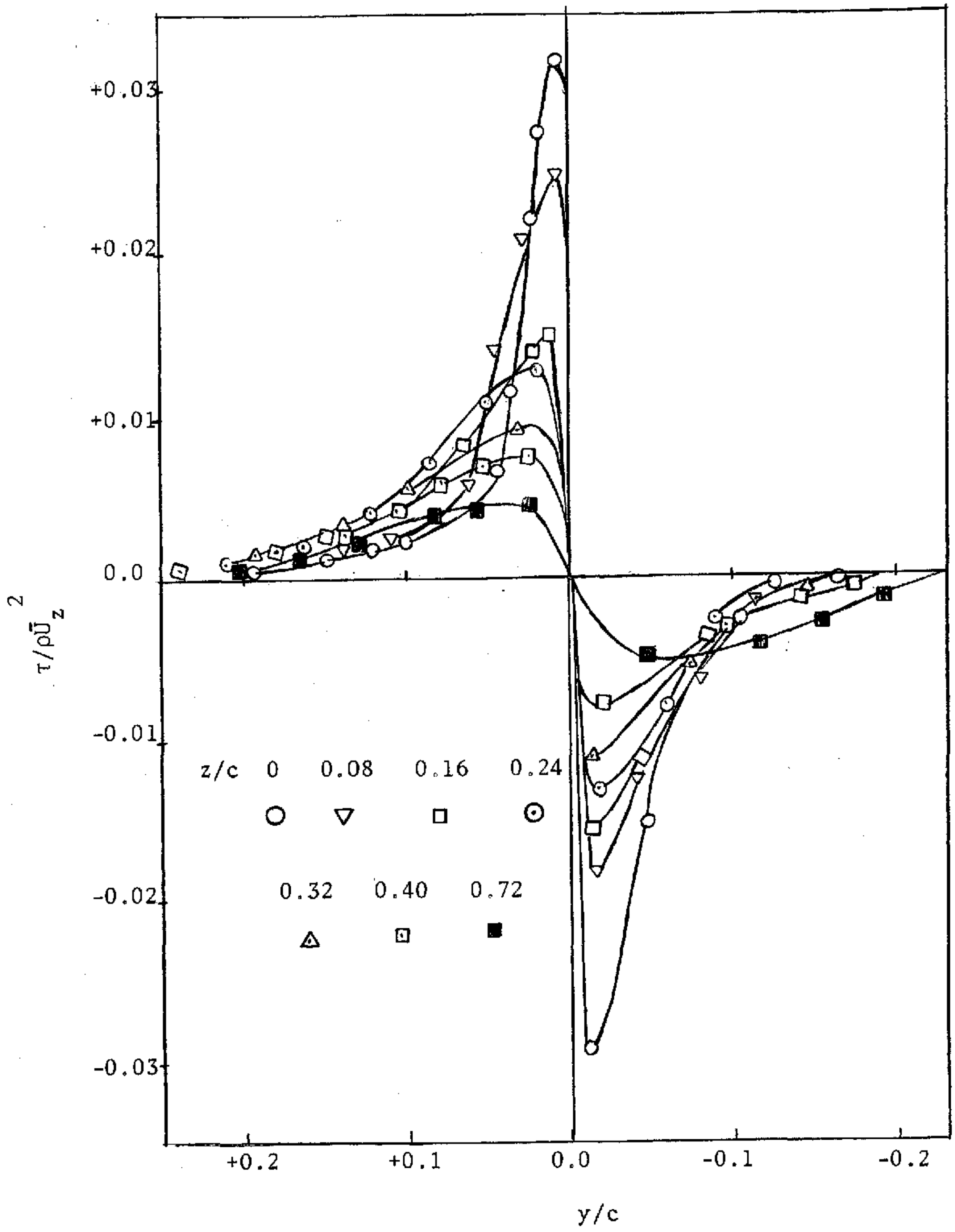

Figure 7.14 Distribution of Shear Stress in a Wake Close Behind a Cascade.

trailing edge, this difference disappears. The maximum value of Reynolds stress decreases rapidly along the streamwise direction up to a distance of z/c = 0.35 (Figure 7.12). But beyond z/c > 0.35, the rate of decrease is small. Variation of $[\tau/\rho\bar{U}_z^2]_{max}$ with distance downstream is given by the following expression (Figure 7.12):

$$[\frac{\tau}{\rho\bar{U}_z^2}]_{max} = 0.005\,[z/c + 0.05\,]^{-0.72}. \tag{7.7}$$

Near the wake center, the shear stress varies linearly across the wake. A very sound qualitative explanation for such behavior has been given by Townsend (62) for a far wake. The same reasoning applies also to a near wake. It should be observed that $(\partial\tau/\partial y)_{y=0}$ is decreasing with streamwise direction and the region of maximum shear is displaced away from the wake centerline with streamwise distance downstream.

In the present investigation, it is found that the point where $\partial\bar{U}_z/\partial y = 0$ (wake centerline) need not necessarily be the same where Reynolds stress is zero. This clearly indicates that mixing length hypothesis is not valid for predicting the mean and turbulence quantities in such a region. The variation of $\overline{U'_z U'_y}/\overline{U'^2_z}$ with distance downstream from the trailing edge is shown in Figure 7.15 and is found to be constant (0.515) near half the wake width. The constant value is found to be little higher than in flows with uniform distortion of homogeneous turbulence (0.4) or the theoretical value (0.354) predicted in Section (4.3.2).

7.2.3 Self-Preservation

An attempt was made to correct turbulence intensities and Reynolds stress data using the same velocity and length scales as that used for

(See Figure 7.14 for Notation)

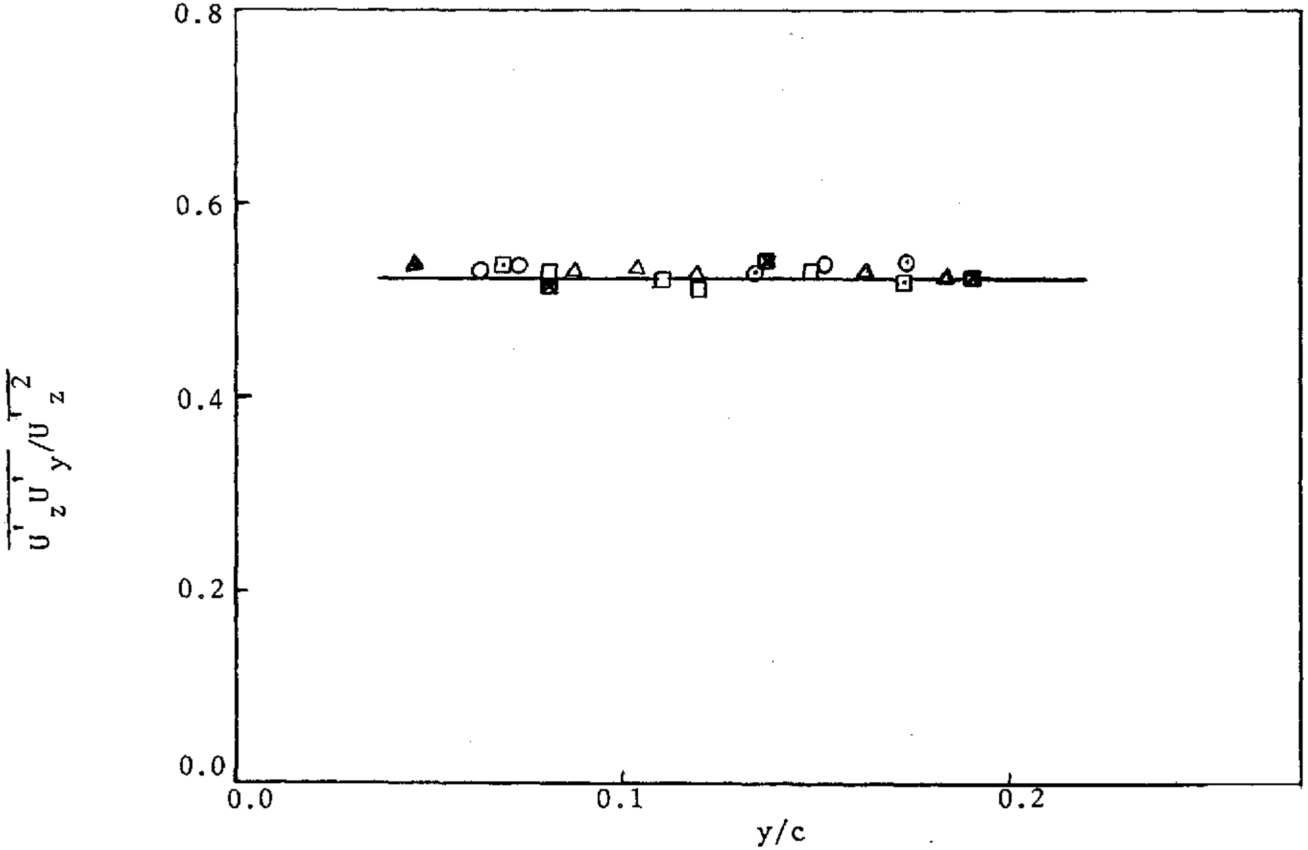

Figure 7.15 Ratio of Shear Stress to Turbulence Intensity Near Half the Wake Width in a Cascade Wake.

mean velocity. The data could not be reduced to a single curve as in the case of mean velocity profile. This shows that the flow is not completely self-preserved. An explanation for such behavior can be given by considering the turbulent energy equation. In a two-dimensional mean motion, the two energy production terms can be written as

$$- \overline{U'_z U'_y} \frac{\partial \bar{U}_z}{\partial y} \quad \text{and} \quad (\overline{U'^2_z} - \overline{U'^2_y}) \frac{\partial \bar{U}_z}{\partial z} \quad . \tag{7.8}$$

The first of these terms is usually ignored in homogeneous distorted turbulence, while the second in isotropic far wake. Therefore, the term introducing nonself-preservation in the flow is the second term. Since at the trailing edge of the cascade there is production of turbulence intensity and the flow is anisotropic, the second term is of comparable magnitude to the first term. The production of turbulent energy differs for various bodies and depends upon the shape of the body. In the case of bluff bodies the second term is of much higher order (3 to 4 times) compared to streamlined bodies or flat plate. This is the reason why in the case of streamlined bodies the self-preservation is attained much earlier than in the case of bluff bodies. Reynolds (53) deduced a criterion for self-preservation based on the above two energy production terms,

$$P = \left[\frac{-\overline{U'_z U'_y} \; \partial \bar{U}_z/\partial y}{(\overline{U'^2_z} - \overline{U'^2_y}) \partial \bar{U}_z/\partial z} \right]_{y = \ell} , \tag{7.9}$$

where ℓ is half the wake width. If $P > 1$, (i.e., shear dominated flows) and equal to 3 the flow tends to be nearly self-preserved. But for complete self-preservation, P has to have a much larger value (≥ 10).

If $P < 1$, the flow is not self-preserved. Variation of P downstream in the streamwise direction of the cascade is shown in Figure 7.16. This shows that, from $z/c \simeq 0.24$ onward the wake is nearly self-preserved.

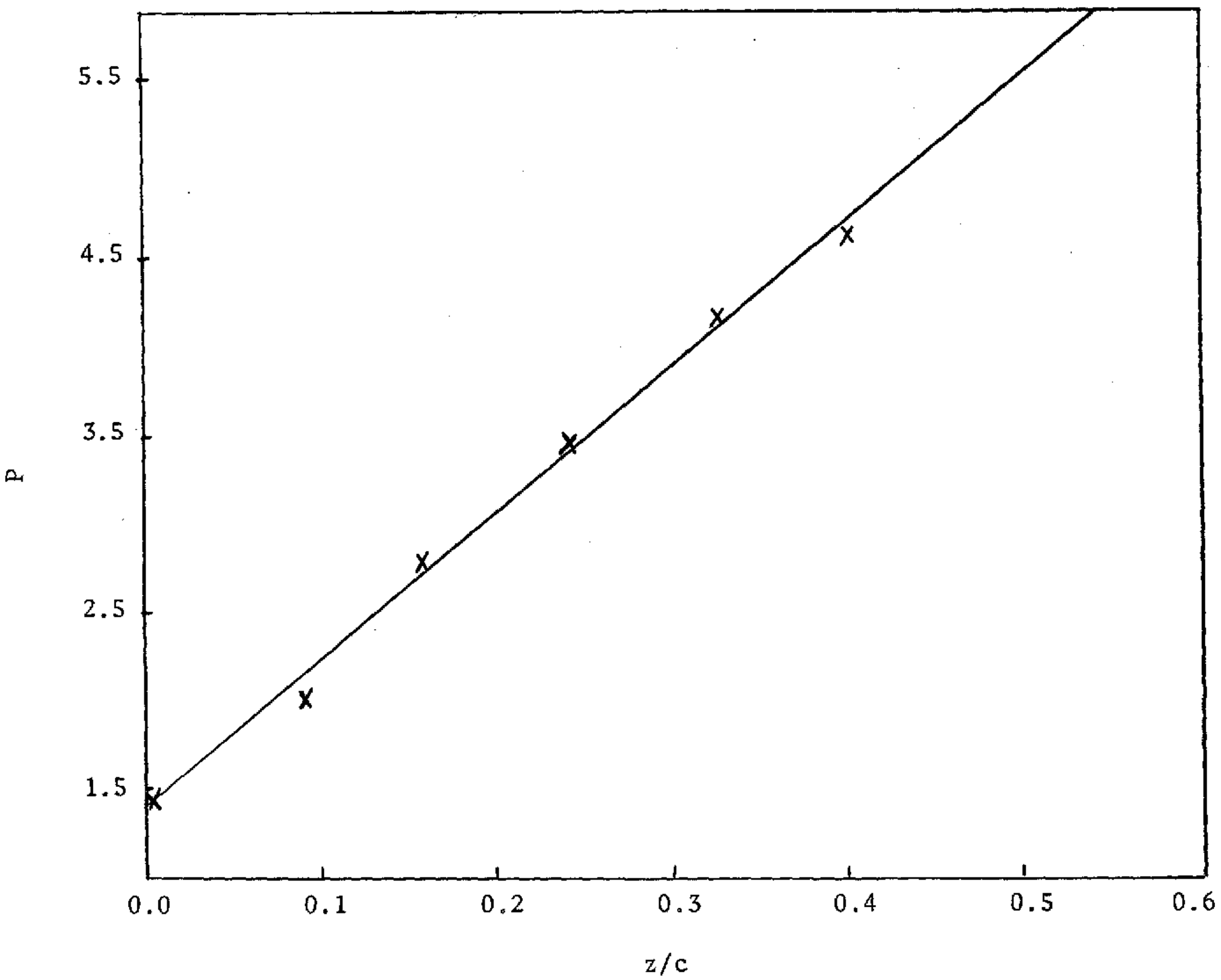

Figure 7.16 Variation of P with Downstream Distance in a Cascade Wake.

CHAPTER VIII

EXPERIMENTAL RESULTS AND COMPARISON WITH PREDICTIONS FOR ROTOR WAKE

The general behavior of the mean flow characteristics of a rotor wake was predicted in Chapter V. A few of the unknown constants are needed to specify the quantitative behavior of the rotor wake. These constants are evaluated from the experimental data discussed in this chapter. The general trend in the experimental data is found to be consistent with the theoretical analysis. The data on the mean and turbulence quantities is compared with the data of an isolated airfoil (Ref. 48) and a cascade of airfoils (Ref. 49). A general discussion on behavior of the mean and turbulence quantities is presented. Empirical decay laws are established for the turbulence quantities.

The measurements with a single sensor hot-wire probe, static pressure probe and three-sensor hot-wire probe will be presented and discussed.

8.1 Overall Disturbance Level

Plots of overall disturbance level $T_D = V^2/\bar{V}$, $\bar{V}$ = circumferential average, of downstream distance from the trailing edge and speed of rotation of the machine are shown in Figure 8.1. Measurement of the overall disturbance level was undertaken due to the following reasons:

(i) It will aid in the selection of the turbulence instrumentation for measurement with a three-sensor hot-wire probe.

(ii) It provides information on the gross characteristics of wake turbulence downstream of a rotor.

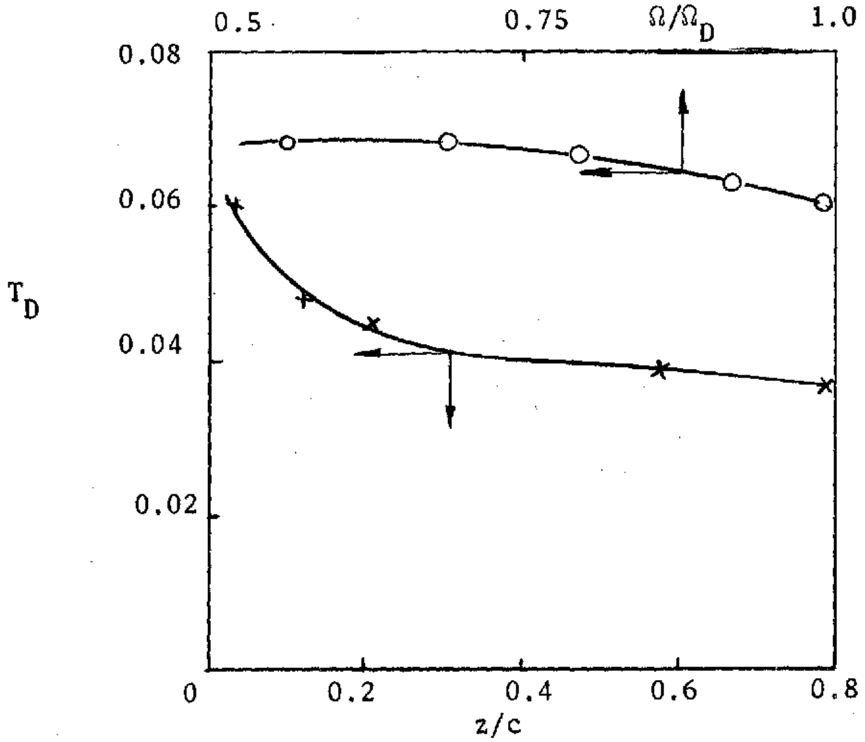

Figure 8.1 Variation of Total Disturbance Level with Distance Downstream and the Speed of Rotation.

(iii) In addition, it provides an easy means of studying the effect of rotation on overall disturbance level at the design operating condition.

The overall disturbance level was measured with a single-sensor hot-wire probe. Two sets of experiments were carried out. In the first set of experiments, the probe was traversed downstream of the trailing edge. However, the radial position of the probe at the downstream stations was kept the same ($r/r_t = 0.72$). In the second set of experiments, the position of the probe was not changed but the speed of the rotor was varied.

As is evident from Figure 8.1, there is a rapid drop in the overall disturbance level close to the blade trailing edge. Farther downstream, the drop in overall disturbance level is considerably smaller. The effect of the variation in speed of rotation on the overall disturbance level is also shown in Figure 8.1. It should be noted that the flow coefficient was kept the same while the speed of rotation was changed. This is the main reason why the effect of rotation is insignificant. It should be pointed out here that the overall disturbance level changes with flow coefficient (Ref. 23, 24). Since the rotor in this case was always operating at design condition, very little change in overall disturbance is observed.

8.2 Static Pressure Distribution

A static pressure probe, manufactured by The Flow Corporation, was used to measure the static pressure at the exit of the rotor. The probe is 3.2 mm in diameter and has two separation rings to assure stability of the sphere's wake region. It is insensitive to yaw and pitch angles in a wide range of angles of variation ($\pm$ 40°). Calibration of the probe is described in Chapter VI.

The radial distribution of static pressure coefficient (ψ_s) at various axial stations is shown in Figure 8.2. It is evident from this figure that the variation of ψ_s in the axial direction is small. The measured gradients in static pressure ($\partial p/\partial r$) is in close agreement with the predictions based on the equation

$$\frac{1}{\rho}\ \frac{\partial p}{\partial r} = 2\Omega\ \bar{U}_{so}\ \sin\lambda\ + \Omega^2 r\ . \tag{8.1}$$

This confirms the validity of the assumptions made in the theoretical analysis.

8.3 Mean Velocity Profile

As indicated earlier, mean velocity profile measurements in the wake of a rotor were carried out at eight radial stations and five axial stations. However, only one radial station is considered in this discussion. The radial station selected is r/r_t = 0.58. Plots of mean streamwise and radial velocities are shown in Figures 8.3, 8.4. The radial component of velocity in the wake close to the trailing edge is about ten percent of the free stream velocity and the radial flow in the inviscid region is of the order of one percent of the free stream velocity ($\bar{U}_{so}$). The trend was similar at all other radial stations of measurement downstream of the rotor.

The velocity profiles shown in Figures 8.3, 8.4 are typical of a three-dimensional wake and are unsymmetrical about the wake centerline. The asymmetry is preserved downstream of the rotor. The appearance of radial flows in the wake is due to the imbalance of centrifugal and

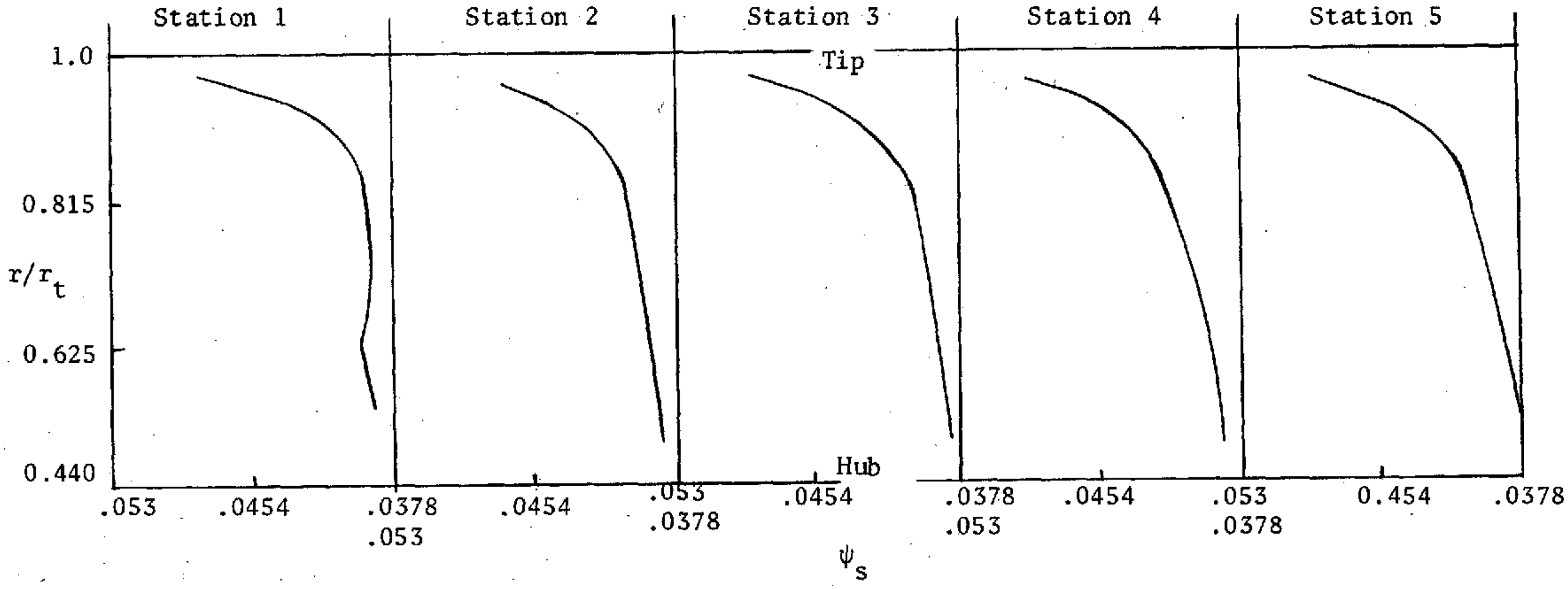

Figure 8.2 Static Pressure Coefficient Distribution from Hub to Tip at Various Axial Locations Downstream of the Rotor.

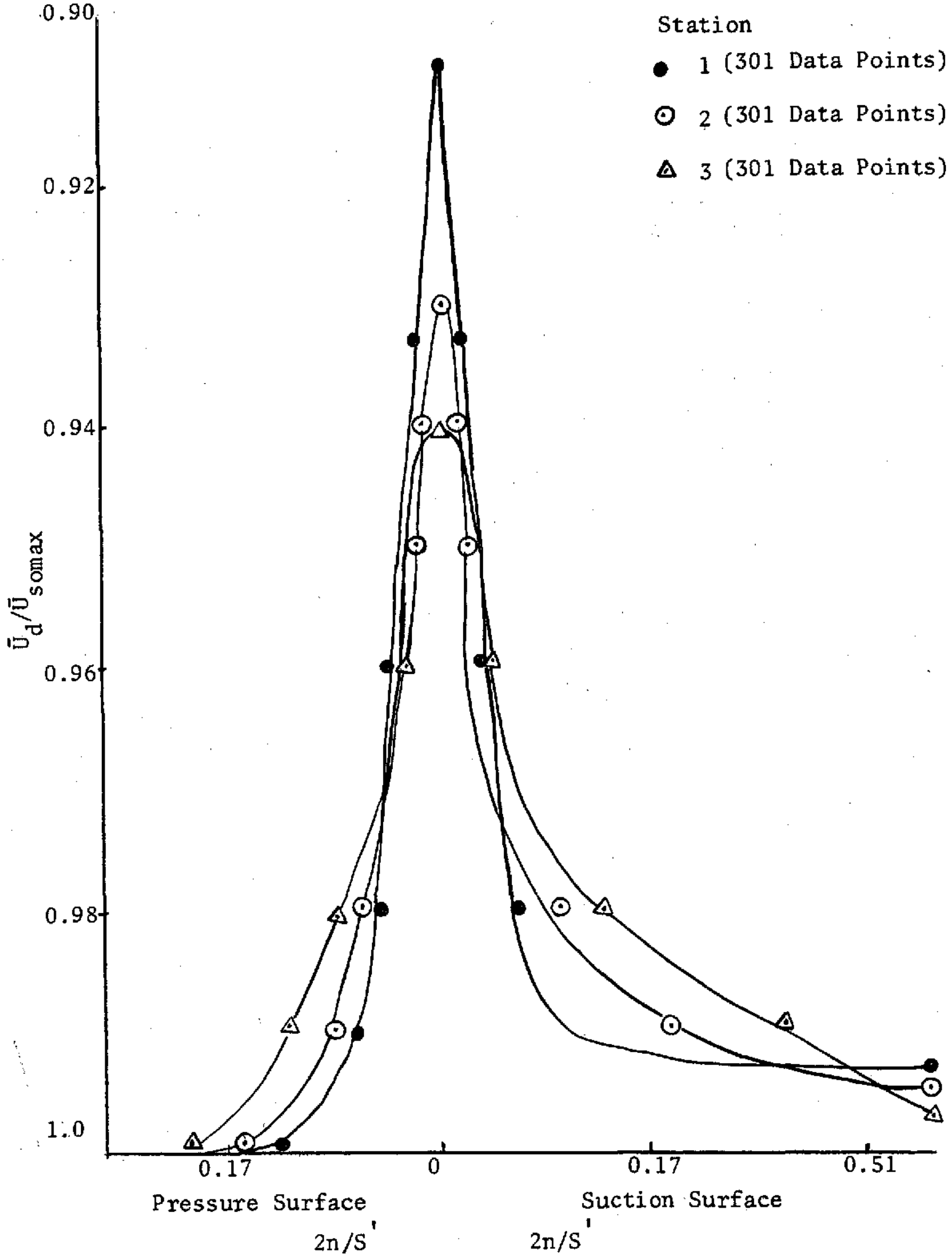

Figure 8.3 Distribution of Streamwise Component of Mean Velocity in a Rotor Wake.

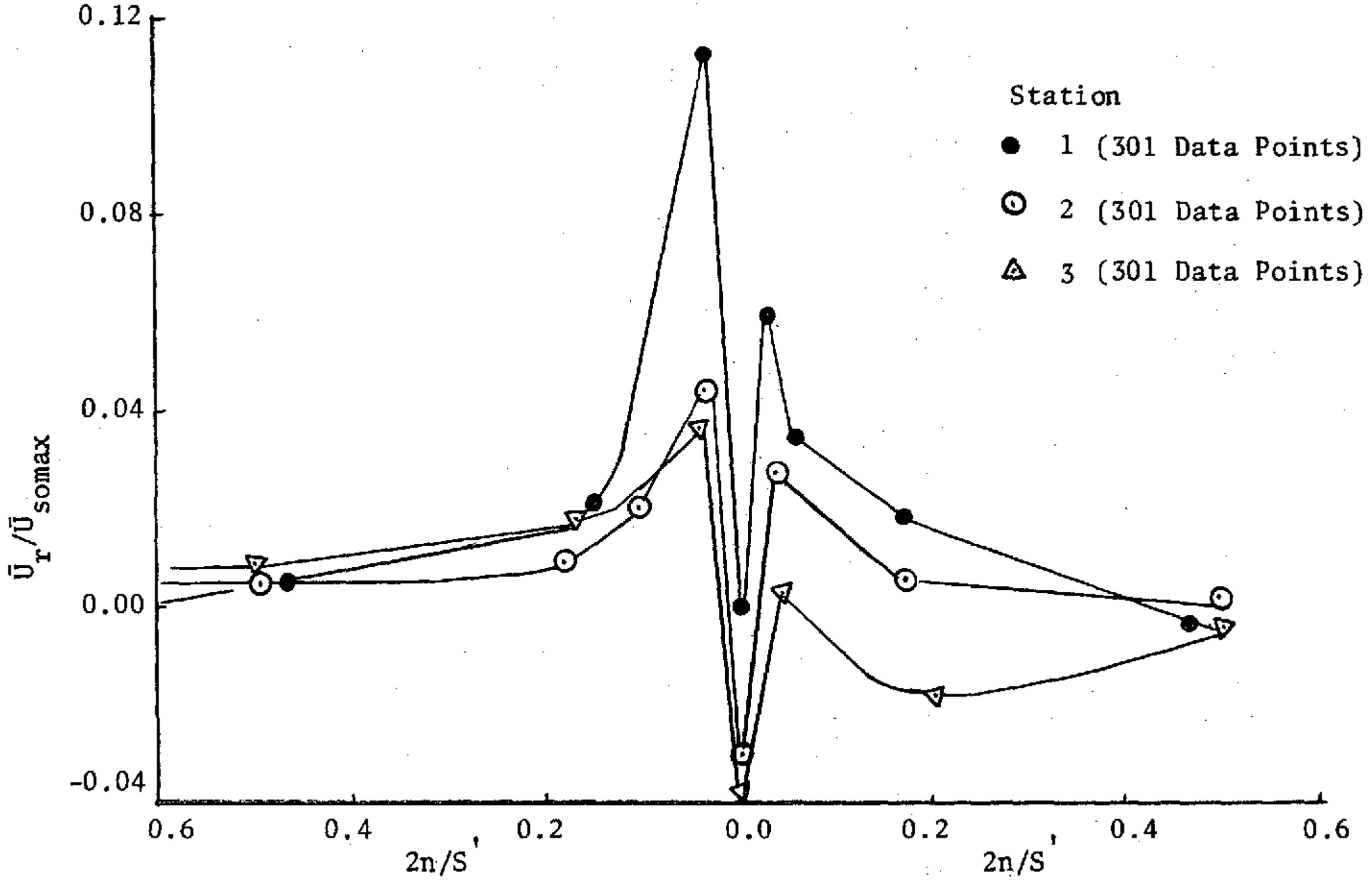

Figure 8.4 Distribution of Radial Component of Mean Velocity in a Rotor Wake.

pressure forces inside the wake and its direction is outward very close to the wake centerline. The peak radial velocities occur away from the wake centerline and radial velocities are very small at the wake edge and the wake centerline.

8.3.1 Self Similarity

In Figure 8.5, an attempt is made to reduce the streamwise mean component of velocity to a single curve using the scaling velocity $\bar{U}_d$ and two different length scales (ℓ_{os} and ℓ_{op}), which are distances on the suction and pressure sides of the wake centerline from the point of minimum velocity to a point where the velocity defect is $\bar{U}_d/2$.

Figure 8.5 shows the existence of similarity in the velocity profile when the velocity and length scales described above are used. The profiles become nearly symmetrical about the wake centerline. The streamwise velocity profile does not show close agreement with the gaussian distribution [i.e., $e^{-\eta_3^2}$ or $(1-\eta_3^{3/2})^2$] unlike a cascade wake (Ref. 49), except near the wake centerline.

A close examination of Figure 8.4 also shows that the mean components of radial velocity are also nearly similar.

8.3.2 The Decay Laws

Figure 8.6 shows the variation of the wake centerline velocity defect (streamwise component) with streamwise distance downstream of the rotor. The data for cascade of airfoils (Ref. 49) and isolated airfoil (Ref. 48) are compared with rotor wake data in Figure 8.6.

The data on rotor wakes was used to find the R_s in Equation (5.28). Due to finite thickness of the trailing edge, it is necessary to add a

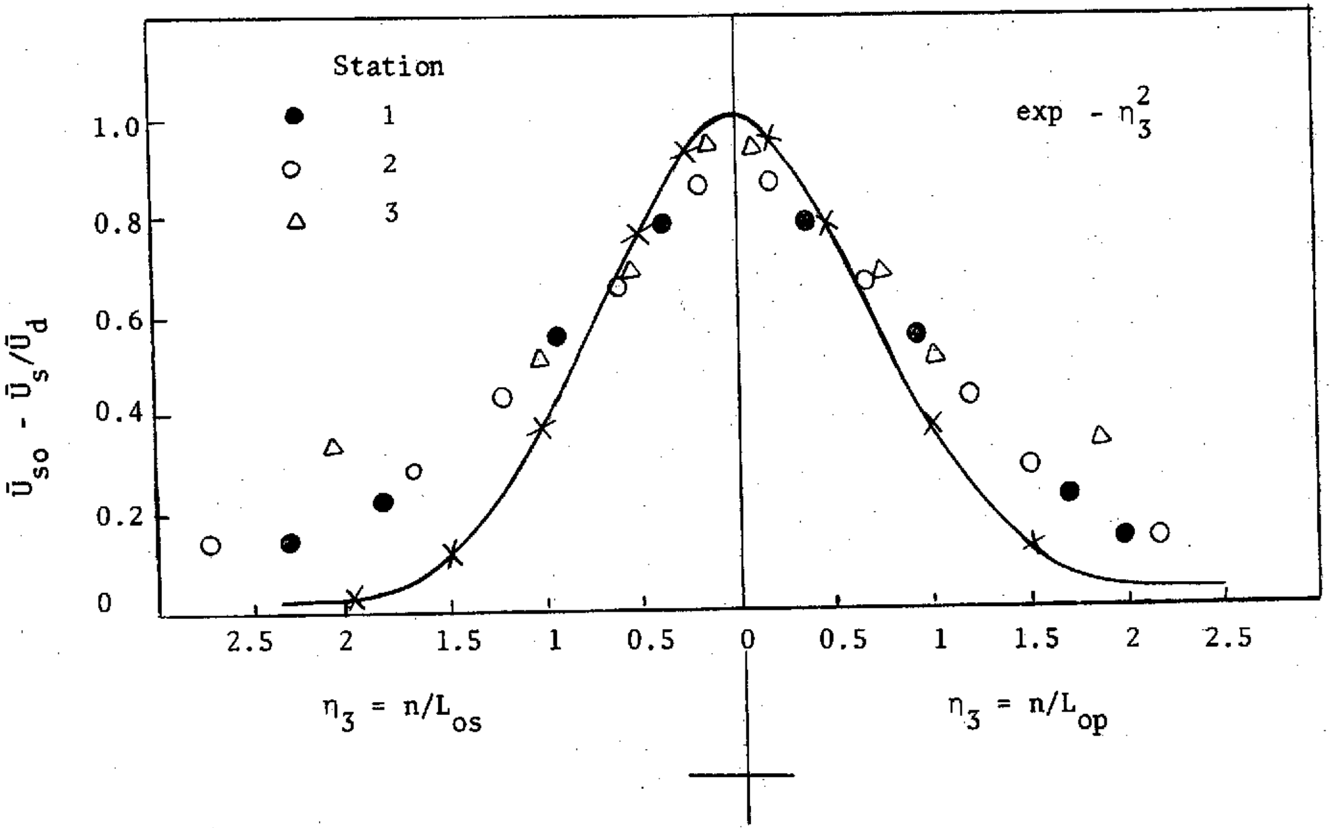

Figure 8.5 Similarity in Streamwise Component of Mean Velocity in a Rotor Wake.

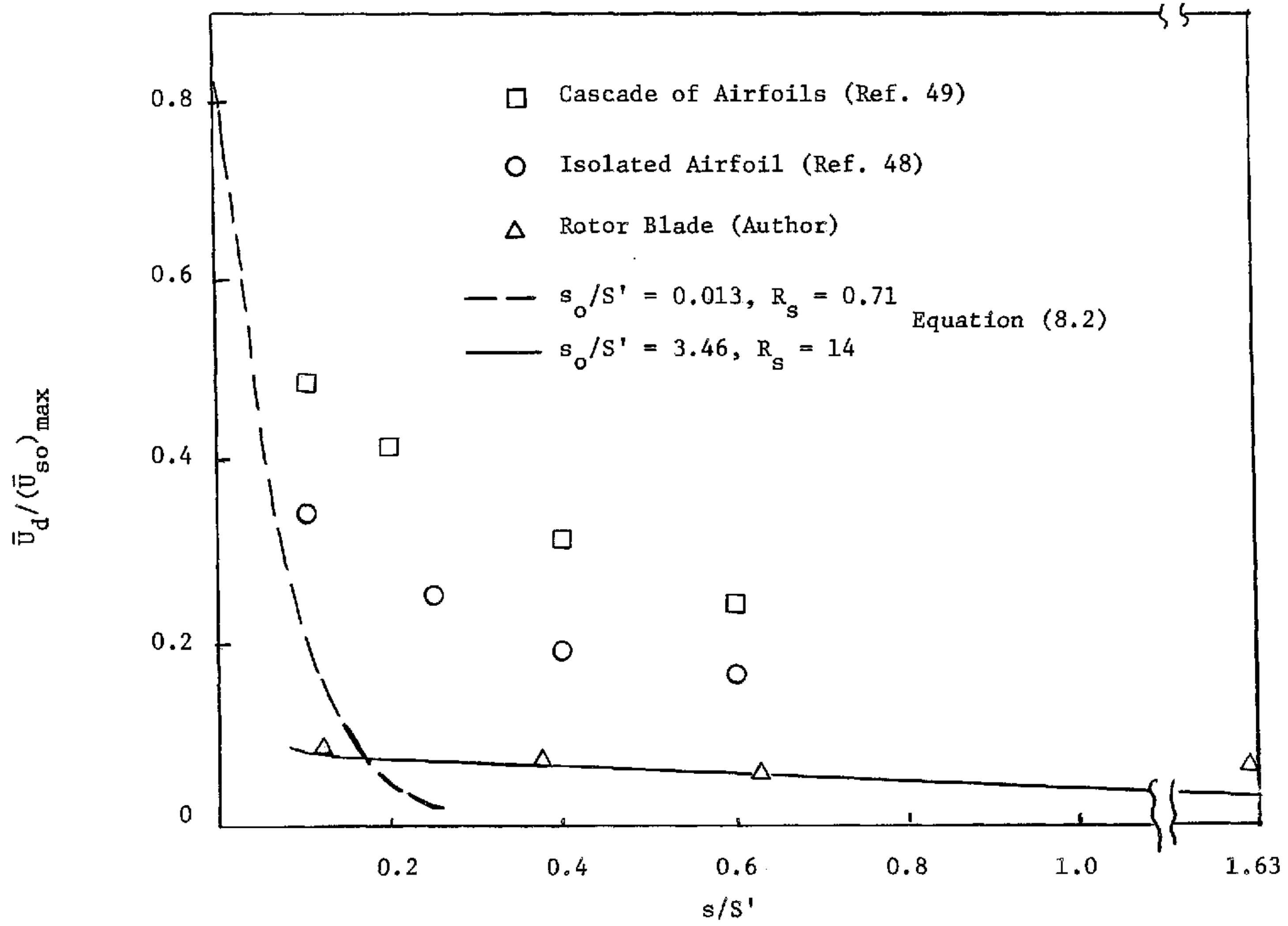

Figure 8.6 Variation of Wake Centerline Mean Velocity Defect (Streamwise Component) with Streamwise Distance Downstream of the Rotor $(r/r_t) = 0.58$).

value of the virtual origin to s in Equation (5.28). With the abovementioned additions, Equation (5.28) takes the following form:

$$\frac{\bar{U}_d}{\bar{U}_{so}} = \exp\left[-\pi^2/R_s\ (s/S' + s_o/S')\right] . \tag{8.2}$$

The constant s_o in the above expression depends on the trailing edge thickness and R_s should depend on the flow and blade parameters of the rotor.

The rate of wake decay very near the trailing edge is found to be very large (Figure 8.6) and, in this region, $R_s = 0.71$ and $s_o/S' = 0.013$. Equation (8.2), with these constants, is valid up to $s/S' = 0.15$. These constants will be different farther downstream, since the diffusion properties which control the value of R_s through eddy viscosity changes. Furthermore, the virtual origin is now dependent on the slope of the wake spread and not the trailing edge thickness. In the region $s/S' > 0.15$, the constants in Equation (8.2) were found to be $s_o/S' = 3.46$ and $R_s = 14.00$.

A few important observations can be made from Figure 8.6. (a) The streamwise component of wake centerline velocity recovered to within 90 percent between trailing edge and one quarter chord length downstream. (b) The rate of decay of rotor wake velocity defect in the streamwise direction is faster than those of a cascade of airfoils (Ref. 49) or an isolated airfoil (Ref. 57). (c) Different values of R_s indicate that the wake diffusion properties change considerably from the trailing edge to distances farther downstream.

The decay rate of the radial component of velocity (maximum value) is shown in Figure 8.7. The decay of the maximum radial velocity seems to follow the following relationship (Figure 8.7):

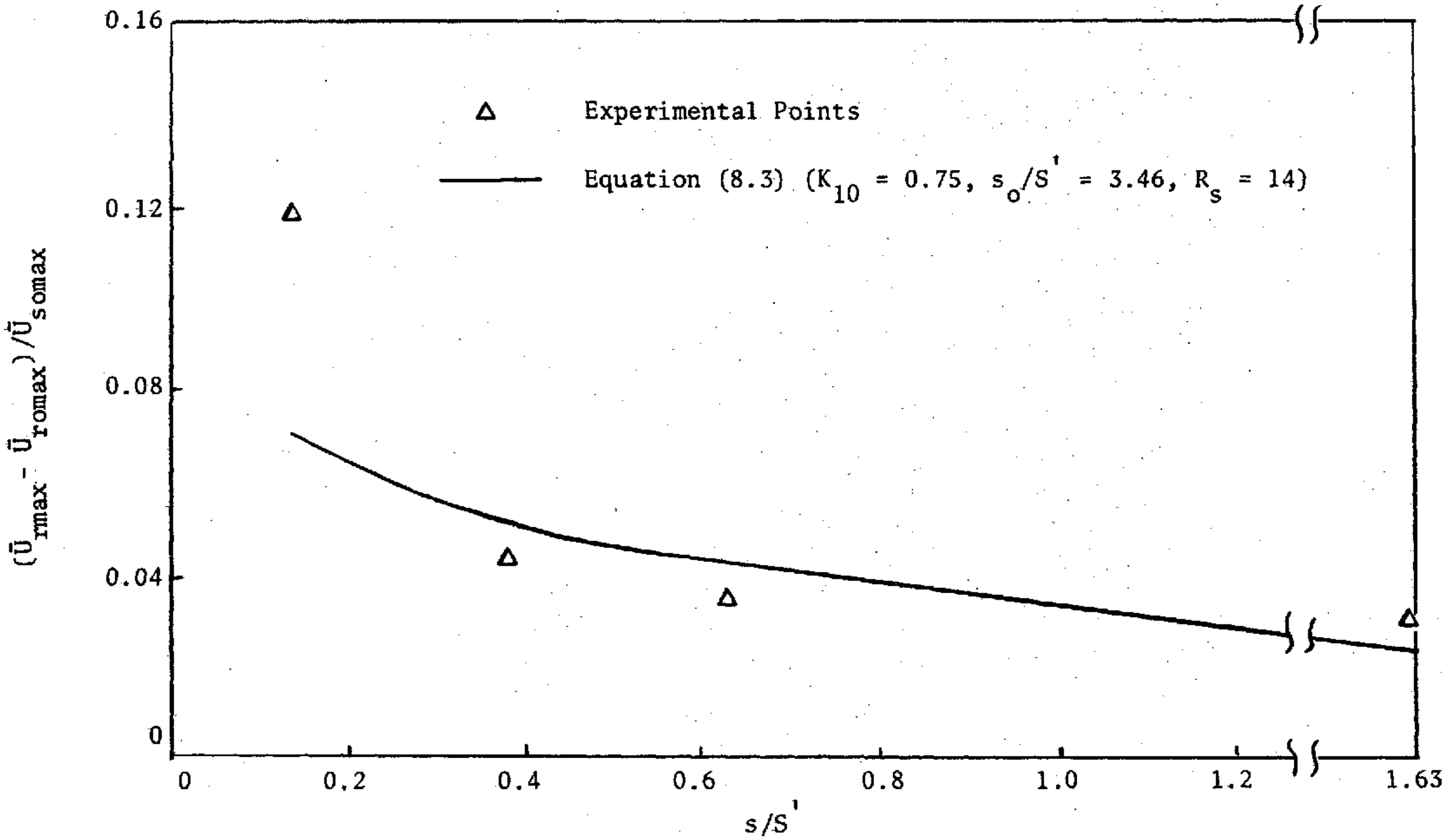

Figure 8.7 Variation of Radial Component of Mean Velocity (Maximum Value) with Streamwise Distance Downstream of the Rotor (r/r_t = 0.58).

$$\frac{(\bar{U}_r)_{max} - (\bar{U}_{ro})_{max}}{\bar{U}_{somax}} = K_{10} \exp\left[\frac{\pi^2}{R_s}\left(\frac{s}{S'} + \frac{s_o}{S'}\right)\right] . \quad (8.3)$$

These constants are the same as those for the decay of streamwise component with the exception of K_{10}. The value of K_{10} is found to be equal to 0.75 for $s/S' > 0.1$.

8.3.3 Wake Width

The variation of half the wake width (ℓ) along streamwise and radial direction is plotted in Figure 8.8. At $r/r_t = 0.58$, there is negligible variation in 'ℓ' along the radial direction, except near the hub wall. The largest value of half the wake width at the hub may be due to complex interaction of wake, hub wall boundary layer and secondary flows. A logarithmic plot of the variation of half the wake width (ℓ) with streamwise direction is shown in Figure 8.9 for $s/S' >$ 0.15, the half wake width at $r/r_t = 0.58$ satisfy the following relationship:

$$\frac{\ell}{\ell_o} = 1.93\ (s/S')^{0.318}, \quad (8.4)$$

where ℓ_o is the value of half the wake width at $s/S' = 0.15$ (first measuring station).

8.4 Turbulence Quantities

8.4.1 Turbulence Intensity

The distribution of turbulence intensities in the streamwise (T_s), transverse (T_n) and in radial directions (T_r) at various axial stations is shown in Figures 8.10, 8.11, 8.12, 8.13. The data is presented for

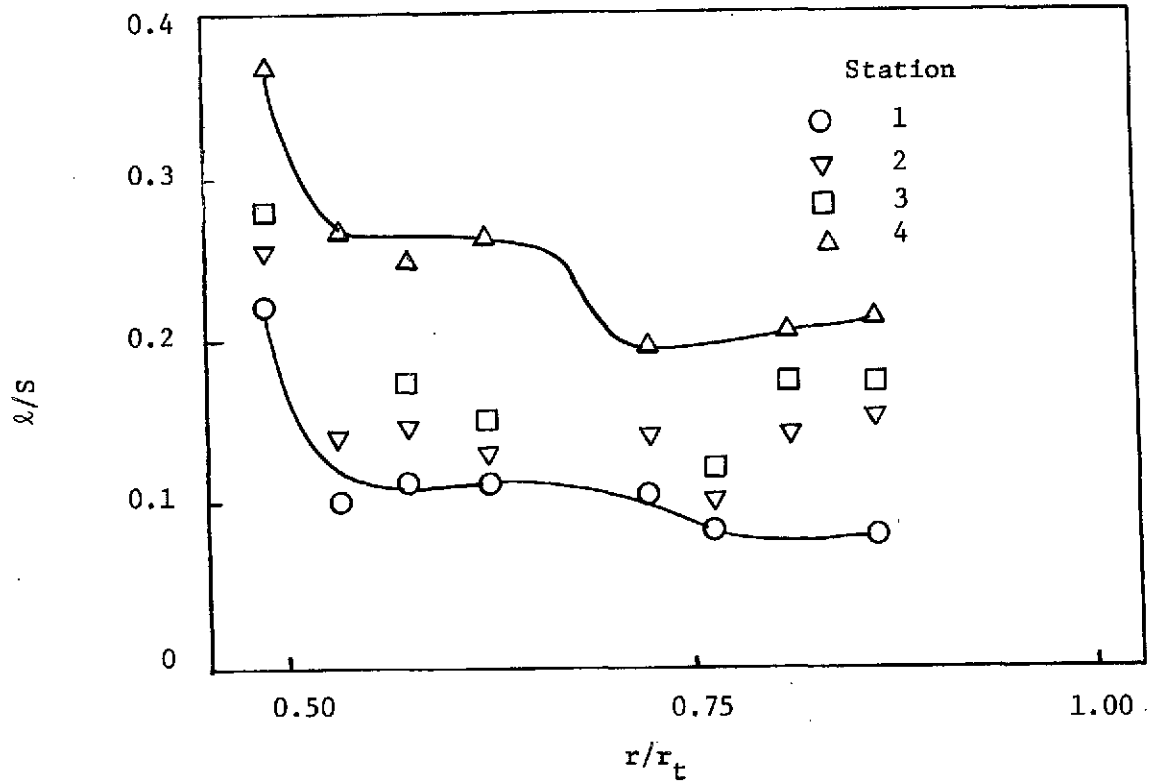

Figure 8.8 Streamwise and Radial Variation of Half the Wake Width (ℓ) in a Rotor Wake

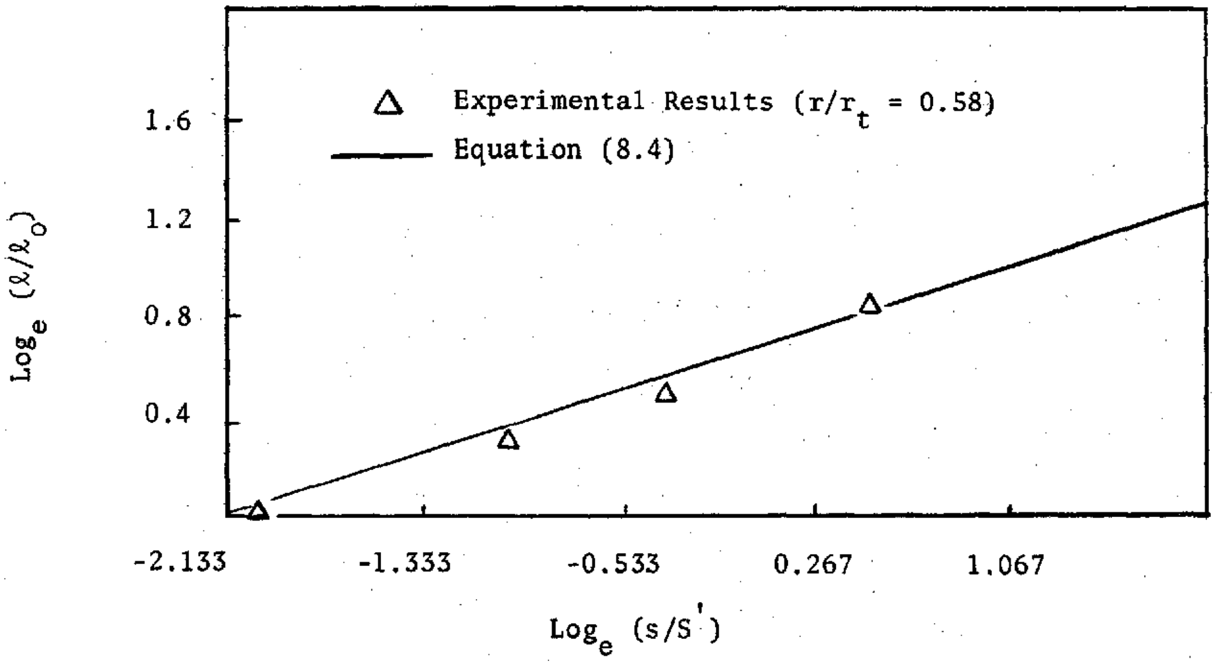

Figure 8.9 Logarithmic Plot of the Variation of Half the Wake Width with Streamwise Distance (r/r_t = 0.58).

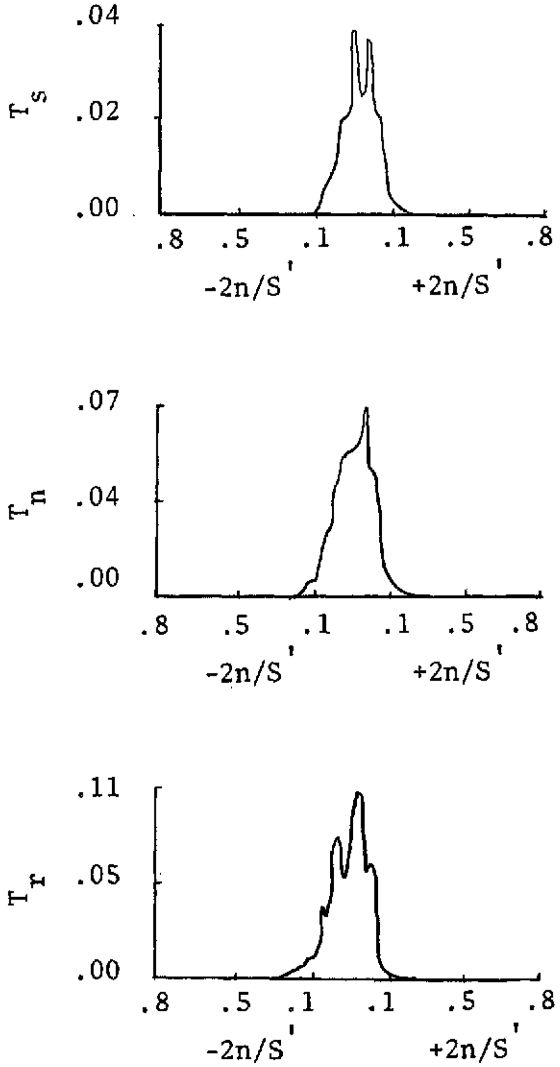

Figure 8.10 Distribution of Turbulence Intensities T_s, T_n, and T_r Across the Rotor Wake at Station 1 $(r/r_t) = 0.58$).

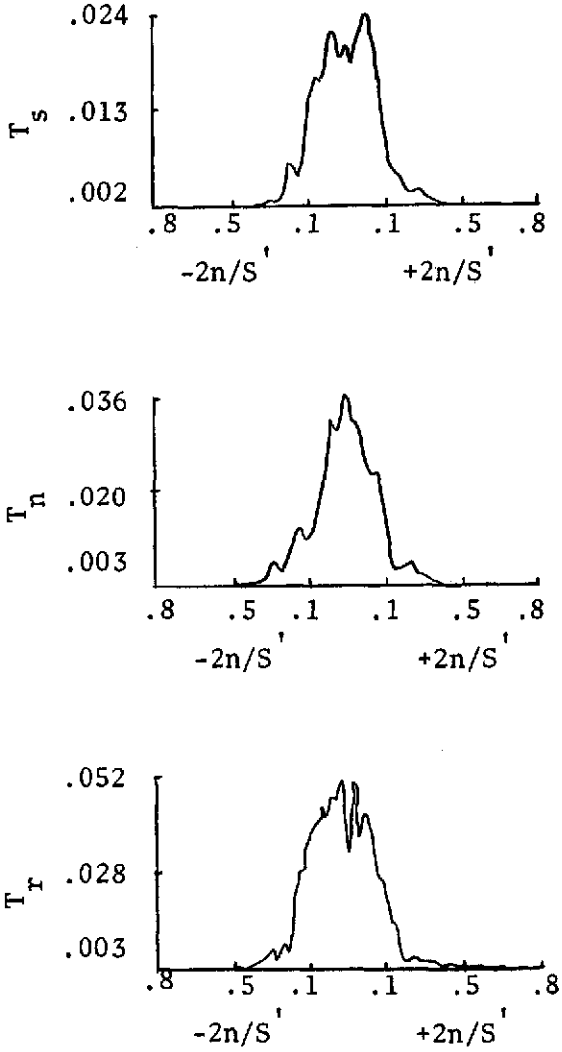

Figure 8.11 Distribution of Turbulence Intensities T_s, T_n, and T_r Across the Rotor Wake at Station 2 (r/r_t = 0.58).

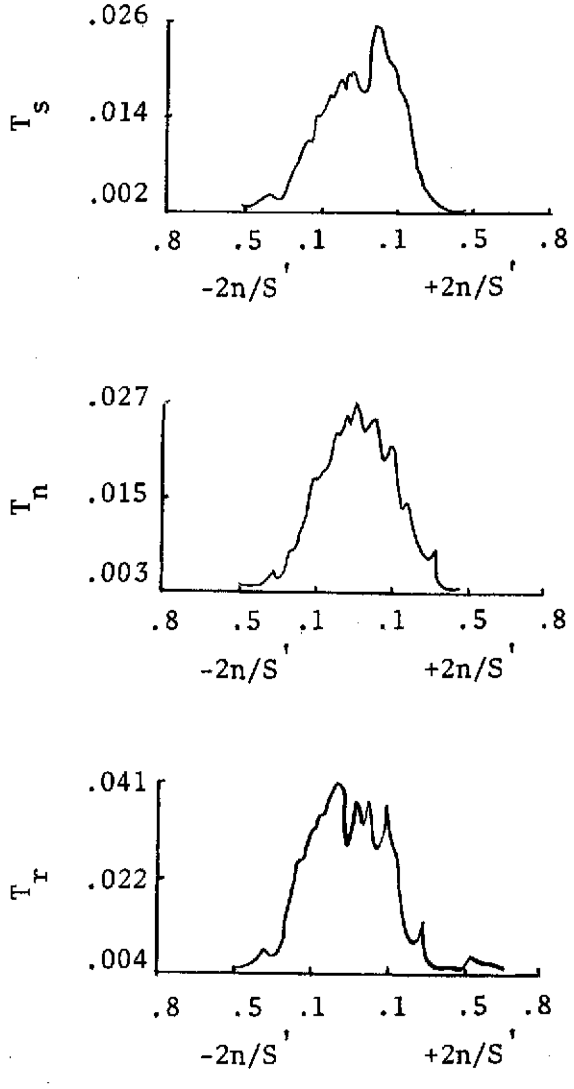

Figure 8.12 Distribution of Turbulence Intensities T_s, T_n, and T_r Across the Rotor Wake at Station 3 (r/r_t = 0.58).

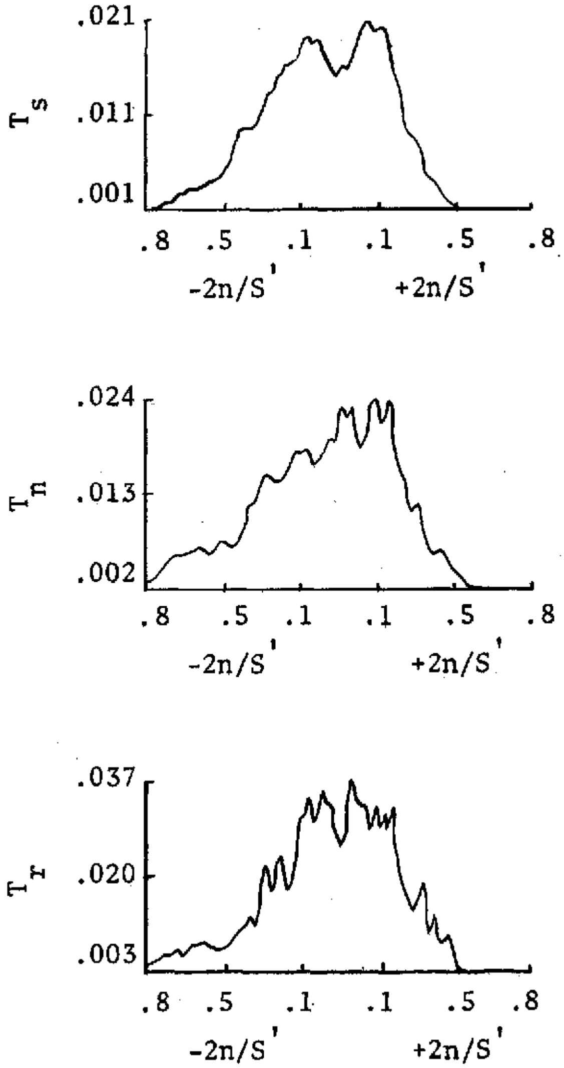

Figure 8.13 Distribution of Turbulence Intensities T_s, T_n, and T_r Across the Rotor Wake at Station 4 ($r/r_t = 0.58$).

one radial station ($r/r_t = 0.58$), since the trend is similar at all other radial stations. The turbulence intensity profiles are asymmetric about the wake centerline and this asymmetry is retained even far downstream of the rotor (one chord length). Furthermore, there is a tendancy (in the radial and streamwise directions) for the occurrence of a dip close to the wake centerline.

The largest component of turbulence intensity is in the radial direction. The ratio of T_r/T_n and T_r/T_s are 1.49 and 2.34, respectively, near the trailing edge and 1.47 and 1.69 farther downstream of the trailing edge. The ratio of turbulence intensities shows that the turbulence is highly anisotropic close to the trailing edge of the rotor blade and has the tendency towards isotropy further downstream. The free stream turbulence level is found to be about 0.1 percent.

A theoretical explanation of the redistribution of energy between the three components of fluctuating velocities is given by Raj and Lumley (50). It is pointed out that, if the gradient of the radial component of mean velocity across the wake is much larger than the angular velocity of the machine, then,

$$T_r > T_n > T_s$$

This is confirmed by data presented here. The anisotropy introduced into the flow is due to the presence of blade, rotation and the pressure gradients.

The decay rate of the turbulence intensities with streamwise distance downstream of the rotor is shown in Figure 8.14 and compared with the decay rates of turbulence intensities in a cascade wake. It is evident from Figure 8.14 that all the components of turbulence

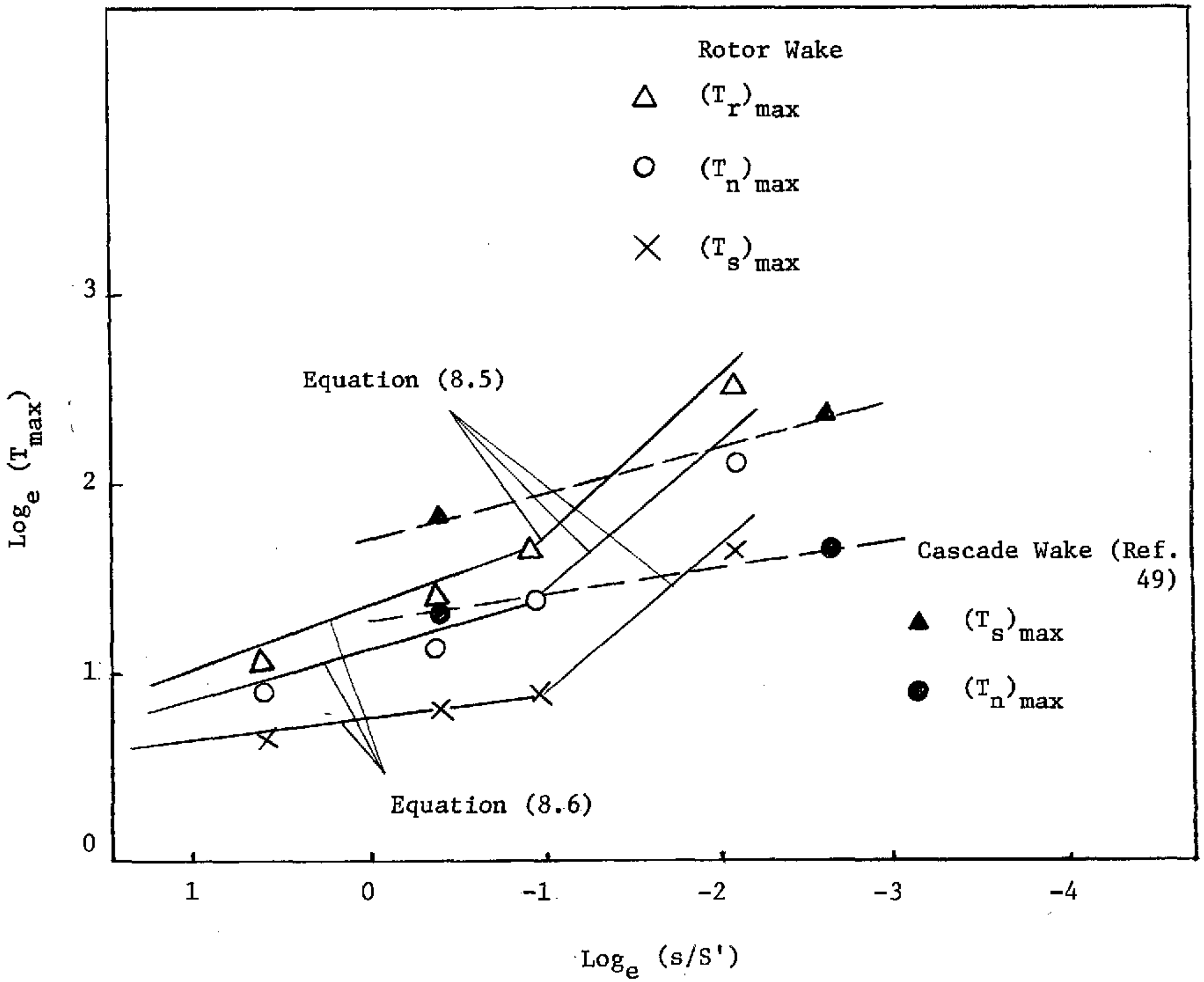

Figure 8.14 Logarithmic Plot of the Variation of Three Components of Turbulence Intensity (Maximum Value) with Streamwise Distance ($r/r_t = 0.58$).

intensities decay at the same rate close to the trailing edge according to the following expression ($0.15 < s/S' < 0.36$):

$$(T)_{max} = A(s/S')^{-0.78} \quad . \tag{8.5}$$

The value of constant A is found to be 0.109, 0.017, and 0.025, respectively, for s, n, and r components. Farther downstream, the intensities decay at different rates as represented by the following relations ($s/S' > 0.36$):

$$\begin{aligned} (T_r)_{max} &= 0.037\ (s/S')^{-0.32} \\ (T_n)_{max} &= 0.028\ (s/S')^{-0.249} \\ (T_s)_{max} &= 0.021\ (s/S')^{-0.122} \end{aligned} \tag{8.6}$$

The above relations show that decay rate of $(T_r)_{max}$ is the largest of all components of turbulence intensities.

A comparison of the decay rates of turbulence intensities of rotor and cascade wakes (Ref. 49) shows that the turbulence level, anisotropy and decay rate in a rotor wake is higher than that of cascade wake.

8.4.2 Reynolds Stress

In figures 8.15, 8.16, 8.17, 8.18 are shown the distribution of components of Reynolds stress τ_{sn}, τ_{rn}, and τ_{sr} at all the axial stations downstream of the trailing edge of the rotor blade for r/r_t = 0.58.

The largest component of Reynolds stress is τ_{rn}. The ratios τ_{rn}/τ_{sn} and τ_{rn}/τ_{sr} are 2 and 3.1 respectively near the trailing edge and 1 and 1.5 farther downstream. The ratio of Reynolds stresses show that they have a tendency to reach the same value. The theoretical

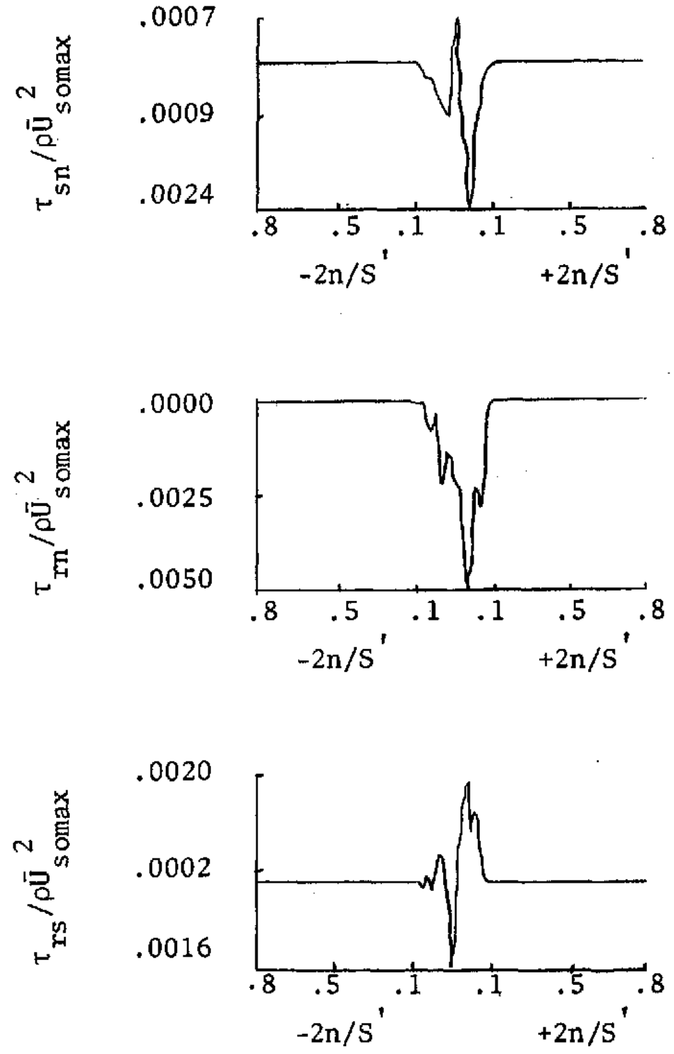

Figure 8.15 Distribution of the Components of Reynolds Stress τ_{sn}, τ_{rn}, and τ_{rs} Across the Rotor Wake at Station 1 (r/r_t = 0.58).

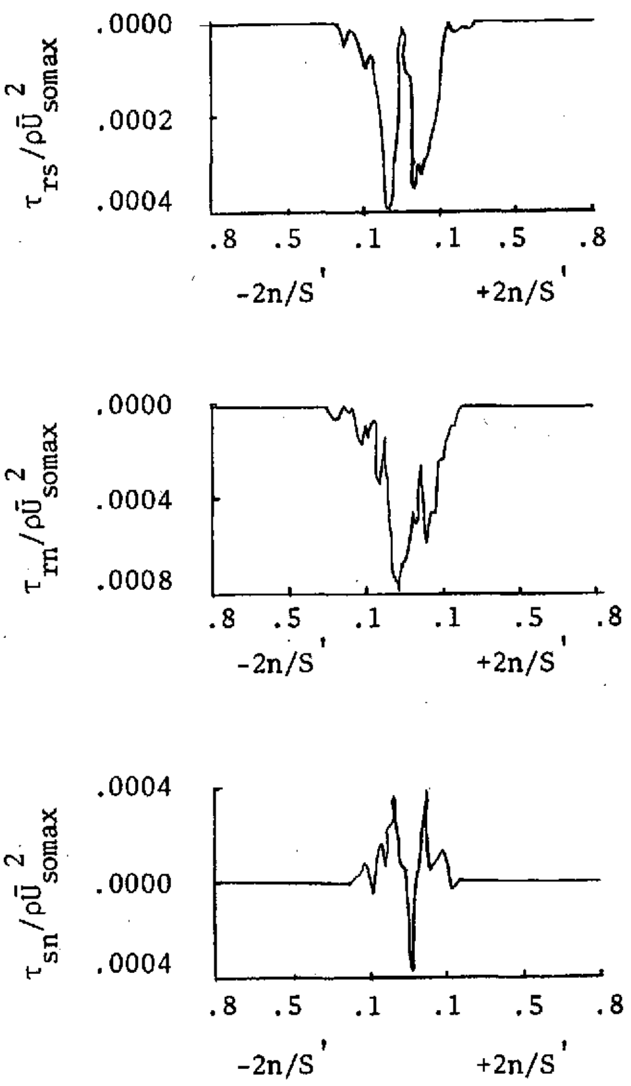

Figure 8.16 Distribution of the Components of Reynolds Stress τ_{sn}, τ_{rn}, and τ_{rs} Across the Rotor Wake at Station 2 (r/r_t = 0.58).

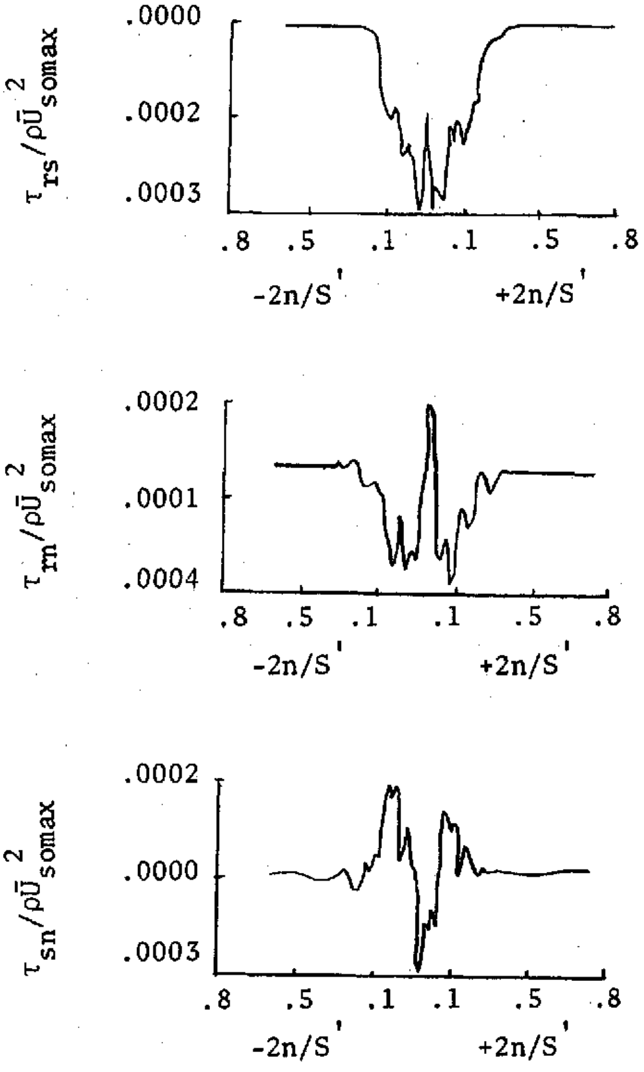

Figure 8.17 Distribution of the Components of Reynolds Stress τ_{sn}, τ_{rn}, and τ_{rs} Across the Rotor Wake at Station 3 ($r/r_t = 0.58$).

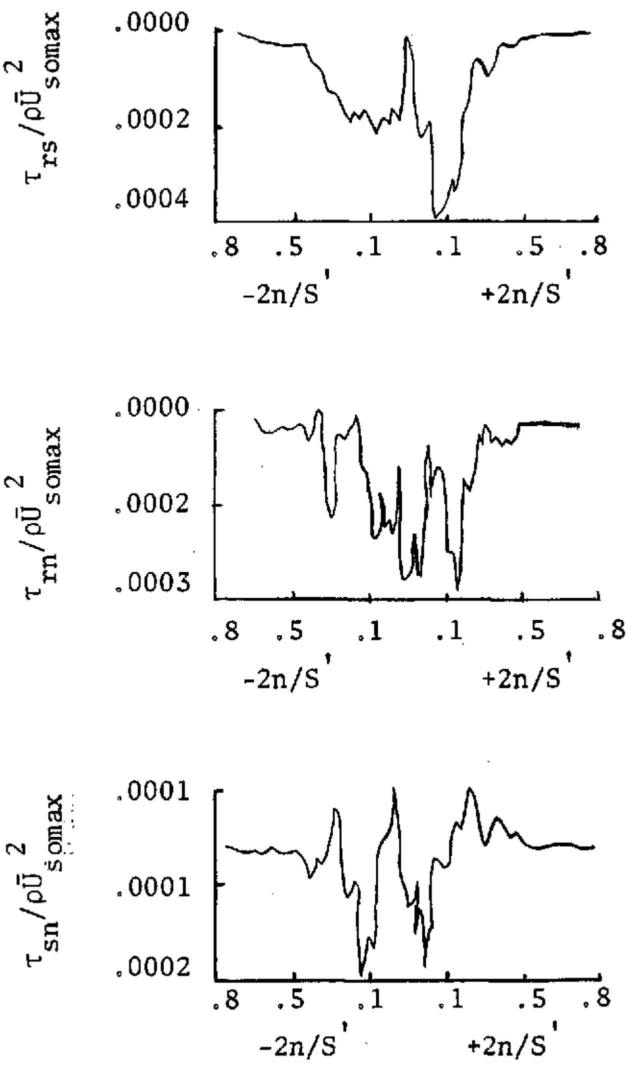

Figure 8.18 Distribution of the Components of Reynolds Stress τ_{sn}, τ_{rn}, and τ_{rs} Across the Rotor Wake at Station 4 ($r/r_t = 0.58$).

explanation for the occurrence of the largest value of Reynolds stress can be based on the largest values of mean velocity gradients in the n direction.

While no analysis is carried out for the prediction of Reynolds stresses, decay laws can be derived from the experimental data. A plot of the variation of maximum values of the components of Reynolds stress (τ_{sn}, τ_{rn}, and τ_{sr}) downstream of the rotor is shown in Figure 8.19. It is clear that all Reynolds stresses first decrease rapidly ($0.15 < s/S' < 0.36$). Then, they decay at nearly the same rate. Near the trailing edge ($0.15 < s/S' < 0.36$), the decay follows the expressions

$$\begin{aligned} \tau_{rn} &= 0.001\ (s/S')^{-2.05} \\ \tau_{sn} &= 0.0006\ (s/S')^{-1.92} \qquad (8.7) \\ \tau_{rs} &= 0.0004\ (s/S')^{-1.92} \end{aligned}$$

Farther downstream, all the components of Reynolds stress decay at nearly the same rate and is given by:

$$\tau = 0.0003\ (s/S')^{-0.267}. \qquad (8.8)$$

It is necessary to point out that the data on Reynolds stress is qualitative in nature.

A comparison of decay laws for Reynolds stress in a cascade wake (Ref. 49) and that of a rotor wake indicate that Reynolds stress decays faster in the rotor wake.

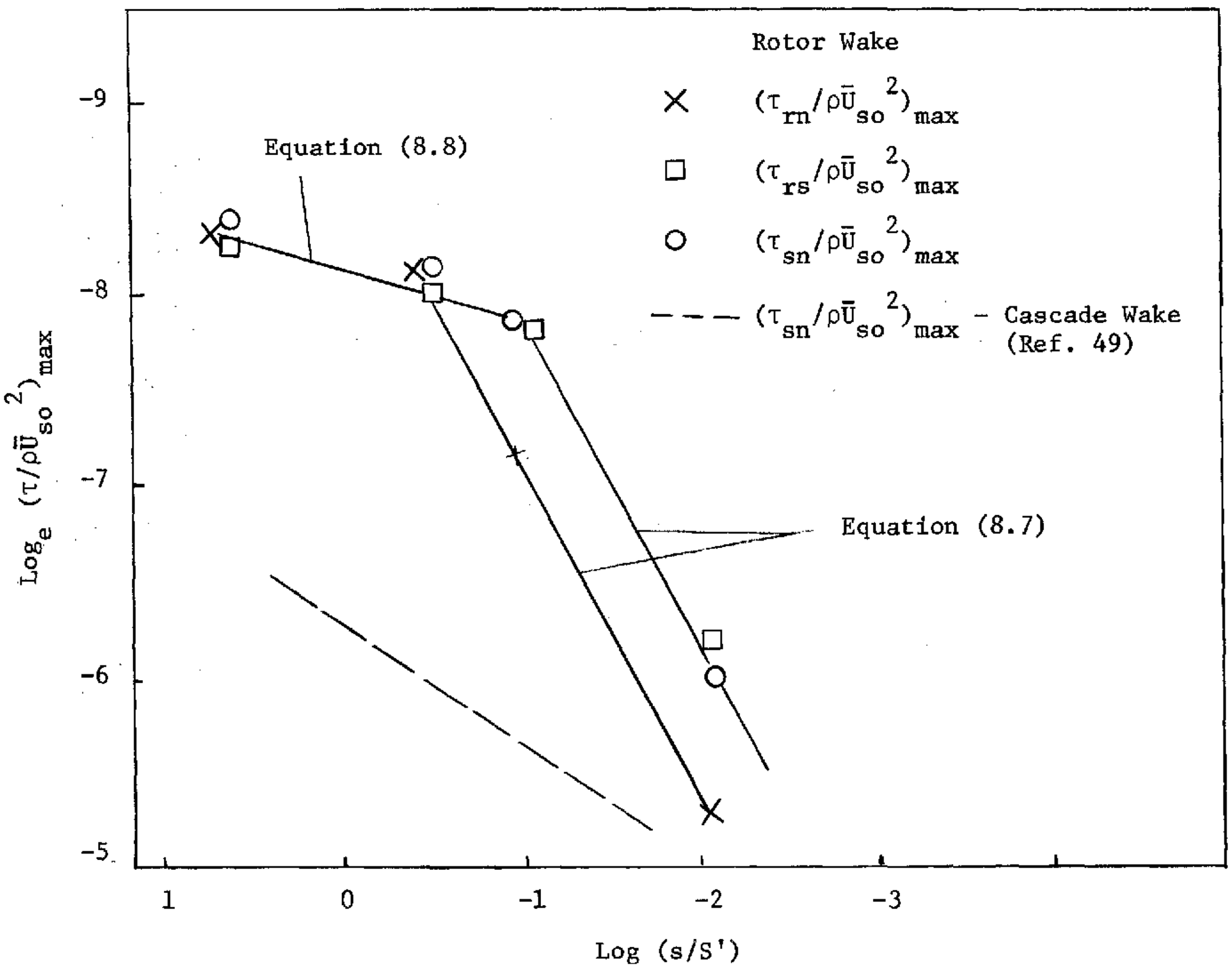

Figure 8.19 Logarithmic Plot of the Variation of Three Components of Reynolds Stress (Maximum Value) with Streamwise Distance ($r/r_t = 0.58$).

8.4.3 Ratio of Total Reynolds Stress (τ_o) to Total Turbulence Energy ($\rho\overline{q^2}$)

A plot of $G(|\tau_o|/\rho\overline{q^2})$ at various axial stations across the wake is shown in Figure 8.20 for $r/r_t = 0.58$. It is clear from this that the variation of G across the wake is not constant and has a wide variation ranging from 0.06 to 0.48. This serves as a caution for those who are contemplating to use Bradshaw et al.'s (6) turbulence model (where G is assumed to be constant) for predicting three-dimensional wake flows.

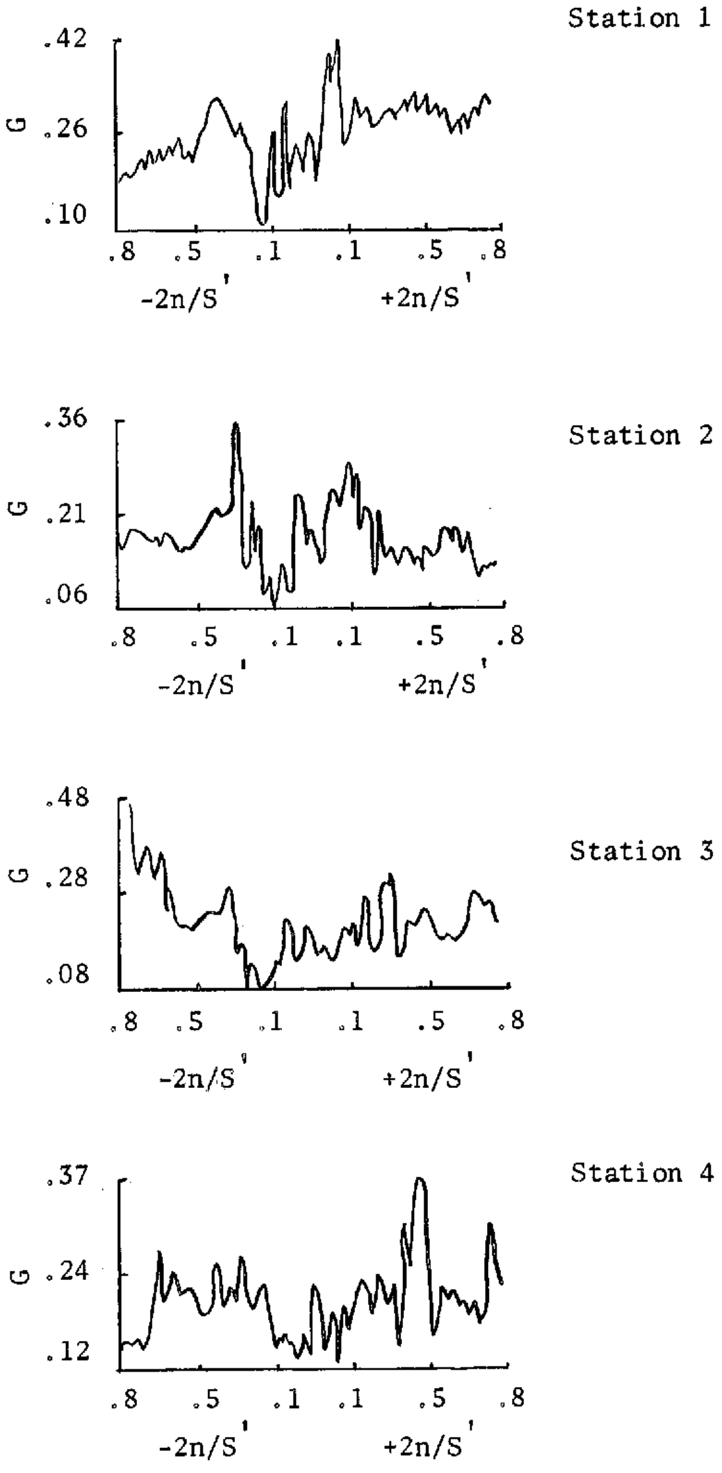

Figure 8.20 Variation of G Across the Wake at Various Axial Stations ($r/r_t = 0.58$).

CHAPTER IX

CONCLUSIONS

9.1 Cascade Wake

The experimental and analytical investigations reported in Chapter VII indicate that the wake of a cascade of airfoils differs from that of a cylinder, flat plate, or isolated (symmetrical) airfoil at zero incidence, in several respects.

(i) The wake is asymmetrical. When two different length scales are used, one for each side of the wake, mean velocity profiles become symmetrical about the wake centerline.

(ii) The wake edge velocity changes continuously, giving rise to either slower decay of the wake defect (as in the case of a cascade with decelerating free-stream flow) or faster decay (as in the case of accelerating mean flow). The mean velocity profile is of the type $(1 - \eta^{3/2})^2$, where $\eta = y/\ell_{os}$ or y/ℓ_{op}, and ℓ_{os}, ℓ_{op} are length scales on the suction and pressure side of the wake, respectively. The wake centerline velocity is well represented by Equation (4.27), and the width of the wake by Equation (7.1).

(iii) Turbulence intensities are higher than those of a flat plate wake, even though decay characteristics shown in Equations (7.5) and (7.6) are nearly the same. Maximum Reynolds stress and decay characteristics are given by Equation (7.7).

The change in cascade parameters (e.g., solidity c/S and incidence i) has a dual effect. Solidity is likely to change the wake edge velocity (m in the equation $\bar{U}_{zo} \sim z^{-m}$) and the profile drag. Both of these change the wake decay characteristics. But in the far wake, where

$\bar{U}_{zo} \sim$ const., the velocity defect at the wake centerline is inversely proportional to solidity. The incidence and camber effects (which directly control boundary-layer growth, blade loading and drag coefficient) would similarly influence the decay rate through the parameters c_d and m. The results reported here adequately demonstrate this.

Schlichting (56), while investigating the far wake of a cascade of circular cylinders, derived a theoretical expression for the mean velocity, which shows no dependency on c_d. This is due to the fact that the c_d for a circular cylinder in the Reynolds number range of 10^4 to 10^5 is nearly unity, while that of a cascade of blades is two or three orders of magnitude less.

The peak in turbulence intensity may occur at the wake centerline in a cascade, depending on the thickness of the blade and the downstream distances. Experimental data of Reynolds (53) show a similar trend. For large-diameter cylinders, the interaction of the mean-velocity defect and the turbulence intensity is delayed, resulting in the occurrence of the turbulence peak at the wake centerline. However, the turbulence intensity peak will be away from the wake centerline for the same cylinder at larger downstream distances.

No attempt is made in this paper to investigate the effect of inlet turbulence. At higher levels of free-stream turbulence, the wake decay characteristics may be different. The data of Eagleson et al. (21) for a flat plate wake in a water tunnel indicate that the near wake decay law changes from $z^{-1/2}$ to z^{-1} when the turbulence level is around 4 to 7 percent. This is an area where further research is needed.

9.2 Rotor Wake

The experimental and analytical investigations reported in Chapter VIII indicate that the wake of a rotor blade differs from that of an isolated airfoil and a cascade of airfoils in several respects.

(i) The decay rate of wake defect of a rotor blade is higher than that of an isolated airfoil or a cascade of airfoils. The decay law is given by Equation (8.2). However, two differing constants are needed to prescribe the wake decay rate; one closer to the trailing edge, and the second further downstream.

(ii) Although the profiles of mean velocity are nearly similar, the similarity is less pronounced near the edges of the rotor wake as compared to those of an isolated airfoil or cascade of airfoils.

(iii) The anisotropy, the magnitude of turbulence intensities and Reynolds stresses are much higher than that of a cascade wake. The decay rate of the turbulence intensities and Reynolds stresses is also larger compared to a cascade wake.

The large decay in mean velocity gradients immediately downstream of the rotor is due to intense mixing of the wake with the free stream. However, due to large mean velocity gradients, there is a large production of turbulence such that turbulence decay cannot adjust itself to the abrupt changes. Consequently, at some points downstream of the rotor, the gradients in turbulence quantities become larger than those of mean velocities. This is an extremely inequilibrium situation and part of the energy contained in turbulence is fed back to the mean velocity, thus preventing the wake from decaying completely until an equilibrium situation is reached.

One of the important features of this investigation is the fact that the contribution from the wake to the total unsteadiness in the subsequent blade row comes equally from the wake turbulence and the defect in mean velocity. Due to physical constraints, it was not possible to investigate the flow regions in the vicinity of the trailing edge ($s/S^{'} < 0.15$) or the boundary layer characteristics at the trailing edge of the rotor blade. Therefore, it should be planned to fully investigate the wake flow using a rotating hot-wire and conventional probe as described in Appendix B.

REFERENCES

1. Batchelor, G. K., "Note on Free Turbulent Flows, with Special Reference to the Two-Dimensional Wake," J. Aero. Sci., July, 1950.

2. Batchelor, G. K., and Townsend, A. A., "Decay of Isotropic Turbulence in Initial Period," Proc. Royal Soc., Vol. 193, 1948.

3. Berger, S. A., Laminar Wakes, American Elsevier, New York, 1971.

4. Bradshaw, P., "Prediction of the Turbulent Near-Wake of a Symmetrical Airfoil," J. AIAA, Vol. 8, 1970.

5. Bradshaw, P., "Effects of Streamline Curvature on Turbulent Flow," Advisory Group for Aerospace Research and Development (AGARD) No. AG-169, 1973.

6. Bradshaw, P., Ferriss, D. H., and Atwell, N. P., "Calculation of Boundary Layer Development Using the Turbulent Energy Equation," J. Fluid Mech., Vol. 8, 1967.

7. Bruce, E. P., "The ORL Fluids Engineering Unit Axial Flow Research Fan," ORL TM No. 72-109, The Pennsylvania State University, 1972.

8. Carmody, T., "Establishment of a Wake Behind a Disk," Trans. ASME, Dec., 1964.

9. Champagne, F. H., Sleicher, C. A., and Wehrmann, O. H., "Turbulence Measurements with Inclined Hot-Wires," Part I, J. Fluid Mech., Vol. 28, 1967.

10. Chanaud, R. C., "Measurements of Mean Flow Beyond a Rotating Disc," J. Basic Engg., June 1971.

11. Chauvin, J., "Turbomachinery Laboratory," Von Karman Inst. TM No. 9, Revised, Rhode-Saint-Genese, Belgium, July 1962.

12. Chervinsky, A., and Lorenz, D., "Decay of Turbulent Axisymmetical Free Flows with Rotation," Trans. ASME, Dec. 1967.

13. Chevray, R., "The Turbulent Wake of a Body of Revolution," J. Basic Engg., June 1968.

14. Chevray, R., and Kovasznay, S. G., "Turbulence Measurements in the Wake of a Thin Flat Plate," J. AIAA, Vol. 7, 1969.

15. Chou, P. Y., "On the Velocity Correlations and the Solution of the Equations of Turbulent Fluctuation," Quart. Appl. Math., Vol. 3, 1945.

16. Cooper, D. R., and Lutzky, M., "Exploratory Investigation of the Turbulent Wakes Behind Bluff Bodies," David Taylor Model Basin Report No. 963, Oct. 1965.

17. Cordes, G., "Statische Druckmessung in Turbulenter Strömung," Ing. Arch., Vol. 8, 1937.

18. Csandy, G. T., Theory of Turbomachines, McGraw-Hill Book Company, New York, 1964.

19. Daly, B. J., and Harlow, F. H., "Transport Equations in Turbulence," J. Physics of Fluids, Vol. 13, 1970.

20. Donaldson, C. D., "Calculation of Turbulent Shear Flows for Atmospheric and Vortex Motions," J. AIAA, Vol. 10, 1972.

21. Eagleson, P. S., Huval, C. J., and Perkins, F. E., "Turbulence in the Early Wake of a Fixed Flat Plate," MIT Hydrodynamic Lab., TR No. 46, Feb. 1961.

22. Ermshaus, R., "Typical Features of Turbulent Wake Flows," Translated from Mitt. aus dem Max-Planck-Inst. für Strömungsforschung u. der Acrodyn. Versuchsanst. Göttingen No. 46, 1970. Translation Published by The Applied Physics Lab. of The Johns Hopkins Univ., Md.

23. Evans, R. L., "Turbulence and Unsteadiness Measurements Downstream of a Moving Blade Row," ASME Paper 74-GT-73, 1974.

24. Gartshore, I. S., "Two-Dimensional Turbulent Wakes," J. Fluid Mech., Vol. 30, 1967.

25. Gearhart, W. S., and Ross, J. R., "A Subsonic Cascade Test Facility," ORL TM 502-02, The Pennsylvania State University, March 1970.

26. Goldstein, S., "On the Two-Dimensional Steady Flow of a Viscous Fluid Behind a Solid Body," Appendix by A. Fage., Proc. Royal Soc., Vol. 142, 1953.

27. Goldstein, S., Modern Developments in Fluid Dynamics, Dover Publications, Inc., New York, 1965.

28. Hanjalic, K., and Launder, B. E., "A Reynolds Stress Model of Turbulence and its Application to Asymmetric Shear Flows," J. Fluid Mech., Vol. 52, 1972.

29. Hill, P. G., Schaub, U. W., and Senoo, Y., "Turbulent Wakes in Pressure Gradients," Trans. of ASME, Dec. 1963.

30. Hu, N., "Statistical Theory of Turbulence," Chinese J. of Physics, Vol. 5, 1944.

31. Hwang, H. C. N., and Baldwin, L. V., "Decay of Turbulence in Axisymmetric Wakes," J. Basic Engg., March 1966.

32. Kiock, R., "Turbulence Downstream of Stationary and Rotating Cascades," ASME Paper 73-GT-80, 1973.

33. Lakshminarayana, B., and Poncet, A., "A Method of Measuring Three-Dimensional Wakes in Turbomachinery," J. Fluids Engg., June, 1974.

34. Lakshminarayana, B., and Raj, R., "Compressor and Fan Rotor Wake Characteristics," Second Interagency Symposium on University Research in Transportation Noise, North Carolina State University, June 5-7, 1974.

35. Landgrebe, A. J., "An Analytical Method for Predicting Rotor Wake Geometry," J. Am. Helicopter Soc., Oct. 1969.

36. Launder, B. E., and Spalding, D. B., Mathematical Models of Turbulence, Academic Press, New York, 1972.

37. Lieblein, S., and Roudenbush, W. H., "Low Speed Wake Characteristics of Two-Dimensional Cascade and Isolated Airfoil Section," NASA, TN 3771, Oct. 1956.

38. Lumley, J. L., "Towards a Turbulent Constitutive Relation," J. Fluid Mech., Vol. 41, 1970.

39. Lumley, J. L., Stochastic Tools in Turbulence, Academic Press, New York, 1970.

40. Lumley, J. L., "A Model for Computation of Stratified Turbulent Flows," International Symposium on Stratified Flows, Novosibirsk, 1972.

41. Lumley, J. L., and Khajeh-Nouri, B., "Computational Modeling of Turbulent Transport," Second IUGG-IUTAM Symposium on Atmsopheric Diffusion and Environmental Pollution, Charlottesville, Va., 1973.

42. Lumley, J. L., and Khajeh-Nouri, B., "Modeling Homogeneous Deformation of Turbulence," Symposium on Turbulence in the Planetary Boundary Layer of Atmosphere, Moscow, 1973. (submitted for publication in J. of Phys. of Fluids)

43. Nash, J. F., and Patel, V. C., Three-Dimensional Turbulent Boundary Layers, Scientific Business Consultants, Atlanta, 1972.

44. Olsson, R. G., "Geschwindigkeits - Und Temperature Verteilung hinter einem Gitter Gei turbulenter Stromung," ZAMN, Vol. 16, 1936.

45. Palmer, M. D., and Keffer, J. F., "An Experimental Investigation of an Asymmetrical Turbulent Wake," J. Fluid Mech., Vol. 53, 1972.

46. Pearson, H., and McKenzie, A. B., "Wakes in Axial Compressors," J. Royal Aero. Soc., July 1959.

47. Preston, S. H., and Sweeting, N. E., "The Experimental Determination of the Boundary Layer and Wake Characteristics of a Simple Joukowski Airfoil, with Particular Reference to the Trailing Edge Region," Gr. Brit. Aero. Res. Council, R and M 1998, 1943.

48. Preston, J. H., Sweeting, N. E., and Miss Cox, D. K., "The Experimental Determination of the Boundary Layer and Wake Characteristics of a Piercy Airfoil with Particular Reference to the Trailing Edge Region," Gr. Brit. Aero. Res. Council, R and M 2013, 1945.

49. Raj, R., and Lakshminarayana, B., "Characteristics of Wakes Behind a Cascade of Airfoils," J. Fluid Mech., Vol. 61, 1973.

50. Raj, R., and Lumley, J. L., "Characteristics of Turbulent Wakes Behind a Rotating Fan," Submitted for Publication in J. Mekhanika Zidkoschi i Gaza ANSSSR; 1974.

51. Reichardt, H., "Gesetzmassigkeiten der freien Turbelenz," VDI--Forschungsheft, Vol. 414, 1945.

52. Reynolds, A. J., "Similarity in Swirling Wakes and Jets," J. Fluid Mech., Vol. 14, 1962.

53. Reynolds, A. J., "Observations on Distorted Turbulent Wakes," J. Fluid Mech., Vol. 13, 1962.

54. Rotta, J., "Statistische Theorie nichthomogener Turbulenz," Zeitsch. für Physik, Vol. 129, 1951.

55. Schlichting, H., and Scholz, N., "Über die Theoretische Berechnung der Strömungsverluste einer ebenen Schaufelgitter," Ing.-Arch., Vol. 19, 1951.

56. Schlichting, H., Boundary Layer Theory, McGraw-Hill Book Company, New York, 1968.

57. Silverstein, A., Katzoff, S., and Bullivant, W., "Downwash and Wake Behind Plain and Flapped Airfoils," NACA TR No. 651, 1939.

58. Spence, D. A., "Growth of Turbulent Wake Close Behind an Airfoil at Incidence," Gr. Brit. Aero. Res. Council, C.P. No. 125, 1952.

59. Steiger, M. H., and Bloom, M. H., "Three-Dimensional Viscous Wakes," J. Fluid Mech., Vol. 14, 1962.

60. Swan, L. M., "Turbulent Wakes Behind a Body of Revolution," Proc. Royal Soc., Vol. 125, 1929.

61. Tennekes, H., and Lumley, J., A First Course in Turbulence, The MIT Press, Cambridge, Massachusetts, 1972.

62. Townsend, A. A., The Structure of Turbulent Shear Flow, Cambridge University Press, 1956.

63. Whitfield, C. E., Kelly, J. C., and Barry, B., "A Three-Dimensional Analysis of Rotor Wakes," Aeronautical Quarterly, Nov. 1972.

APPENDIX A

LISTING OF COMPUTER PROGRAMS FOR ROTOR WAKE DATA PROCESSING

A) FORTRAN PROGRAM TO WRITE EVERY THIRTEENTH WAKE

```
/*TAPE RISH02
/*TAPE MEH07,M,W
// EXEC FGCG
//SOURCE.INPUT DD *
      REAL * 4 V1(5000), V2(5000), V3(5000)
      REAL * 4 V1BK(150), V2BK(150), V3BK(150)
      LOGICAL * 1 CC(16384)
      DATA NUM/0/, IPTR/4097/,IREC/0/,IFILE/1/,IMARK/1/
100   DO 10 I=1,11
      IKEY = 0
      CALL PEAK(V1,V2,V3,V1BK,V2BK,V3BK,IPTR,IKEY,ISWTCH)
      IF(IKEY.NE.0) GO TO 1001
10    IPTR = IPTR + 151
      IKEY = 0
      CALL PEAK(V1,V2,V3,V1BK,V2BK,V3BK,IPTR,IKEY,ISWTCH)
      IF(IKEY.NE.0) GO TO 1001
      IKEY = 0
      CALL WRITE (V1,V2,V3,V1BK,V2BK,V3BK,IPTR,IKEY,
     X             IMARK,IREC)
      IF(IKEY.NE.0) GO TO 1001
      IPTR = IPTR + 151
      GO TO 100
1001  WRITE(6,51) IFILE,IREC
      IREC = 0
      IFILE = IFILE + 1
      IMARK = 1
      IPTR = 4097
      ENDFILE 70
      GO TO 100
51    FORMAT(' ',10X,'FILE NUMBER =',I3,10X,
     X       'NUMBER OF RECORDS=',I3)
      END
      SUBROUTINE RESET(V1,V2,V3,IPTR,ISWTCH,IKEY)
      REAL * 4 V1(5000), V2(5000), V3(5000)
      LOGICAL * 1 CC(16384), L(4)
      EQUIVALENCE (L(1), INT)
      INT = 0
      ISWTCH = 0
100   CALL GET (60,CC,16384,IKEY)
      IF(IKEY.NE.0) RETURN
      DO 10 I=1,4096
      ITEMP = (I-1) * 4 + 1
      L(4) = CC(ITEMP)
      V3(I) = FLOAT(INT)
      L(4) = CC(ITEMP+1)
      V1(I) = FLOAT(INT)
```

```
      L(4) = CC(ITEMP+2)
      V2(I) = FLOAT(INT)
10    CONTINUE
      IPTR = 4
      RETURN
      END
      SUBROUTINE REBK(V1,V2,V3,V1BK,V2BK,V3BK,ISWTCH)
      REAL * 4 V1(5000), V2(5000), V3(5000)
      REAL * 4 V1BK(150), V2BK(150), V3BK(150)
      IKNT = 1
      ISWTCH = 1
      DO 10 I=3947,4096
      V1BK(IKNT) = V1(I)
      V2BK(IKNT) = V2(I)
      V3BK(IKNT) = V3(I)
10    IKNT = IKNT + 1
      RETURN
      END
      SUBROUTINE PEAK (V1,V2,V3,V1BK,V2BK,V3BK,IPTR,
     X                 IKEY,ISWTCH)
      REAL * 4 V1(5000), V2(5000), V3(5000), MIN
      REAL * 4 V1BK(150), V2BK(150), V3BK(150)
      IF(IPTR.GT.4096) CALL RESET(V1,V2,V3,IPTR,
     X                            ISWTCH,IKEY)
      IF(IKEY.NE.0) RETURN
1     DO 10 I=IPTR,4096
      TEMP = V1(I-3) - V1(I)
      TEMP = TEMP/V1(I-3)
      IF(TEMP.GT.0.20) GO TO 11
      IF(ISWTCH.EQ.1) GO TO 10
      IF(I.GT.151) CALL REBK(V1,V2,V3,V1BK,V2BK,
     X                       V3BK,ISWTCH)
10    IPTR = I
      CALL RESET(V1,V2,V3,IPTR,ISWTCH,IKEY)
      IF(IKEY.NE.0) RETURN
      GO TO 1
11    IADD = 0
      IEND = IPTR + 100
      IPTR = IPTR - 2
      IF(IEND.LE.4096) GO TO 12
      IADD = IEND - 4096
      IEND = 4096
12    MIN = 10000.0
      DO 20 I=IPTR,IEND
      IF(V1(I).GE.MIN) GO TO 20
      MIN = V1(I)
      IMIN = I
20    CONTINUE
      IF(IADD.EQ.0) GO TO 21
      CALL RESET(V1,V2,V3,IPTR,ISWTCH,IKEY)
      IF(IKEY.NE.0) RETURN
      DO 30 I=1,IADD
      IF(V1(I).GE.MIN) GO TO 30
      MIN = V1(I)
```

```
      IMIN = I
30    CONTINUE
21    IPTR = IMIN
      RETURN
      END
      SUBROUTINE WRITE(V1,V2,V3,V1BK,V2BK,V3BK,IPTR,IKEY,
     X                 IMARK,IREC)
      REAL * 4 V1(5000), V2(5000), V3(5000)
      REAL * 4 V1BK(150), V2BK(150), V3BK(150)
      REAL * 4 V1F(301), V2F(301), V3F(301)
      LOGICAL * 1 ACCUM(18060), L(4)
      EQUIVALENCE (INT, L(1))
      IKNT = 1
      IF(IPTR.LT.151) GO TO 11
      IF(IPTR.GT.3946) GO TO 21
      ISTRT = IPTR - 150
      IEND = IPTR + 150
      DO 10 I=ISTRT, IEND
      V1F(IKNT) = V1(I)
      V2F(IKNT) = V2(I)
      V3F(IKNT) = V3(I)
10    IKNT = IKNT + 1
      GO TO 100
11    DO 20 I=IPTR,150
      V1F(IKNT) = V1BK(I)
      V2F(IKNT) = V2BK(I)
      V3F(IKNT) = V3BK(I)
20    IKNT = IKNT + 1
      IEND = IPTR + 150
      DO 30 I=IPTR,IEND
      V1F(IKNT) = V1(I)
      V2F(IKNT) = V2(I)
      V3F(IKNT) = V3(I)
30    IKNT = IKNT + 1
      GO TO 100
21    ITEMP = IPTR
      IF(ISWTCH.EQ.0) GO TO 22
      CALL RESET (V1,V2,V3,IPTR,ISWTCH,IKEY)
      IF(IKEY.NE.0) RETURN
22    ISTRT = ITEMP - 3946
      DO 40 I=ISTRT, 150
      V1F(IKNT) = V1BK(I)
      V2F(IKNT) = V2BK(I)
      V3F(IKNT) = V3BK(I)
40    IKNT = IKNT + 1
      IEND = ITEMP + 150
      DO 50 I=ITEMP,IEND
      V1F(IKNT) = V1(I)
      V2F(IKNT) = V2(I)
      V3F(IKNT) = V3(I)
50    IKNT = IKNT + 1
100   MIN = V1F(151)
      DO 60 I=1,301
      IF(MIN.LE.V1F(I)) GO TO 60
```

```
      IF(I.GT.155.OR.I.LT.147) GO TO 71
60    CONTINUE
      DO 70 I=1,301
      INT = IFIX(V1F(I))
      ACCUM(IMARK) = L(4)
      IMARK = IMARK + 1
      INT = IFIX(V2F(I))
      ACCUM(IMARK) = L(4)
      IMARK = IMARK + 1
      INT = IFIX(V3F(I))
      ACCUM(IMARK) = L(4)
      IMARK = IMARK + 1
70    CONTINUE
      IF(IMARK.NE.18061) RETURN
      CALL PUT(70,ACCUM,18060,IKEY)
      IREC = IREC + 1
      IMARK = 1
71    RETURN
      END
//DATA.FT60F001 DD UNIT=(TAPEA,,DEFER),VOL=SER=RISH01,
// LABEL=(1,SL),DSN=FILE1
//DATA.FT60F002 DD UNIT=(TAPEA,,DEFER),VOL=SER=RISH01,
// LABEL=(2,SL),DSN=FILE2
//DATA.FT60F003 DD UNIT=(TAPEA,,DEFER),VOL=SER=RISH01,
// LABEL=(3,SL),DSN=FILE3
//DATA.FT60F004 DD UNIT=(TAPEA,,DEFER),VOL=SER=RISH01,
// LABEL=(4,SL),DSN=FILE4
//DATA.FT60F005 DD UNIT=(TAPEA,,DEFER),VOL=SER=RISH01,
// LABEL=(5,SL),DSN=FILE5
//DATA.FT60F006 DD UNIT=(TAPEA,,DEFER),VOL=SER=RISH01,
// LABEL=(6,SL),DSN=FILE6
//DATA.FT60F007 DD UNIT=(TAPEA,,DEFER),VOL=SER=RISH01,
// LABEL=(7,SL),DSN=FILE7
//DATA.FT60F008 DD UNIT=(TAPEA,,DEFER),VOL=SER=RISH01,
// LABEL=(8,SL),DSN=FILE8
//DATA.FT60F009 DD UNIT=(TAPEA,,DEFER),VOL=SER=RISH01,
// LABEL=(9,SL),DSN=FILE9
//DATA.FT60F010 DD UNIT=(TAPEA,,DEFER),VOL=SER=RISH01,
// LABEL=(10,SL),DSN=FILE10
//DATA.FT70F001 DD UNIT=(TAPEB,,DEFER),VOL=SER=MEH06,
// DSN=MARK.F1,DCB=(RECFM=F,LRECL=18060,BLKSIZE=18060),
// LABEL=(1,SL)
//DATA.FT70F002 DD UNIT=(TAPEB,,DEFER),VOL=SER=MEH06,
// DSN=MARK.F2,DCB=(RECFM=F,LRECL=18060,BLKSIZE=18060),
// LABEL=(2,SL)
//DATA.FT70F003 DD UNIT=(TAPEB,,DEFER),VOL=SER=MEH06,
// DSN=MARK.F3,DCB=(RECFM=F,LRECL=18060,BLKSIZE=18060),
// LABEL=(3,SL)
//DATA.FT70F004 DD UNIT=(TAPEB,,DEFER),VOL=SER=MEH06,
// DSN=MARK.F4,DCB=(RECFM=F,LRECL=18060,BLKSIZE=18060),
// LABEL=(4,SL)
//DATA.FT70F005 DD UNIT=(TAPEB,,DEFER),VOL=SER=MEH06,
// DSN=MARK.F5,DCB=(RECFM=F,LRECL=18060,BLKSIZE=18060),
// LABEL=(5,SL)
```

```
//DATA.FT70F006 DD UNIT=(TAPEB,,DEFER),VOL=SER=MEH06,
// DSN=MARK.F6,DCB=(RECFM=F,LRECL=18060,BLKSIZE=18060),
// LABEL=(6,SL)
//DATA.FT70F007 DD UNIT=(TAPEB,,DEFER),VOL=SER=MEH06,
// DSN=MARK.F7,DCB=(RECFM=F,LRECL=18060,BLKSIZE=18060),
// LABEL=(7,SL)
//DATA.FT70F008 DD UNIT=(TAPEB,,DEFER),VOL=SER=MEH06,
// DSN=MARK.F8,DCB=(RECFM=F,LRECL=18060,BLKSIZE=18060),
// LABEL=(8,SL)
//DATA.FT70F009 DD UNIT=(TAPEB,,DEFER),VOL=SER=MEH06,
// DSN=MARK.F9,DCB=(RECFM=F,LRECL=18060,BLKSIZE=18060),
// LABEL=(9,SL)
//DATA.FT70F010 DD UNIT=(TAPEB,,DEFER),VOL=SER=MEH06,
// DSN=MARK.F10,DCB=(RECFM=F,LRECL=18060,BLKSIZE=18060),
// LABEL=(10,SL)
```

B) FORTRAN PROGRAM TO OBTAIN MEAN VELOCITY, TURBULENCE INTENSITY AND REYNOLDS STRESS.

```
// MSGLEVEL=(1,1)
/*TAPE MEH07
/*USERID MEH02
//WTLOG EXEC PGM=WTLOG
//STEPLIB DD DSN=COMPLIB,DISP=SHR
//FT05F001 DD *
RISH
PLOTS
//STEP1 EXEC FGCG
//SOURCE.INPUT DD *
      REAL * 4 K2
      DIMENSION V1(6020), V2(6020), V3(6020), SUMV(6020)
      DIMENSION SINA(6020), SINB(6020), SINC(6020)
      DIMENSION AVGV1(301), AVGV2(301), AVGV3(301)
      DIMENSION AVGV1S(301), AVGV2S(301), AVGV3S(301)
      DIMENSION SMV1V2(301), SMV2V3(301), SMV3V1(301)
      DIMENSION TEMP2(301), AVG123(301), SUMAVG(301)
      LOGICAL * 1 CC(18060), L(4)
      DATA IREC/1/,DIV/351.0/,IAVG/6020/,K2/0.029/
      DATA V1CON/13.3/,V2CON/6.6/,V3CON/16.0/,NREC/3/
      DATA E1CON/3.210/,E2CON/3.237/,E3CON/3.230/
      EQUIVALENCE (L(1),INT)
      EQUIVALENCE (AVGV1(1), CC(1))
      EQUIVALENCE (AVGV2(1), CC(1205))
      EQUIVALENCE (AVGV3(1), CC(2409))
      EQUIVALENCE (AVGV1S(1),CC(3613))
      EQUIVALENCE (AVGV2S(1),CC(4817))
      EQUIVALENCE (AVGV3S(1),CC(6021))
      EQUIVALENCE (SMV1V2(1),CC(7225))
      EQUIVALENCE (SMV2V3(1),CC(8429))
      EQUIVALENCE (SMV3V1(1),CC(9633))
      EQUIVALENCE (AVG123(1),CC(10837))
```

```
      EQUIVALENCE (SUMAVG(1),CC(12041))
      TAVG = 20.0 * FLOAT(NREC)
      INT = 0
      DO 1000 IREC=1,NREC
      CALL GET (91,CC,18060,KEY)
      IF(KEY) 101,102,103
102   CONST = 3.985/255.0
      K2P2 = K2 + 2.0
      DO 10 I=1,IAVG
      ITEMP = (I-1)*3 +1
      L(4) = CC(ITEMP)
      TEMP = FLOAT(INT-128)*CONST
      TINT = (TEMP/V3CON) + E3CON
      V3(I) = ((TINT**2 - 3.95)/0.802)**2
      L(4) = CC(ITEMP+1)
      TEMP = FLOAT(INT-128)*CONST
      TINT = (TEMP/V1CON) + E1CON
      V1(I) = ((TINT**2 - 3.95)/0.802)**2
      L(4) = CC(ITEMP+2)
      TEMP = FLOAT(INT-128)*CONST
      TINT = (TEMP/V2CON) + E2CON
      V2(I) = ((TINT**2 - 3.95)/0.802)**2
10    SUMV(I) =((V1(I)**2+V2(I)**2+V3(I)**2)/K2P2)**0.5
      DO 20 I=1,IAVG
      SINA(I) = V1(I)/SUMV(I)
      IF(SINA(I).GT.1.0.OR.SINA(I).LT.-1.0) GO TO 11
      SINA(I) = ARSIN(SINA(I))
      SINB(I) = V2(I)/SUMV(I)
      IF(SINB(I).GT.1.0.OR.SINB(I).LT.-1.0) GO TO 11
      SINB(I) = ARSIN(SINB(I))
      SINC(I) = V3(I)/SUMV(I)
      IF(SINC(I).GT.1.0.OR.SINC(I).LT.-1.0) GO TO 11
      SINC(I) = ARSIN(SINC(I))
      GO TO 20
11    SINA(I) = SINA(I-1)
      SINB(I) = SINB(I-1)
      SINC(I) = SINC(I-1)
      SUMV(I) = SUMV(I-1)
      V1(I) = V1(I-1)
      V2(I) = V2(I-1)
      V3(I) = V3(I-1)
20    CONTINUE
      DO 30 I=1,IAVG
      COMVAL = (V1(I)/SUMV(I))**2
      TEMP = ((COMVAL-K2)/(1.0-K2))**0.5
      SINA(I) = ARSIN(TEMP)
      COMVAL = (V2(I)/SUMV(I))**2
      TEMP = ((COMVAL-K2)/(1.0-K2))**0.5
      SINB(I) = ARSIN(TEMP)
      COMVAL = (V3(I)/SUMV(I))**2
      TEMP = ((COMVAL-K2)/(1.0-K2))**0.5
      SINC(I) = ARSIN(TEMP)
C
C
```

```
C      COORDINATE TRANSFORMATION
C
       V1(I) = COS(SINA(I))/TEMP*SUMV(I)*(0.82*TEMP+
     X         0.575*COS(SIN(I)))
       V2(I) = COS(SINB(I))/TEMP*SUMV(I)*(0.82*TEMP+
     X         0.575*COS(SINC(I)))
       V3(I) =  SUMV(I)*(-0.575*TEMP + 0.82*COS(SINC(I)))
       V1(I) = 0.707 * (V1(I) + V2(I))
       V2(I) = 0.707 * (V1(I) - V2(I))
       V2(I) = 59.5 - V2(I)
30     CONTINUE
       CALL PUT (80,V1,24080,IKEY)
       CALL PUT (80,V2,24080,IKEY)
       CALL PUT (80,V3,24080,IKEY)
1000   CONTINUE
       REWIND 80
C
       DO 1100 I=1,301
       AVGV1(I) = 0.0
       AVGV2(I) = 0.0
       AVGV3(I) = 0.0
       AVGV1S(I) = 0.0
       AVGV2S(I) = 0.0
       AVGV3S(I) = 0.0
       SMV1V2(I) = 0.0
       SMV2V3(I) = 0.0
       SMV3V1(I) = 0.0
1100   CONTINUE
C
C       BEGINNING OF THE AVERAGING PROCEDURE
C
       DO 2000 IREC=1,NREC
       CALL GET (80,V1,24080,IKEY)
       CALL GET (80,V2,24080,IKEY)
       CALL GET (80,V3,24080,IKEY)
       DO 2000 IKNT=1,301
       DO 50 I=IKNT,IAVG,301
       AVGV1(IKNT) = AVGV1(IKNT) + V1(I)
       AVGV2(IKNT) = AVGV2(IKNT) + V2(I)
       AVGV3(IKNT) = AVGV3(IKNT) + V3(I)
50     CONTINUE
       V1MAXL = -10000.0
2000   CONTINUE
       DO 3000 IKNT=1,301
C
C
C      MEAN VELOCITY
C
       AVGV1(IKNT) = AVGV1(IKNT)/TAVG
       AVGV2(IKNT) = AVGV2(IKNT)/TAVG
       AVGV3(IKNT) = AVGV3(IKNT)/TAVG
       IF(AVGV1(IKNT).GT.V1MAXL) V1MAXL = AVGV1(IKNT)
3000   CONTINUE
       REWIND 80
```

```
      DO 3100 I=1,301
      AVGV1S(I) = 0.0
      AVGV2S(I) = 0.0
      AVGV3S(I) = 0.0
      SMV1V2(I) = 0.0
      SMV2V3(I) = 0.0
      SMV3V1(I) = 0.0
3100  CONTINUE
      D = AVGV2(151)/AVGV1(151)
      D = ATAN(D)
      DO 3300 I=1,301
      AVGV1(I) = AVGV1(I)*COS(D) + AVGV2(I)*SIN(D)
      AVGV2(I) = -AVGV1(I)*SIN(D) + AVGV2(I)*COS(D)
3300  CONTINUE
      DO 4000 IREC=1,NREC
      CALL GET(80,V1,24080,IKEY)
      CALL GET(80,V2,24080,IKEY)
      CALL GET(80,V3,24080,IKEY)
      DO 4000 IKNT=1,301
      DO 60 I=IKNT,IAVG,301
      V1(I) = V1(I)*COS(D) + V2(I)*SIN(D)
      V2(I) = -V1(I)*SIN(D) + V2(I)*COS(D)
      AVGV1S(IKNT) = AVGV1S(IKNT)+(V1(I)-AVGV1(IKNT))**2
      AVGV2S(IKNT) = AVGV2S(IKNT)+(V2(I)-AVGV2(IKNT))**2
      AVGV3S(IKNT) = AVGV3S(IKNT)+(V3(I)-AVGV3(IKNT))**2
60    CONTINUE
4000  CONTINUE
      REWIND 80
C
C
C     TURBULENCE INTENSITY
C
      DO 4100 IKNT=1,301
      AVGV1S(IKNT) = AVGV1S(IKNT)/TAVG
      AVGV2S(IKNT) = AVGV2S(IKNT)/TAVG
      AVGV3S(IKNT) = AVGV3S(IKNT)/TAVG
      AVG123(IKNT) = (AVGV1S(IKNT) + AVGV2S(IKNT) +
     X               AVGV3S(IKNT))**0.5
      AVGV1S(IKNT) = AVGV1S(IKNT)**0.5
      AVGV2S(IKNT) = AVGV2S(IKNT)**0.5
      AVGV3S(IKNT) = AVGV3S(IKNT)**0.5
4100  CONTINUE
      DO 5000 IREC=1,NREC
      CALL GET(80,V1,24080,IKEY)
      CALL GET(80,V2,24080,IKEY)
      CALL GET(80,V3,24080,IKEY)
      DO 5000 IKNT=1,301
      DO 70 I=IKNT,IAVG,301
      V1(I) = V1(I)*COS(D) + V2(I)*SIN(D)
      V2(I) = -V1(I)*SIN(D) + V2(I)*COS(D)
      TV1 = V1(I) - AVGV1(IKNT)
      TV2 = V2(I) - AVGV2(IKNT)
      TV3 = V3(I) - AVGV3(IKNT)
      SMV1V2(IKNT) = SMV1V2(IKNT) + TV1*TV2
```

```
      SMV2V3(IKNT) = SMV2V3(IKNT) + TV2*TV3
      SMV3V1(IKNT) = SMV3V1(IKNT) + TV3*TV1
70    CONTINUE
5000  CONTINUE
C
C
C     REYNOLDS STRESS
C
      DO 5100 IKNT=1,301
      SMV1V2(IKNT) = SMV1V2(IKNT)/TAVG
      SMV2V3(IKNT) = SMV2V3(IKNT)/TAVG
      SMV3V1(IKNT) = SMV3V1(IKNT)/TAVG
      SUMAVG(IKNT) = (SMV1V2(IKNT)**2+SMV2V3(IKNT)**2+
     X             SMV3V1(IKNT)**2)**0.5/AVG123(IKNT)**2
5100  CONTINUE
      V1MAX = -100000.0
      DO 80 I=1,301
      IF(AVGV1(I).GT.V1MAX) V1MAX = AVGV1(I)
80    CONTINUE
      V1MAX2 = V1MAX**2
      DO 90 I=1,301
      AVGV1(I) = AVGV1(I)/V1MAX
      AVGV2(I) = AVGV2(I)/V1MAX
      AVGV3(I) = AVGV3(I)/V1MAX
      AVGV1S(I) = AVGV1S(I)/V1MAX
      AVGV2S(I) = AVGV2S(I)/V1MAX
      AVGV3S(I) = AVGV3S(I)/V1MAX
      AVG123(I) = AVG123(I)/V1MAX
      SMV1V2(I) = SMV1V2(I)/V1MAX2
      SMV2V3(I) = SMV2V3(I)/V1MAX2
      SMV3V1(I) = SMV3V1(I)/V1MAX2
90    CONTINUE
      WRITE(6,82) IREC,V1MAXL,V1MAX
      WRITE(6,71)
      DO 701 I=1,301
701   WRITE(6,81) I,AVGV1(I),AVGV2(I),AVGV3(I),TEMP2(I)
      WRITE(6,72)
      DO 702 I=1,301
702   WRITE(6,81) I,AVGV1S(I),AVGV2S(I),AVGV3S(I),
     X            AVG123(I)
      WRITE(6,73)
      DO 703 I=1,301
703   WRITE(6,81) I,SMV1V2(I),SMV2V3(I),SMV3V1(I),
     X            SUMAVG(I)
      CALL PUT(70,CC,13244,IKEY)
      STOP
101   WRITE(6,61)
      STOP
103   WRITE(6,62)
      STOP
61    FORMAT('-', T10, 'ERROR ON TAPE')
62    FORMAT('-', T10, 'END OF FILE ON TAPE')
63    FORMAT('-', T10, 'RECORD NUMBER',2X,I5)
71    FORMAT('-',T28,'AVGV1',T58,'AVGV2',T88,'AVGV3',
```

```
     X        T118,'TEMP'//)
72     FORMAT('-',T28,'AVGV1S',T58,'AVGV2S',T88,'AVGV3S',
     X        T118,'AVG123'//)
73     FORMAT('-',T28,'SMV1V2',T58,'SMV2V3',T88,'SMV3V1',
     X        T118,'SUMAVG'//)
81     FORMAT(' ',I5,4(10X,F20.8))
82     FORMAT('1',10X,'DATA SET NUMBER',I5,5X,'V1MAXL=',
     X        F10.5,10X,'V1MAX=',F10.5///)
       END
//DATA.SYSLIN DD DSN=&&OBMOD,DISP=(OLD,DELETE,DELETE),
// DCB=(RECFM=FB,LRECL=80,BLKSIZE=3120)
//DATA.FT70F001 DD UNIT=3330,VOL=SER=SYSDA1,DSN=MARK.F1,
// DCB=(RECFM=FT,LRECL=13244,BLKSIZE=13244,BUFNO=1),
// DISP=(NEW,PASS,DELETE),SPACE=(CYL,(5,1))
//DATA.FT80F001 DD UNIT=3330,VOL=SER=SYSDA1,DSN=TEMP,
// DCB=(RECFM=FT,LRECL=24080,BLKSIZE=24080,BUFNO=1),
// DISP=(NEW,DELETE),SPACE=(CYL,(5,2))
//DATA.FT91F001 DD UNIT=(2400,,DEFER),VOL=SER=MEH07,
// LABEL=(1,SL),DSN=MARK.F1,DCB=BUFNO=1
//STEP2 EXEC FGCG
//SOURCE.INPUT DD *
       REAL * 4 DATA(301,11),Y(301),X(301),DP(6,2000)
       INTEGER * 2 AP(2000), BP(2000), CP(2000)
       LOGICAL * 1 LABEL(40,2), SYM/'*'/, GRAPH(13244)
       EQUIVALENCE (DATA(1,1),GRAPH(1))
       DATA N/301/
       CALL INITQ (AP,BP,CP,DP,2000)
       CALL GET(50,GRAPH,13244,IKEY)
       DO 10 I=1,N
10     X(I) = FLOAT(I-151)/178.0
       DO 100 IGR=1,11
       DO 90 I=1,301
90     Y(I) = DATA(I,IGR)
       LOGX = 0
       LOGY = 0
       XAXIS = 7.0
       YAXIS = 5.0
       XMIN = 100000.0
       XMAX = -10000.0
       DO 15 I=1,N
       IF(X(I).GT.XMAX) XMAX = X(I)
       IF(X(I).LT.XMIN) XMIN = X(I)
15     CONTINUE
       XINC = (XMAX-XMIN)/5.0
       NXDEC = 5
       YMIN = 10000.0
       YMAX = -10000.0
       DO 20 I=1,N
       IF(Y(I).GT.YMAX) YMAX = Y(I)
       IF(Y(I).LT.YMIN) YMIN = Y(I)
20     CONTINUE
       YINC = (YMAX-YMIN)/4.0
       NYDEC = 4
       XSMIN = XMIN
```

```
       XSMAX = XMAX
       YSMIN = YMIN
       YSMAX = YMAX
       ICON = 0
       HT = 0.15
       NDECX = 2
       NDECY = 2
       IF(YSMIN.LT.0.01) NDECY = 4
       HTS = 0.15
       READ(5,51) (LABEL(I,1),I=1,40)
       READ(5,51) (LABEL(I,2),I=1,40)
       CALL PLOTIT(Y,N,LOGX,LOGY,XAXIS,YAXIS,XMIN,XINC,
     X             NXDEC,YMIN,YINC,NYDEC,LABEL,XSMIN,
     X             XSMAX,YSMIN,YSMAX,X,SYM,ICON,HT,
     X             NDECX,NDECY,HTS)
       CALL PAWZQ
100    CONTINUE
       RETURN
51     FORMAT(40A1)
       END
//DATA.FT07F001 DD UNIT=BAT,FILES=($T2F1B1,$T2F1B2)
//DATA.FT50F001 DD UNIT=3330,VOL=SER=SYSDA1,DSN=MARK.F1,
// LABEL=(1,SL),DISP=(OLD,DELETE)
//DATA.INPUT DD *
       -2Y/S                    +2Y/S
             AVGUS/AVGUSMAX         T2F1
       -2Y/S                    +2Y/S
             AVGUN/AVGUSMAX
       -2Y/S                    +2Y/S
             AVGUR/AVGUSMAX
       -2Y/S                    +2Y/S
          AVGUS2**0.5/AVGUSMAX
       -2Y/S                    +2Y/S
          AVGUN2**0.5/AVGUSMAX
       -2Y/S                    +2Y/S
          AVGUR2**0.5/AVGUSMAX
       -2Y/S                    +2Y/S
          AVGUSUN/AVGUSMAX**2
       -2Y/S                    +2Y/S
          AVGUNUR/AVGUSMAX**2
       -2Y/S                    +2Y/S
          AVGURUS/AVGUSMAX**2
       -2Y/S                    +2Y/S
                    Q
       -2Y/S                    +2Y/S
                 T/Q**2
/*
```

APPENDIX B

ROTATING PROBE MEASUREMENT

It has been indicated in Chapter IX that it is not feasible to investigate regions $s/S' < 0.15$ with a stationary three-sensor hot wire probe due to physical limitations. However, the largest decay of the wake centerline velocity (up to 90 percent) occurs in this region. Moreover, the investigations were carried out in a rotor specifically designed to operate at zero loading. Even though the actual rotor has a small loading, it cannot be operated at high lift coefficients normally encountered in practice.

The abovementioned difficulties can be overcome by carrying out measurements in a rotating frame of reference and on a loaded rotor. Therefore, it is first planned to repeat the stationary probe measurement with a rotating probe measurement with a special emphasis on regions close to the trailing edge ($s/S' < 0.15$) and boundary layer on the trailing edge to know the initial conditions and regions very close to the hub and the annulus wall.

For carrying out rotating probe measurement, the Axial Flow Research Fan Facility of the Applied Research Laboratory is being modified. A rotating traversing mechanism (Figure B-1) is being installed. The traversing mechanism, when in full operation, will provide two degrees of freedom to the probe in rotation (one about its own axis and the second in the circumferential direction). While stationary, the probe location can be changed radially and axially.

The block diagram of turbulence instrumentation for rotating probe measurement is shown in Figure B-2. The quantities obtained

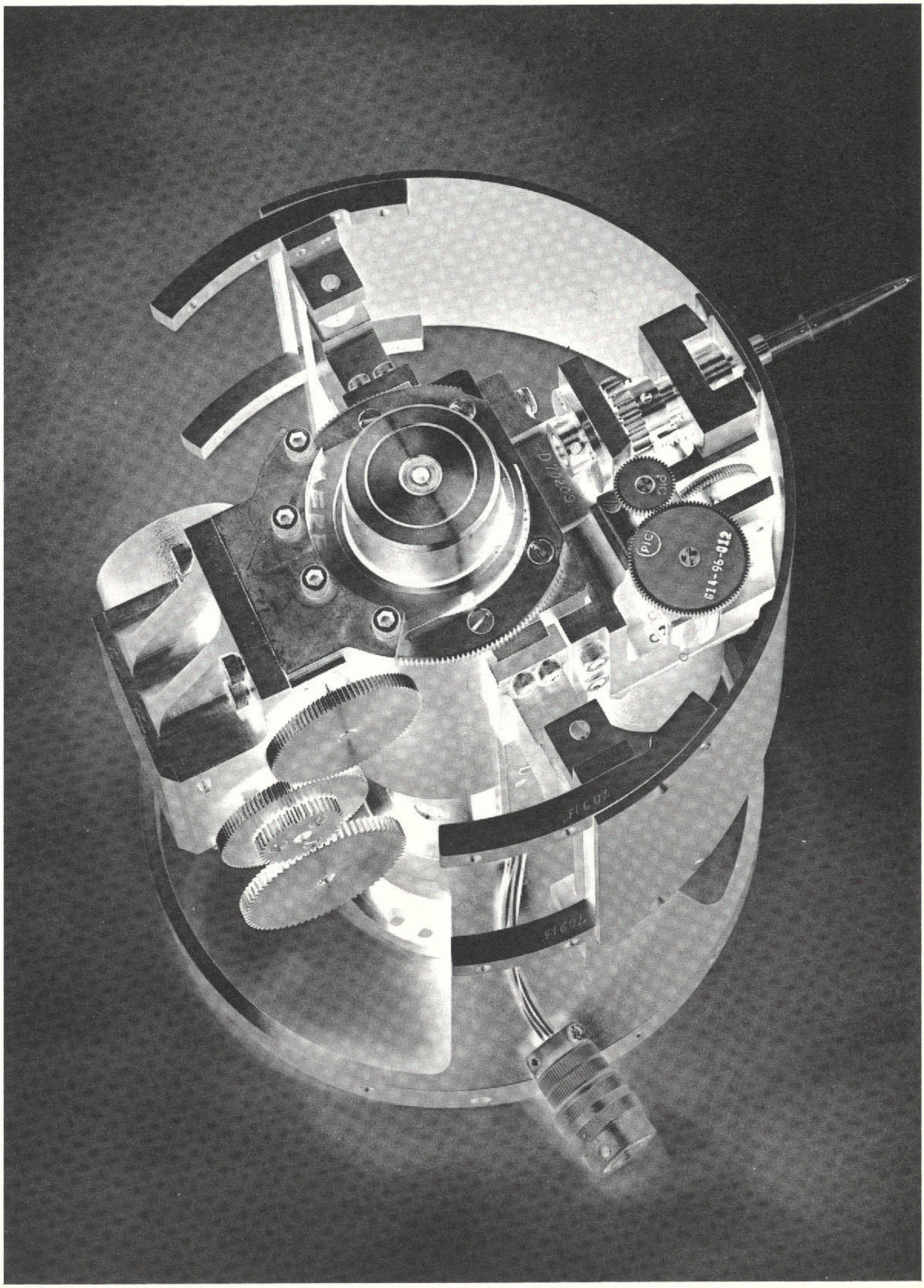

Figure B-1 Traversing Mechanism.

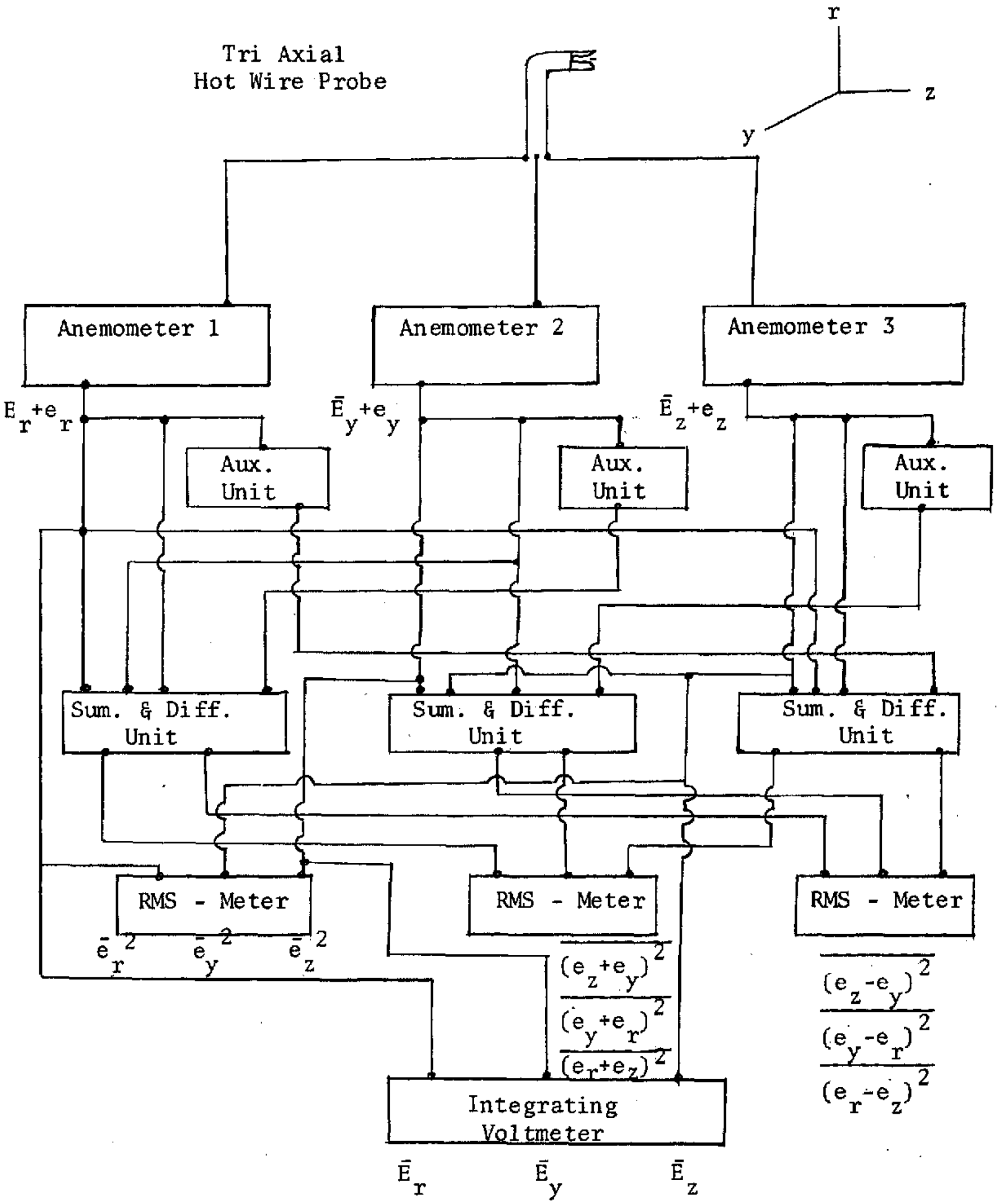

Figure B-2 Block Diagram of Turbulence Instrumentation for Mean Velocity, Turbulence Intensity, and Shear Stresses.

can be transferred in any new coordinate system by using the standard method of coordinate transformation.

The program of rotating probe measurements is outlined in Reference (34).